Surface organometallic chemistry on Titania

Tapish Saboo

N°d'ordre NNT : 2018LYSE1061

THESE de DOCTORAT DE L'UNIVERSITE DE LYON
opérée au sein de
l'Université Claude Bernard Lyon 1

Ecole Doctorale de Lyon
N° ED206

Spécialité de doctorat : Chimie
Discipline : Chimie Industrielle Durable

Soutenue publiquement le 06/04/2018
par

M. Tapish Saboo

Chimie organométallique de surface sur l'oxyde de titane

Jury :

Prof. Stefania Albonetti	Rapporteuse	Università di Bologne
Dr. Francesco Di Renzo	Rapporteur	CNRS-ICG Montpellier
Dr. Claudio Ampelli	Examinateur	Università degli Studi di Messina
Prof. Dominique Luneau	Examinateur	Université Claude Bernard Lyon1
Dr. Elsje A. Quadrelli	Directrice de thèse	CNRS-C2P2 Lyon
Prof. Siglinda Perathoner	Co-directrice de thèse	Università degli Studi di Messina

Surface Organometallic Chemistry on Titania

DOCTORAL THESIS

Université Claude Bernard Lyon 1

and

Universita` degli Studi di Messina

SINCHEM - Sustainable and Industrial Chemistry

Erasmus Mundus - Joint Doctoral Research program

Ecole Doctorale N° 206
(Ecole Doctorale de Chimie de Lyon : Chimie, Procédés, Environnement)
and
Dottorato di XXX ciclo in
Ingegneria e Chimica dei Materiali e delle Costruzioni

Supervisors
Dr. Elsje Alessandra Quadrelli (Lyon)
and
Prof.ssa Siglinda Perathoner (Messina)

Co-Supervisor
Dr. Claudio Ampelli (Messina)

Thesis by

Tapish Saboo

April, 2018

UNIVERSITE CLAUDE BERNARD - LYON 1

Président de l'Université	**M. le Professeur Frédéric FLEURY**
Président du Conseil Académique	M. le Professeur Hamda BEN HADID
Vice-président du Conseil d'Administration	M. le Professeur Didier REVEL
Vice-président du Conseil Formation et Vie Universitaire	M. le Professeur Philippe CHEVALIER
Vice-président de la Commission Recherche	M. Fabrice VALLÉE
Directrice Générale des Services	Mme Dominique MARCHAND

COMPOSANTES SANTE

Faculté de Médecine Lyon Est – Claude Bernard	Directeur : M. le Professeur G.RODE
Faculté de Médecine et de Maïeutique Lyon Sud – Charles Mérieux	Directeur : Mme la Professeure C. BURILLON
Faculté d'Odontologie	Directeur : M. le Professeur D. BOURGEOIS
Institut des Sciences Pharmaceutiques et Biologiques	Directeur : Mme la Professeure C. VINCIGUERRA
Institut des Sciences et Techniques de la Réadaptation	Directeur : M. X. PERROT
Département de formation et Centre de Recherche en Biologie Humaine	Directeur : Mme la Professeure A-M. SCHOTT

COMPOSANTES ET DEPARTEMENTS DE SCIENCES ET TECHNOLOGIE

Faculté des Sciences et Technologies	Directeur : M. F. DE MARCHI
Département Biologie	Directeur : M. le Professeur F. THEVENARD
Département Chimie Biochimie	Directeur : Mme C. FELIX
Département GEP	Directeur : M. Hassan HAMMOURI
Département Informatique	Directeur : M. le Professeur S. AKKOUCHE
Département Mathématiques	Directeur : M. le Professeur G. TOMANOV
Département Mécanique	Directeur : M. le Professeur H. BEN HADID
Département Physique	Directeur : M. le Professeur J-C PLENET
UFR Sciences et Techniques des Activités Physiques et Sportives	Directeur : M. Y.VANPOULLE
Observatoire des Sciences de l'Univers de Lyon	Directeur : M. B. GUIDERDONI
Polytech Lyon	Directeur : M. le Professeur E.PERRIN
Ecole Supérieure de Chimie Physique Electronique	Directeur : M. G. PIGNAULT
Institut Universitaire de Technologie de Lyon 1	Directeur : M. le Professeur C. VITON
Ecole Supérieure du Professorat et de l'Education	Directeur : M. le Professeur A. MOUGNIOTTE
Institut de Science Financière et d'Assurances	Directeur : M. N. LEBOISNE

INSPIRATION

लहरों से डर कर नौका पार नहीं होती,

कोशिश करने वालों की कभी हार नहीं होती।

असफलता एक चुनौती है, इसे स्वीकार करो,

क्या कमी रह गई, देखो और सुधार करो।

जब तक न सफल हो, नींद चैन को त्यागो तुम,

संघर्ष का मैदान छोड़ कर मत भागो तुम।

कुछ किये बिना ही जय जय कार नहीं होती,

कोशिश करने वालों की कभी हार नहीं होती।

- सोहन लाल द्विवेदी

INSPIRATION

The boat that qualms the waves
Never gets across
The mind that dreads and dares
Has never been at loss
O' accept the failures that cross your way
They are just the challenging mile-stones
And build from right here, where you fell
Until all the shortcomings cease
And you soar in success
Burn restful sleeps in the sacrificial pyres
Until tireless struggles brought smiles of joy
Oh! Do not run away from the battlefields
For triumph always yields such joy
Just after relentless endeavours…….

- Sohanlal Dwivedi

Acknowledgments

It was often said that PhD is a lonely journey. It is a journey that can be completed by no one else but oneself. Fortunately, my PhD life was accompanied by so many people who made significant contributions towards the completion of this thesis. It is difficult to mention all of them individually (would need another chapter in this thesis), but there are some whose exceptional contributions deserve distinctive acknowledgement.

First and foremost, I express my immense gratitude to Dr. Elsje Alessandra Quadrelli, whose scientific expertise, advice, support and wisdom carved a path for thesis from the very early stage. Her excellent presentation skills and brainstorming sessions helped me boost my confidence and plan my work. Not only has she been a great mentor but has also been an amazing curator. Any success that I achieve in my professional life will include her preaching.

One of the key elements of any PhD is independent research- the ability to design, develop and perform experiments independently. I thank Prof. Siglinda Perathoner at University of Messina, who truly helped me develop this quality by allowing me to explore my design of experiments. Her cutting edge knowledge in the subject and calm and composed nature allowed me to progress rapidly in the subject. I would also like to thank Prof. Gabriele Centi for his backstage insights into this thesis.

I am deeply grateful to Dr. Claudio Ampelli (my co-supervisor) for his thought-provoking insights, prompt solutions and planning that helped me attain success in the project in a limited time at hand. His scientific curiosity and technical skills facilitated my work life in Messina.

Characterization of the newly developed materials is an integral aspect of a PhD thesis. I indeed indebted to Dr Kai Szeto, Mr Laurent Veyre, Mrs Christine Lucas, Dr Nesrine Cherni, Dr Aimery DeMallmann, Dr Mostafa Taoufik, Mr François Bayard, Mr Ruben Vera, Mr Lhoussain Khrouz from University of Lyon and Mr Salvatore Abate from University of Messina for helping me in the analysis of my materials using various characterization tools. I feel obliged for sharing your expertise of different techniques with me. It has and will help me in the coming future.

I thank Dr Frédéric Lefebvre for his contributions in DFT modelling as well as technical feedbacks. I appreciate Dr Chloé Thieuleux and Dr Clement Camp for their comments during the group meetings.

I would also like to mention Mrs Emmanuelle Fouilhe (University of Lyon) and Mrs Anna Maria Cassella (University of Messina) who ensured that my administrative status was up to date and helped me schedule my conferences and meetings.

Scientific discussions are a fuel to research. These debates are a pool of freshly brewed ideas stemming from scientific inquisitiveness. My heartfelt thanks are to Stéphane, Marc and Cherif whose vast knowledge and discussions helped me expand my scientific expertise.

None of the aforementioned wonderful people would have touched my life, if not for SINCHEM. Therefore, I am immensely grateful to Prof. Stefania Albonetti, who put incredible effort and enthusiasm in starting an Erasmus Mundus funded program, of which I am honoured to be a part.

Every PhD has its own unique challenges and more often than not, tackling these challenges gives you a hard time. I am exceptionally thankful to Pooja, Giuliana and Nimisha who stood by me and helped me overcome all these difficult situations during my PhD tenure. Without your warmth, this thesis would have been a much more daunting task.

I would specially like to mention Vittoria, Walid and Sebastian for their quick and to the point translations.

I would also like to thank Reine, Iuliia, Tibo, Fred, David, Audrey, Debora, Matthieu, Iurii, Tin, Mathilde, Danilo, Ravi, Nicolas, Gleb, Sebastian, Walid, Bishoy, Clément Demarcy, Vittoria, Pascal, Bhanu, Gunjita, Shifa, Aditi, Shilpa, Giorgia, Chiara, Francesco, Katia, Andres, Chalachew and the entire SINCHEM family for being my special friends and keeping my life upbeat.

Last but not the least, I am thankful to the almighty and my grandmother, parents and my brother for supporting me and showering me with their love and best wishes.

List of Abbreviations

SOMC : Surface organometallic chemistry

MMCT : Metal to metal charge transfer

EXAFS : Extended X-ray absorption fine structure

XANES : X-ray absorption near edge structure

STEM : Scanning transmission electron microscopy

HRTEM : High-resolution transmission electron microscopy

SEM : Scanning electron microscopy

DRIFT : Diffuse reflectance infrared Fourier transform

FTIR : Fourier-transform infrared spectroscopy

XRD : X-Ray diffraction spectroscopy

EPR : Electron paramagnetic resonance

DFT : Density functional theory

PEC : Photo electro catalytic cell

BuH : n-butane

NpH : Neopentane

n-BuLi : n-Butyl lithium

2-mIm : 2-methyl Imidazole

TNT's : Titania nanotubes

PCE : Photo conversion efficiency

UHV : Ultra high vacuum (10^{-5} Torr)

CVD : Chemical Vapour Deposition

Abstract

Homogeneous and heterogeneous catalysts have been serving the chemical industries for over 90 years easing the conversion of bulk chemical feedstock into fine chemicals.[1,2] While they both have their advantages such as, for example, similar actives sites homogeneous catalysts and high temperature stability and recyclability for heterogeneous catalysts. The catalysts still have avenues of improvements such as higher efficiency, selectivity, temperature stability, recyclability of the catalysts etc.

Surface organometallic chemistry (SOMC) a technique developed in the 60's[3] and refined over the years provides the gap between homogeneous and heterogeneous catalysis by producing supported catalysts with well-defined active sites.[4,5] The method involves reaction of organometallic complex with surface sites of a support in a controlled fashion as shown in Figure 1. SOMC gives us the capability to design (in ideal cases) heterogeneous

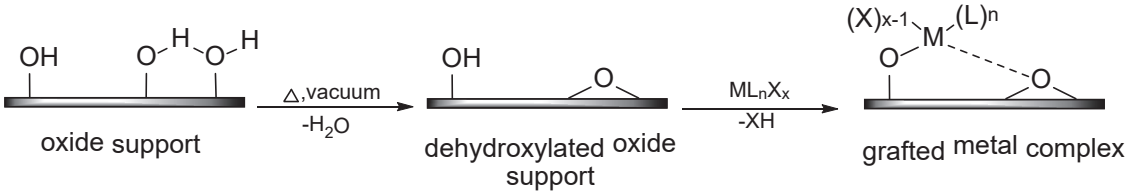

Figure 1 Schematic representation of preparation of a well-defined catalyst using SOMC on a solid oxide whose ultimate surface can be correctly described by a collection of surface hydroxyls.

catalysts with well-defined coordination sphere in molecular terms as in homogeneous catalysts. The grafted organometallic complexes can be directly used as a catalyst by themselves or can be treated in presence of a reactive or inert gas or vacuum to obtain isolated surface species.

A schematic representation explaining the construction of a catalyst prepared by SOMC and the wide variety of metal complexes that can be used as doping agents is shown below (Figure 2). The key components of the catalyst are: i) the support, ii) the metal, iii) the functional ligand and iv) the ancillary ligand. Supports such as silica, silica-alumina, alumina, zeolites, polymers etc. comprising of different surface sites can be used for grafting organometallic complexes comprising of various metal-ligand assembly.[6] The grafted surface moieties are usually characterized by means of advanced characterization tools such as SSNMR, EXAFS and XANES combined with basic set of tools such as IR, GC and elemental analysis.

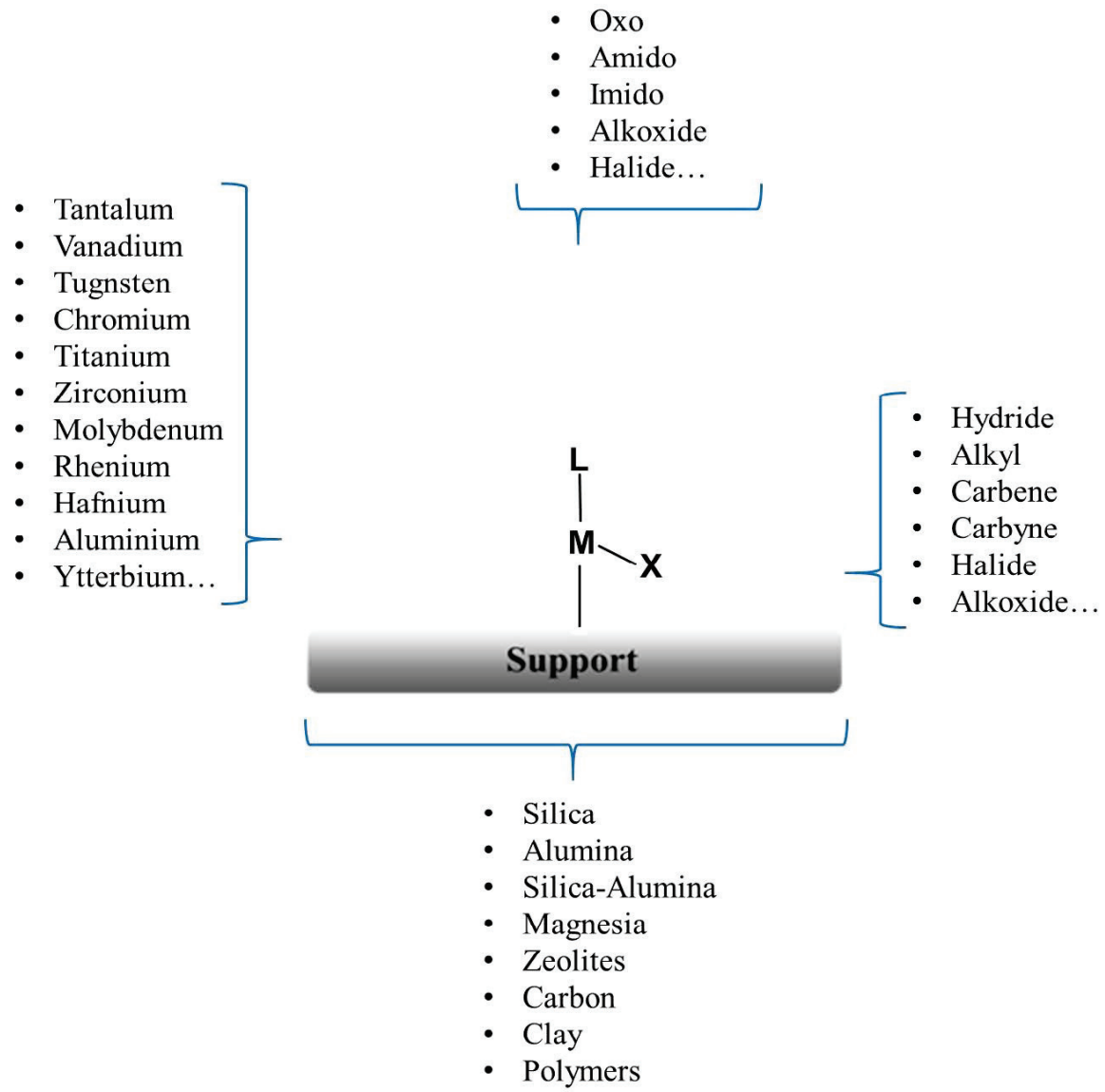

Figure 2 The generic structure of surface organometallic compounds and the possibility of bearing different possible supports, transition metals, functional and spectator ligands (only monopodal specie is shown for simplicity, likewise, possible ancillary assistance from neighbouring surface moieties is omitted too).

Amongst the various supports, silica is one of the most studied support whose surface consists of siloxy bridges (≡Si-O-Si≡) and silanols (≡Si-OH). The surface silanols are mainly divided into 3 categories namely: vicinal, germinal and isolated.[7] Dehydroxylation under dynamic vacuum at 150°C leads to desorption of physisorbed water whereas heating at higher temperature starts dehydroxylation process where two vicinal hydroxyls surface condense to eliminate a water molecule and yield a surface siloxy bridge. This process at

700°C generates isolated surface hydroxyl species. Once qualitatively analysed *via* DRIFT spectroscopy, the quantitative estimation of silanols is performed using chemical titration. The method involves reaction of accessible hydroxyls with metal alkyls (n-*Bu*Li) or metal alkyl halides (MeMgBr) to produce alkanes that can be quantified by gas chromatography.[8,9]

Grafting an organometallic complex onto supports generally requires anhydrous and anaerobic conditions. Typically, an organometallic precursor with an M^1—X configuration is chosen for which the reaction $\mathbf{M^1—X + M—OH \rightarrow M—O—M^1 + HX}$ is favoured thermodynamically, with M—OH being the hydroxyl group of the support. Such SOMC catalysts have been used for several applications including alkane metathesis, olefin metathesis and alkene polymerization. Although exciting, most of the applications based on SOMC catalysts are fossil to fossil conversions. The current trends in CO_2 emissions and usage of non-renewables has emerged a need for shifting the energy dynamics from a fossil based transformation to solar driven transformation.

Titania or TiO_2, a photoactive support, has been widely used as a pigment[10], in sunscreens, paints[11], ointments, self-cleaning windows, water splitting[12], CO_2 photoreduction[13] etc. When in nature, it usually exists in 3 polymorphs: anatase, rutile and brookite. The most commonly used polymorphs amongst them are anatase and rutile with a band gap of 3.05 eV and 2.98 eV respectively.[14] Even though rutile has a lower band gap which allows absorption in visible region, anatase displays more photoactivity. Many studies have indicated that anatase TiO_2 with a higher crystallinity, smaller particle size, and larger surface area is favorable for photocatalysis.[15] To overcome the limitations of anatase, various methods have been implemented such as doping with different metals and non-metals, the addition of sacrificial layers such as dyes and sensitization with new enzymes and polymers.[22] Moreover, the applications mentioned above do not focus on the control of surface-doping interactions. This can give rise to a photocatalyst comprising hindered surface active sites, which ultimately leads to a decrease in overall photocatalytic efficiency. One of the possible ways to recover this loss of efficiency is the development of well-defined photocatalysts with precise surface sites.

SOMC is well-known to provide control while grafting dopants. SOMC on titania is not well-explored and only a few examples exists in literature. Organometallic precursors such as $(CH_3)_4Sn$, nickelocene, ruthenocene etc. have been grafted on the surface on anatase.[6]

Different characterization tools have been used to understand the interaction between the surface and active metal species that follows a metal to metal charge transfer mechanism when exposed to photons. But what most of these studies lack is the basic quantitative estimation of surface titanols before grafting metal precursors to form a well-defined catalyst. The goal of this thesis is to develop a reliable activation procedure leading to a well defined structure whose qualitative and quantitive decsription of the reactive surface species is known and accessible by SOMC.

To develop a well-characterized surface for SOMC, it was necessary to eliminate all the physiosrbed water and partially dehydroxylate the surface of titania. TiO_2 anatase (99.7%) from alfa aesar was calcined at 450°C under air to ensure crystallinity of the powder and eliminate surface organic impurities (if any). It was then partially dehydroxylated at 200°C, 500°C and 700°C under UHV to obtain a white powder with different surface area and pore volumes. XRD combined with HRTEM suggested the presence of anatase phase with (101) crystal plane of anatase as the predominant species for $TiO_{2(700)}$. These results were in line with the Gibbs-Curie-Wulff construction that suggested the predominance of (101) crystal plane over other planes with 1-6% of (001) crystal plane. The DRIFT spectra was used to analyse the qualitative aspects of TiO_2 anatase dehydroxylated at different temperatures.

At 700°C, all the physisorbed water was completely eliminated and three isolated peaks were observed in 3600-3800 cm^{-1}. 12 different types of hydroxyls have been assigned on different crystal planes of titania in literature, suggesting the ambiguous and complex nature of surface hydroxyls. In our work, the peak at 3670 cm^{-1} was assigned to a bridging hydroxyl on (101) facet of anatase. The broad peak at 3715 cm^{-1} and sharp peak at 3741 cm^{-1} were assigned to a chemisorbed H_2O on (100) and terminal hydroxyl on (001) facets respectively.

Chemical titration combined with FTIR analysis allowed quantification of the above mentioned hydroxyl concentration. A chemical titration can simply be defined as the reaction between surface hydroxyls and an organometallic precursor (such as n-*Bu*Li), the resultant being an alkane that can be quantified using gas chromatography (GC). When $TiO_{2(700)}$ was treated with n-*Bu*Li the reaction was assumed to follow a pathway as shown in Eq.1, Eq.2 and Eq.3; reacting with all the accessible surface hydroxyls and coordinated water to produce butane. GC quantification estimated the presence of approximately 0.73

OH/nm^2 which was within a 10% error bar of the value estimated by FTIR spectroscopy (~ 0.8 OH/nm^2).

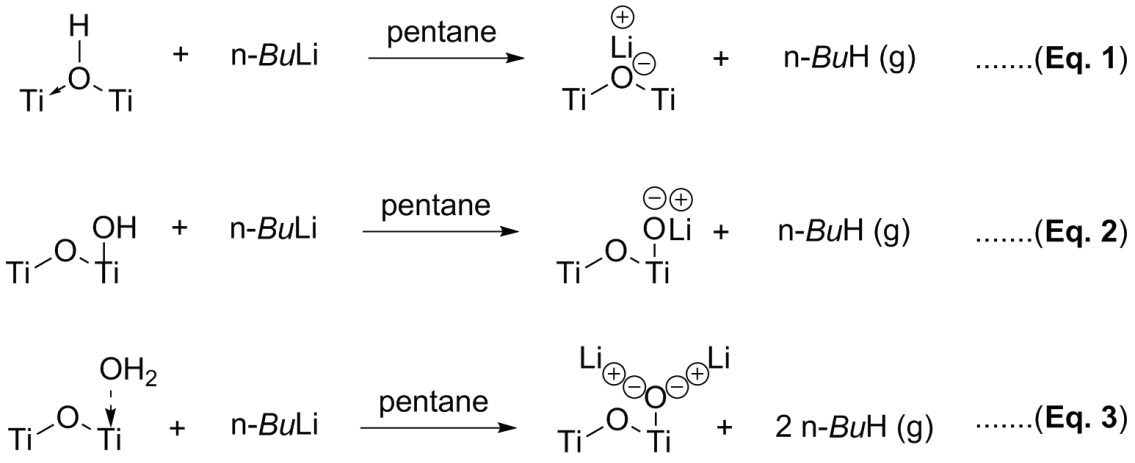

Furthermore, electron paramagnetic resonance spectroscopy was used to identify the paramagnetic centres present on the surface and in the bulk of $TiO_{2(700)}$. Nuclear spins (relative ratio 35%, 25% and 40%) were obtained, corresponding to g values with g_1 = 2.000, g_2 = 1.974 and g_3 = 1.996 respectively. A net total of 21 µmol spins/g of $TiO_{2(700)}$ were calculated form the EPR spectra amongst which 13.7 µmol spins/g belongs to "Ti^{3+}" ions which corresponds to *ca.* 0.1 Ti^{3+}/nm^2. Most of the "Ti^{3+}" ions and oxygen vacancies were found to be present in the bulk of the system rather than on the surface suggesting absence of reductants on the surface of $TiO_{2(700)}$.

Apart from surface hydroxyls, the different crystal planes of TiO_2 when dehydroxylated consists of surface Lewis acidity due to penta coordinated (Ti_{5c}) atoms and weak bronsted

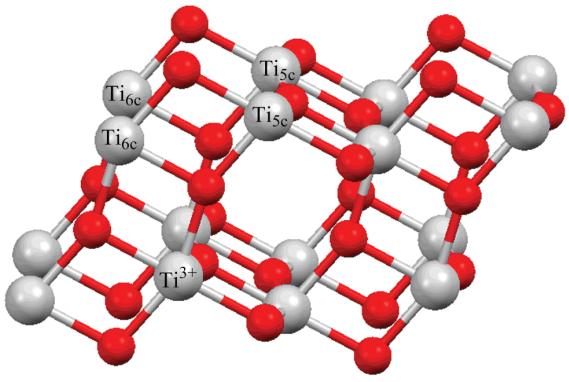

TiO_2 (101)

Ti_{5c} : 5/nm^2 Ti_{6c} : 5/nm^2 Ti^{3+} : 0.1/nm^2

Figure 3 Schematic representation of anatase (101) crystal plane illustrating the presence of surface Lewis acidity (Ti_{5c}) and bulk paramagnetic activity (Ti^{3+} ions).

basicity due to bi coordinated (O_{2c}) atoms. On an average, 5 atoms/nm^2 of Ti_{5C} and O_{2c} are present on the surface irrespective of the crystal plane (Figure 3).

After this qualitative and quantitative characterization of the surface species present on the surface of the anatase, the surface of $TiO_{2(700)}$ was exposed to a tantalum complex. The grafting was accomplished using SOMC technique at room temperature using pentane as a solvent (Eq. 4). The tantalum complex, Ta[-$CH_2C(CH_3)_3$]$_3$[=$CHC(CH_3)_3$] (**1**) was used as a precursor due to the fact that its analogous species grafted on silica partially dehydroxylated at 700°C is very well studied. The grafting reaction between (**1**) and $TiO_{2(700)}$ is controlled by the quantification of the neopentane released during this reaction also indicating the success of the reaction. Once grafted, the bluish gray solid was studied by DRIFT spectroscopy, ^{13}C CPMAS NMR, EPR and EXAFS and by elemental analysis, as well as hydrolysis with degassed water in order to quantify the amount of residual neopentane (Eq5).

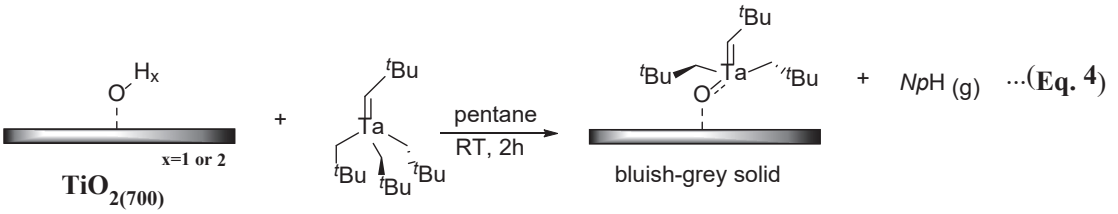

...(**Eq. 4**)

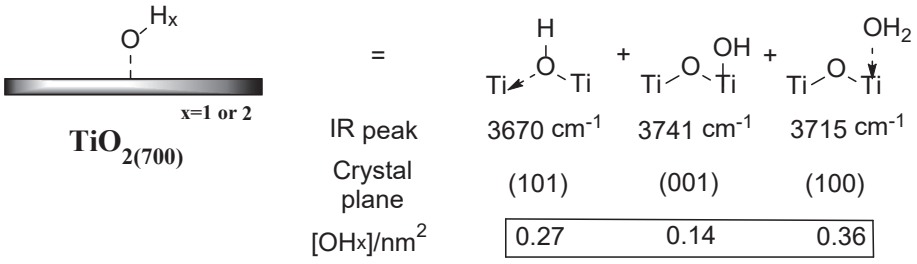

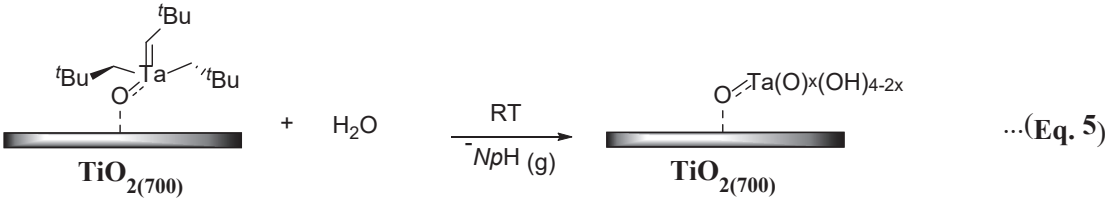

...(**Eq. 5**)

DRIFT spectra of the bluish grey solid showed complete disappearance of surface titanols indicating reactivity between the the metal precursor and the surface. Additionally, elemental analysis showed the presence of 1 Ta/ nm^2 and 14C/Ta demonstrating a full reaction and possibly the formation of monopodal specie as seen in case of $SiO_{2(700)}$. EPR spectra showed an increase in the paramagnetic activity of the solid when compared to $TiO_{2(700)}$, recalling the known "self-doping" phenomena for TiO_2. We can propose in our case a mechanism based on the oxophilic nature ot tantala carbon bond: this can be converted into an oxygen trap leading to the formal reduction of Ti(IV) to "Ti(III)", thus explaining the evolution of the observed EPR spectrum. No relevant information was acquired from the SSNMR of the solid due to its paramagnetic nature. In order to validate this hypothesis, additional tests will be performed with SOMC of $[Ta(OEt)_5]$.

SOMC technique usually creates catalysts with well-defined active sites on substrate surface. But since $TiO_{2(700)}$ in itself has a complex mixture of different crystal planes comprising of different hydroxyls, alongside acidic Ti_{5C} and paramagnetic "Ti(III)" centers and a phenomenon similar to "self-doping", which increases the "Ti(III)" sites, it has proven difficult to utilize SOMC technique with its classical Ta(V) precursor used here to lay the foundations of SOMC on TiO_2. Therefore, the $TiO_{2(700)}$ surface Lewis acidity was exploited by exposing it to a bi-functional coordinating molecule such as 2-methylimidazole (**2-mIm**), to produce a homogeneous surface containing grafting sites after coordination with surface acid sites.

The surface of $TiO_{2(700)}$ was examined *by* DRIFT spectroscopy using pyridine as the basic (monofunctional) probe molecule. Pyridine was adsorbed on $TiO_{2(700)}$ prior to the experiment and DRIFT spectra were studied during the desorption process. At 20°C, 6 different absorption peaks are observed for pyridine adsorbed $TiO_{2(700)}$ in 1200-1700 cm^{-1} range that corresponds to C-C and C-N ring modes. The peak frequency and sharpness of the strong ν_{19b} absorbance which appears at 1445 cm^{-1} corresponds to the C-N-C stretching mode of pyridine. The position of the ν_{19b} absorbance at 1445 cm^{-1} confirms that pyridine molecules are chemisorbed on the Lewis acidic sites of TiO_2 anatase. The frequency of this mode is most strongly affected due to the interaction between the nitrogen lone pair of pyridine molecule and the substrate surface. In the ν(CCN) region, a shoulder on the lower wavenumber side is seen on both the ν_{19a} (peak at 1492 cm^{-1}) and the ν_{19b} (peak at 1445 cm^{-1}) indicating that there is more than one type of Lewis acid site on the TiO_2 surface. The concomitant desorption of pyridine was observed with steady increase in temperature and

lead to relatively complete removal of the N-heterocycle at around 350°C. During, the desorption process, no other peaks appeared indicating no decomposition of pyridine on surface of anatase. The study was found to be coherent with the reported literature and confirms the presence of mainly Lewis acidic sites. Since, no dominant peak corresponding to PyH^+ was observed it can be concluded that the Lewis acid chemistry is prominent on the substrate surface.

A similar study was then carried out with our target molecule *i.e.* 2-mIm to study its interaction with the surface of $TiO_{2(700)}$. The temperature dependent desorption of 2-mIm from $TiO_{2(700)}$ showed that the molecule coordinates to the Lewis acidic sites of the surface with multilayer stacks. The ν_{N-H} streching band at 3505 cm^{-1} showed a maximum intensity around 200°C indicating the isolated nature of the pyrrole. Therefore, for experimental purpose after adsorption of 2-mIm at 120°C on $TiO_{2(700)}$ it was desorbed at 200°C under UHV to obtain a net coordination of 3.5 2-mIm/nm^2 as analysed by elemental analysis. The ^{13}C CPMAS NMR spectra of the resultant solid showed all the peaks coressponding to C's of 2-mIm thus further conforming successful coordination of the linker to the surface. This first monolayer is intended as an interphase to establish fruther SOMC chemistry with organometallic precursors.

Finally, a new versatile support has been developed that can easily adapt to the devices referred to as Photoelectrocatalytic (PEC) cells: TiO_2 nanotubes/Ti mesh based system as fututre support for SOMC. TiO_2 nanotubes (**TNTs**) on a Ti grid have been known to afford better photocatalytic efficiencies compared to TiO_2 powders. This is due to i) higher light absorption due to order in the system; ii) easy electron diffusion from anode to cathode as the nanotubes are supported on Ti metal and iii) higher surface area in a compact setup.[23–27] TiO_2 nanotubes were fabricated on a Ti mesh as it offers a specific surface area, 3-D hierarchical meso/macro porous structure, flexibility and low dependence on the angle of incident light. Anodic oxidation or electrochemical anodization technique was used to synthesize TNTs on Ti mesh. This method forms an array of well-defined, perpendicularly aligned TNTs that originate from the substrate surface (Ti mesh) and hence are electrically connected and easy to handle. Anodization was performed in an electrochemical cell with Pt electrode as a cathode and Ti mesh as an anode. Different applied potential and duration of synthesis were tested to obtain TNTs with different structural parameters. Once anodized, the mesh with amorphous TNTs was calcined at 450°C under air to form crystalline TNTs. The resultant structure offered two types of porosity like hierarchical

porous zeolites: i) a mesoporosity due to the TiO_2 nanotubes having an inner diameter in the range 40-120 nm (as characterized by SEM), ii) a macroporosity due to the meshes of the Ti gauze (80 mesh). For all the samples, once crystallized by calcination, only anatase phase was determined by XRD. UV-Vis. spectra for TNTs-Ti mesh anodized for 1h at 50V showed a broad absorption spectra centred at about 580-600 nm apart from the characteristic absorption in the UV region. This is due to the diffraction and scattering phenomena.

Chronoamperometric measurements were performed for TNTs-Ti mesh anodized at 50V between 20-420 min. under different filters. The sharp increase and decrease of current with light ON/OFF is due to the optical absorption and formation of electron–hole pairs indicating the photoelectrochemical activity of TNTs. The highest value of photocurrent was obtained for the 20 min-anodized sample (0.53 mA cm^{-2}). For the AM 1.5 G filter, that simulates the sunlight received on earth, the 5h sample exhibited higher photocurrent density than others.

In order to evaluate the stability and efficiency of the catalyst, photoelectrocatalysis was performed for all the TNTs-Ti mesh samples anodized at 50 V between 20-420 min. in a photoelectrocatalytic cell (PEC). The TNTs-Ti mesh were assembled with Nafion® and GDL and tested in the PEC device. When the light source is turned on, O_2 is produced in the anodic chamber while the cathodic chamber produces H_2. All the photocatalysts were tested for a period of 5h during which they showed constant and stable water oxidation (mediated by H_2 production). The highest activity in terms of photo water splitting was shown by TNTs-Ti mesh anodized for 5h at 50 V. A maximum H_2 production rate of 0.59 µmol/min. was achieved, giving about 177 µmol in 5 h of light irradiation, while the photo conversion efficiency was higher for the 20-min anodized sample. These performances are in relation with the current state of the art photo-production of H_2 by TNTs on Ti mesh.

In conclusion, we characterized by the SOMC technique the surface of partially dehydoxylated titania anatase nanopowder. The results showed the presence of three types of surface hydroxyls ((a bridging titanol preferentially on crystal plane (101)), a terminal titanol ((a bridging titanol preferentially on crystal plane (001)) and a coordinated water ((a bridging titanol preferentially on crystal plane (100)) in a respective ratio of 1:0.5:1.3 for a total of 0.7 OH/nm^2 on different crystal planes of anatase) along with “Ti(III)” centers (0.1 Ti^{3+}/ nm^2) and mostly, dominant Lewis acidic (*ca.* 5 Ti_{5c}/nm^2) and bronsted basic (O_{2c})

sites. The Ta complex was grafted onto the pre-treated $TiO_{2(700)}$ powder using the SOMC technique. The reaction was analysed by DRIFT and elemental analysis. The presence of different hydroxyls and chemisorbed water on $TiO_{2(700)}$, as well as increase of "Ti(III)" sites, posed difficulties in developing well-defined photocatalysts. The 2-mIm molecule was successfully coordinated to the Lewis acid sites of $TiO_{2(700)}$ as demonstrated by DRIFT, elemental analysis and SSNMR, leaving an accessible NH capable for subsequent surface reaction as a linking site.

Finally, a 3D-hierarchical mesoporous/macroporous TNTs-Ti mesh photocatalyst has been developed as a possible support for exploring the SOMC technique on self-supporting oxide substrates other than powder. The resulting TNTs-Ti showed a vertically aligned ordered array of TiO_2 nanotubes originating from Ti mesh. The sample anodized for 5h at 50 V was the most efficient catalyst among the other samples in terms of H_2 production rate and had a constant and stable activity during a 5h test in the PEC device.

With increasing carbon emissions and ongoing depletion of non-renewable resources, there is a prompt necessity for development and implementation of solar driven chemistry that can help reduce our carbon footprint. This work is a first step in understanding the development of well-defined photocatalyst *via* SOMC pathway that can lead to catalysts combining photocatalysis and heterogeneous chemistry on isolated surface metal atoms.

References

(1) Wernicke, H.-J.; Fischer, R. W. *Chemie Ing. Tech.* **2006**, *78* (7), 825–834.

(2) Somorjai, G. A.; McCrea, K. *Appl. Catal. A Gen.* **2001**, *222* (1–2), 3–18.

(3) Zakharov, V. A.; Yermakov, Y. I. *Catal. Rev.* **1979**, *19* (1), 67–103.

(4) Copéret, C.; Chabanas, M.; Petroff Saint-Arroman, R.; Basset, J.-M. *Angew. Chemie Int. Ed.* **2003**, *42* (2), 156–181.

(5) Basset, J.-M., Psaro, R., Roberto, D., Ugo, R., Eds.; Wiley-VCH Verlag GmbH & Co. KGaA: Weinheim, Germany, **2009**.

(6) Copéret, C.; Comas-Vives, A.; Conley, M. P.; Estes, D. P.; Fedorov, A.; Mougel, V.; Nagae, H.; Núnez-Zarur, F.; Zhizhko, P. A. *Chem. Rev.* **2016**, *116* (2), 323–421.

(7) Aristov. B, Kiselev, A. *Zh. Fiz. Khim.* **1964**, *38* (8), 1984–1989.

(8) Millot, N.; Santini, C. C.; Lefebvre, F.; Basset, J.-M. *Comptes Rendus Chim.* **2004**, *7* (8–9), 725–736.

(9) Bartram, M. E.; Michalske, T. A.; Rogers, J. W. *J. Phys. Chem* **1991**, *95*, 4453–4463.

(10) Gerhard Pfaff; Reynders, P. *Chem. Rev.* **1999**, *99* (7), 1963–1982.

(11) Braun, J. H.; Baidins, A.; Marganski, R. E. *Prog. Org. Coatings* **1992**, *20* (2), 105–138.

(12) Fujishima, a; Honda, K. *Nature* **1972**, *238* (5358), 37–38.

(13) Inoue, Tooru; Fujishima, Akira; Konishi, Satoshi; Kenichi, H. *Nature* **1979**, *277*, 637–638.

(14) Di Paola, A.; Bellardita, M.; Palmisano, L. *Catalysts* **2013**, *3* (1), 36–73.

(15) Mills, A.; Le Hunte, S. *J. Photochem. Photobiol. A Chem.* **1997**, *108* (1), 1–35.

(16) Zhuang, H.; Zhang, Y.; Chu, Z.; Long, J.; An, X.; Zhang, H.; Lin, H.; Zhang, Z.; Wang, X. *Phys. Chem. Chem. Phys.* **2016**, *9636* (18), 9636–9644.

(17) Li, X.; Zhuang, Z.; Li, W.; Pan, H. *Appl. Catal. A Gen.* **2012**, *429–430*, 31–38.

(18) Dvoranová, D.; Brezová, V.; Mazúr, M.; Malati, M. A. *Appl. Catal. B Environ.* **2002**,

37 (2), 91–105.

(19) Transactions, E. C. S.; Society, T. E. **2008**, *3* (43), 1–9.

(20) Yang, L.; Li, Z.; Jiang, H.; Jiang, W.; Su, R.; Luo, S.; Luo, Y. *Appl. Catal. B Environ.* **2016**, *183*, 75–85.

(21) Hamadanian, M.; Karimzadeh, S.; Jabbari, V.; Villagrán, D. *Mater. Sci. Semicond. Process.* **2016**, *41* (JANUARY), 168–176.

(22) Tahir, M.; Amin, N. S. *Energy Convers. Manag.* **2013**, *76*, 194–214.

(23) Roy, P.; Berger, S.; Schmuki, P. *Angew. Chemie - Int. Ed.* **2011**, *50* (13), 2904–2939.

(24) Kontos, A. I.; Likodimos, V.; Stergiopoulos, T.; Tsoukleris, D. S.; Falaras, P.; Rabias, I.; Papavassiliou, G.; Kim, D.; Kunze, J.; Schmuki, P. *Chem. Mater.* **2009**, *21* (4), 662–672.

(25) Nguyen, N. T.; Ozkan, S.; Hwang, I.; Mazare, A.; Schmuki, P. *Nanoscale* **2016**, *8*.

(26) Passalacqua, R.; Ampelli, C.; Perathoner, S.; Centi, G. *Nanosci. Nanotechnol. Lett.* **2012**, *4* (2), 142–148.

(27) Mor, G. K.; Varghese, O. K.; Paulose, M.; Shankar, K.; Grimes, C. A. *Sol. Energy Mater. Sol. Cells* **2006**, *90* (14), 2011–2075.

Resumé

Depuis 90 ans les catalyseurs homogènes et hétérogènes ont été couramment utilisés par les industries chimiques pour la conversion des matières premières.[1,2] Chaque type de catalyseur a des avantages notables tels que, par exemple, des sites actifs identiques et finement modulables pour les catalyseurs homogènes et une grande résistance à la température pour les catalyseurs hétérogènes. Les catalyseurs peuvent cependant rester perfectibles vis-à-vis notamment de l'efficacité, sélectivité, stabilité thermale, et/ou recyclabilité, selon la réaction étudiée.

La chimie organométallique de surface (COMS) est une technique développée dans les années 60[3] et affinée par les ans qui essaye de réduire l'écart entre les catalyseurs hétérogènes et homogènes en produisant des catalyseurs supportés possédant des sites actifs bien définis.[4,5] Cette méthode implique la réaction contrôlée d'un complexe organométallique avec les sites de surface d'un support comme schématisé dans la figure 1. La COMS nous donne la possibilité de développer (dans les cas idéaux) des catalyseurs hétérogènes avec une sphère de coordination aussi bien définie en termes moléculaires qu'en catalyse homogène. Le complexe organométallique greffé peut être utilisé directement comme catalyseur ou bien être traité en présence d'un réactif, gaz inerte ou vide afin d'obtenir des espèces de surface isolées actives.

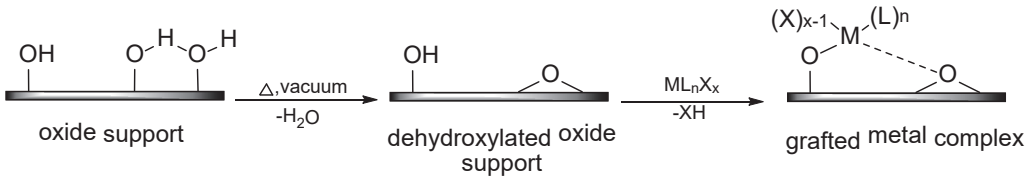

Figure 1 représentation schématique de la préparation de catalyseurs bien définis utilisant la technique COMS sur un oxyde solide possédant une surface correctement décrite par différents hydroxyles de surface.

Une représentation schématique de la construction du catalyseur préparé par COMS et la large variété de complexes métalliques pouvant être utilisés comme agent dopant est donnée ci-dessous (figure 2). Les éléments clés du catalyseur sont : i) Le support, ii) le métal, iii) le ligand fonctionnel et iv) le ligand auxiliaire. Les supports tels que la silice, la silice-alumine, l'alumine, les zéolites, les polymères, etc comprenant différents sites de surface peuvent être utilisés pour greffer des complexes organométalliques comprenant de nombreuses associations métal-ligands.[6] Les éléments de surface greffés sont couramment

caractérisés par des outils d'analyses avancés tels que SSNMR, EXAFS et XANES combinés avec les techniques plus courantes d'IR, GC et analyse élémentaire.

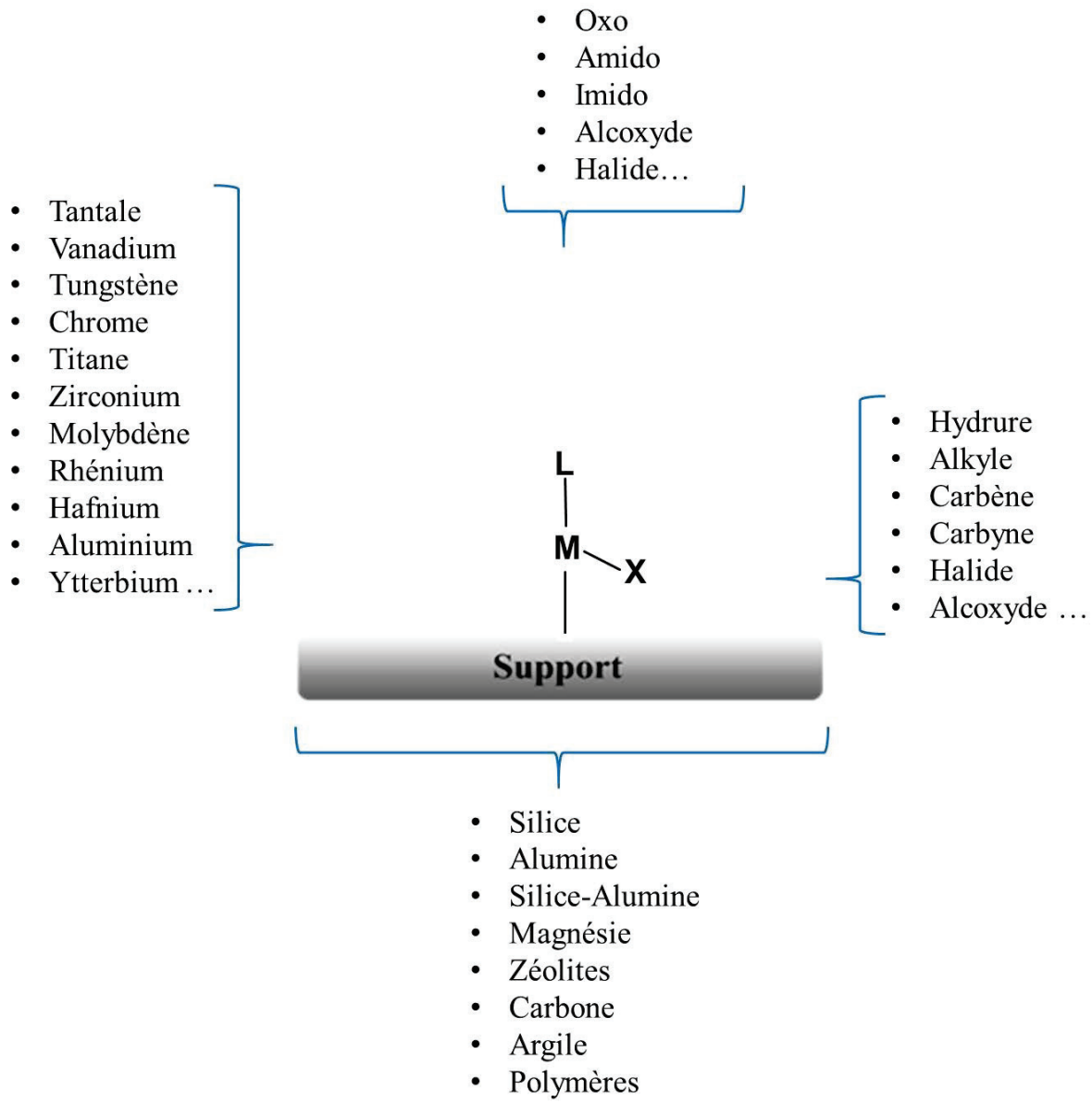

Figure 2 La structure générique des composés organométalliques de surface et la possibilité de porter différents supports possibles, métaux de transition, ligands fonctionnels et spectateurs (seule l'espèce monopodale est montrée pour simplifier, de même, l'aide auxiliaire possible des fragments de surface voisins est omise).

Parmi les nombreux supports, la silice est le support le plus étudiée car elle possède une surface composée de ponts siloxy (≡Si-O-Si≡) et de silanols (≡Si-OH). Les silanols de surface sont principalement divisés en 3 catégories nommées : adjacents, géminés et isolés.[7] La déshydroxylation sous vide dynamique à 150°C conduit à la désorption de l'eau

physisorbée alors que le chauffage à des températures supérieures induit le processus de déshydroxylation où deux groupement hydroxyles adjacents de surface se condensent pour éliminer une molécule d'eau conduisant à un siloxy de surface pontant. Ce processus à 700°C génère des espèces hydroxyles de surface isolées. Une fois analysée qualitativement par spectroscopie DRIFT, l'analyse quantitative des silanols de surface est effectuée par titration chimique. Cette méthode implique la réaction des hydroxyles accessibles avec des alkyles métalliques (n-*Bu*Li) ou des halogénures d'alkyles métalliques (MeMgBr), produisant ainsi des alcanes pouvant être quantifiés par chromatographie en phase gazeuse.[8,9]

Greffer un complexe organométallique sur un support nécessite généralement de strictes conditions anhydres et anaérobiques. Typiquement, un précurseur organométallique avec une configuration M^1—X est choisi en raison de la réaction correspondante **M^1—X + M—OH → M—O—M^1 + HX** thermodynamiquement favorable, avec M-OH correspondant aux groupements hydroxyles du support. De tels catalyseurs COMS sont utilisés dans de nombreuses applications comme la métathèse d'alcanes, la métathèse et la polymérisation d'alcènes. Bien qu'excitantes, la plupart des applications basées sur des catalyseurs COMS sont les conversions de matières fossiles à matières fossiles. Les tendances actuelles dans les émissions de CO_2 et l'usage de procédés non renouvelables ont contraint un changement dans la dynamique énergétique d'une production à partir de matières fossiles vers des transformations issues d'énergies renouvelables, notamment l'énergie solaire.

L'oxyde de titane (TiO_2), largement utilisé comme pigment[10], dans les crèmes solaires, les peintures [11], les pommades, est aussi et surtout dans ce contexte un support photo-actif, ayant permis des applications tels que les vitres autonettoyantes, la décomposition de l'eau[12], la photo-réduction du CO_2[13] etc. Ce composé se présente dans la nature sous principalement trois formes polymorphes : anatase, rutile et brookite. Les polymorphes les plus couramment utilisés sont l'anatase et le rutile avec respectivement une bande interdite de 3.05 eV et 2.98 eV.[14] Même si le rutile possède une bande interdite plus faible, laquelle permet l'absorption dans la région du visible, l'anatase affiche plus de photo-activité. De nombreuses études ont montré que plus l'anatase TiO_2 possède une grande cristallinité, une petite taille de particules, et une grande surface spécifique, meilleure est la photocatalyse.[15] Pour surmonter les limitations de l'anatase, diverses méthodes ont été mises en œuvre telles que le dopage par différents métaux et non-métaux, l'ajout de couches sacrificielles telles que des colorants et la sensibilisation avec de nouvelles enzymes et

polymères.[22] La plupart des applications mentionnées ci-dessus ne se focalisent pas sur le contrôle des interactions surface-dopant. Ceci peut donner lieu à un photo-catalyseur comprenant des sites actifs de surface encombrés, lesquels conduisent finalement à une diminution de l'efficacité photocatalytique globale. L'un des moyens possible pour récupérer cette perte d'efficacité est le développement de photocatalyseurs bien définis avec des sites de surface précis.

La COMS est bien connue pour fournir un contrôle sur le greffage d'agents dopants. La chimie organométallique de surface du titane n'est pas bien connue et seulement quelques exemples ont été décrits dans la littérature. Les précurseurs organométalliques tels que le $(CH_3)_4Sn$, nickelocène, ruthenocène etc ont été greffés en surface de l'anatase.[6] Différentes méthodes de caractérisations ont été utilisées pour comprendre les interactions entre la surface et les centres actifs métalliques lesquelles suivent un mécanisme de transfert de charge du métal sous l'action de photons. Cependant la principale lacune de ces études est l'estimation quantitative des titanols de surface avant de greffer les précurseurs métalliques afin de former un catalyseur bien-défini. Le but de cette thèse est de développer une procédure d'activation fiable conduisant à une structure biendéfinie, et, à partir de ce matériau, obtenir une description qualitative et quantitative des espèces de surface accessible à la COMS.

Afin d'obtenir une surface bien caractérisée pour la COMS, il est nécessaire d'éliminer toute l'eau physisorbée et deshydroxyler partiellement la surface de titane. L'anatase TiO_2 (99,7%, obtenue chez Alfa Aesar, a été calcinée à 450°C sous air afin d'assurer la cristallinité de la poudre et éliminer toutes traces d'impuretés organiques de surface. Elle est par la suite deshydroxylée à 200°C, 500°C et 700°C sous UHV conduisant ainsi à une poudre blanche avec différentes surfaces spécifiques et volumes poreux. La DRX combinée avec la HRTEM suggère la présence de la phase anatase avec un plan cristallin (101) comme espèce prédominante dans $TiO_{2(700)}$. Ces résultats sont en accord avec la construction de Gibbs-Curie-Wulff qui suggère la prédominance du plan cristallin (101) sur d'autres plans avec notamment 1-6% du plan cristallin (001). Les spectres DRIFT ont été utilisés pour analyser les aspects qualitatifs de l'anatase de TiO_2 déshydroxylée à différentes températures.

A 700°C, toute l'eau physisorbée est complètement éliminée et trois pics isolés sont observés entre 3600-3800 cm^{-1}. 12 différents types d'hydroxyles ont été assignés sur

différents plans cristallins d'oxyde de titane dans la littérature, suggérant la nature ambigüe et complexe des hydroxyles de surface. Dans notre travail, le pic à 3670 cm^{-1} a été assigné à un hydroxyle pontant sur la face (101) de l'anatase. Le large pic à 3715 cm^{-1} et le pic fin à 3741 cm^{-1} ont été assignés respectivement à l'eau chimisorbée sur la face (100) et aux hydroxyles terminaux sur la face (001).

Le titrage chimique combiné à l'analyse FTIR a permis la quantification de la concentration des hydroxyles susmentionnés. Un titrage chimique peut être simplement défini comme la réaction entre des hydroxyles de surface et un précurseur organométallique (tel que n-*Bu*Li), le résultat étant un alcane qui peut être quantifié par chromatographie en phase gazeuse (CG). Lorsque $TiO_{2(700)}$ est traité avec n-*Bu*Li, la réaction est supposée suivre une des voies décrites dans les équations Eq.1, Eq.2 et Eq.3; réagissant ainsi avec tous les hydroxyles de surface accessibles et l'eau coordonnée pour produire du butane. La quantification par CG a déterminé la présence d'approximativement 0,73 OH/nm^2, valeur comprise dans un intervalle d'erreur de 10% de la valeur estimée par spectroscopie FTIR (~ 0,8 OH/nm^2).

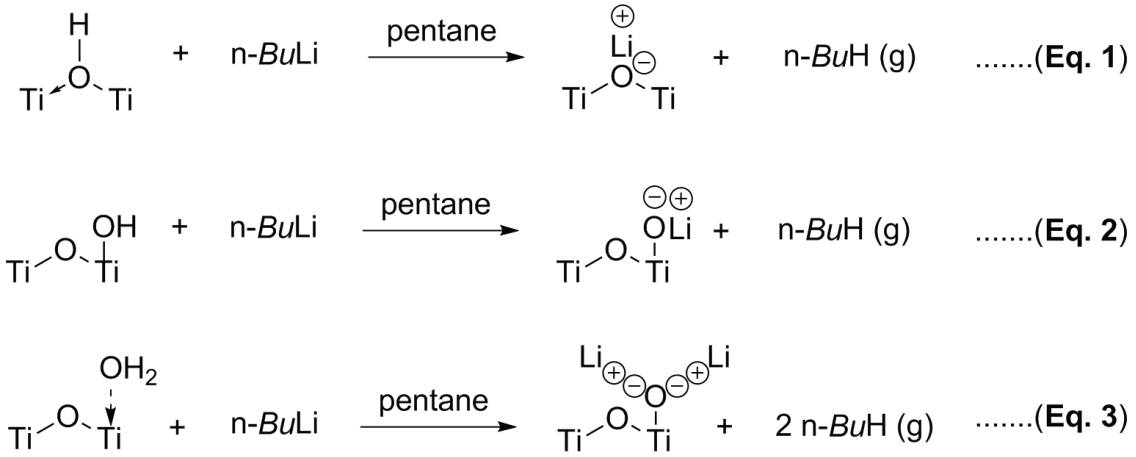

En outre, la spectroscopie par résonance paramagnétique électronique a été utilisée pour identifier les centres paramagnétiques présents dans le réseau et la surface de $TiO_{2(700)}$. Des spins nucléaires (en rapport relatif 35%, 25% et 40%) ont été obtenus, correspondant respectivement à des valeurs de g avec $g_1 = 2.000$, $g_2 = 1.974$ et $g_3 = 1.996$. Un total net de 21 µmol spins/g de $TiO_{2(700)}$ a été calculé à partir des spectres EPR parmi lesquels 13,7 µmol spins/g appartiennent aux ions "Ti^{3+}" correspondant à env. 0,1 Ti^{3+}/nm^2. La plupart des ions "Ti^{3+}" et des lacunes d'oxygène se sont avérés être présents dans le réseau du

système plutôt qu'en surface, suggérant ainsi l'absence de réducteurs à la surface du $TiO_{2(700)}$.

Mis à part les hydroxyles de surface, les différents plans cristallins de TiO_2, lorsqu'ils sont deshydroxylés, sont constitués d'une acidité superficielle de Lewis due à des atomes penta coordonnés (Ti_{5c}) et à une faible basicité de Bronsted due à des atomes bi-coordonnés (O_{2c}). En moyenne, 5 atomes/nm^2 de Ti_{5c} et O_{2c} sont présents sur la surface quel que soit le plan cristallin (Figure 3).

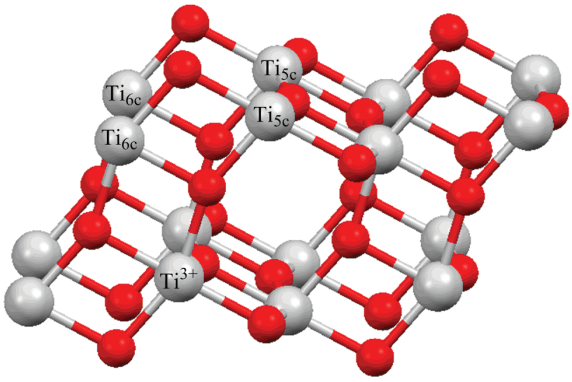

TiO_2 (101)

Ti_{5c} : 5/nm^2 Ti_{6c} : 5/nm^2 Ti^{3+} : 0.1/nm^2

Figure 3 Représentation schématique du plan cristallin de l'anatase (101) illustrant la présence de l'acidité superficielle de Lewis (Ti_{5c}) et de l'activité paramagnétique globale (ions Ti^{3+}).

Après cette caractérisation qualitative et quantitative des espèces de surface présentes à la surface de l'anatase, la surface de $TiO_{2(700)}$ a été exposée à un complexe de tantale. Le greffage est effectué par la technique de COMS à température ambiante utilisant le pentane comme solvant (Eq.4). Le complexe, $Ta[-CH_2C(CH_3)_3]_3[=CHC(CH_3)_3]$ (**1**) a été utilisé comme précurseur en raison du fait que son espèce analogue greffée sur silice partiellement deshydroxylée à 700°C est très bien étudiée. La réaction de greffage entre **1** et $TiO_{2(700)}$ est contrôlée par la quantification du néopentane relâché au cours de cette réaction indiquant également le succès de la réaction. Une fois greffé, le solide gris bleuté est été étudié par spectroscopies DRIFT, ^{13}C CPMAS RMN, RPE et EXAFS et par analyse élémentaire, ainsi que l'hydrolyse avec de l'eau dégazée afin de quantifier la quantité de néopentane résiduelle (Eq. 5).

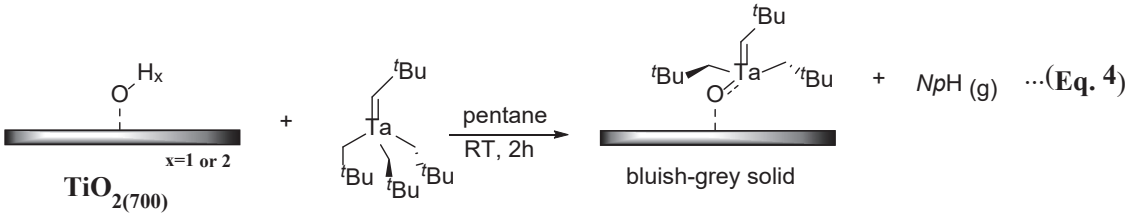

...(**Eq. 4**)

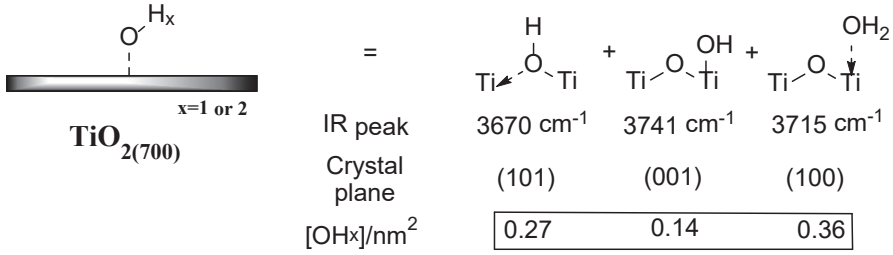

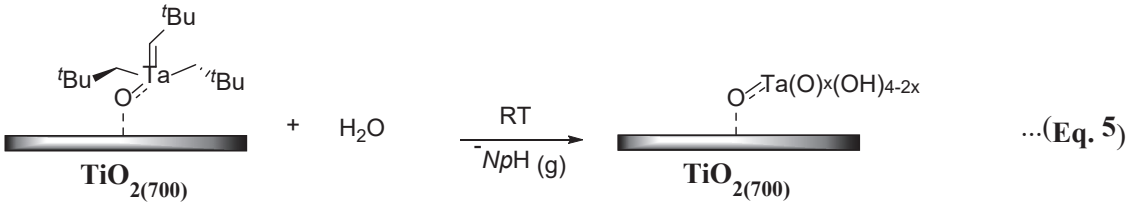

...(**Eq. 5**)

Les spectres DRIFT du solide ont montré une disparition complète des fonctions –OH de surface indiquant la réactivité entre le précurseur et la surface. De plus, l'analyse élémentaire a montré la présence de 1Ta/nm^2 et 14C/Ta démontrant une réaction complète et éventuellement la formation d'espèces monopodales comme dans le cas de $SiO_{2(700)}$. Les spectres RPE ont montré une augmentation de l'activité paramagnétique du solide par rapport au $TiO_{2(700)}$), rappelant les phénomènes d' « auto-dopage » connus pour TiO_2.On peut proposer dans notre cas un mécanisme basé sur la nature oxophile de la liaison carbone tantale : celle-ci peut se transformer en piège à oxygène conduisant à la réduction formelle de Ti(IV) en "Ti(III)", expliquant ainsi l'évolution du spectre RPE observée. Aucune information pertinente n'a été acquise à partir du SSNMR du solide en raison de sa nature paramagnétique. Afin de valider cette hypothèse, des essais supplémentaires seront réalisés en utilisant COMS $Ta(OEt)_5$.

La technique COMS crée des catalyseurs avec des sites actifs bien définis sur la surface du substrat. Mais comme $TiO_{2(700)}$ possède un mélange complexe de différents plans cristallins

comprenant différents hydroxyles, de sites acides Ti_{5c} et de centres paramagnétiques de "Ti(III)", et un phénomène similaire à l' « auto-dopage », qui augmente les sites de "Ti(III)" a lieu, il s'est avéré difficile d'utiliser la technique COMS avec son précurseur classique de Ta(V) utilisé ici pour poser les fondations de la COMS sur TiO_2. Par conséquent, l'acidité de Lewis de surface de $TiO_{2(700)}$ a été exploitée en l'exposant à une molécule coordonnante bi fonctionnelle telle que le 2-méthylimidazole (**2-mIm**), pour produire une surface homogène présent encore des sites de greffage après coordination sur les sites acides de surface.

La surface de $TiO_{2(700)}$ a été premièrement examinée par spectroscopie DRIFT en utilisant la pyridine comme molécule sonde basique (monofonctionnelle). La pyridine a été adsorbée sur $TiO_{2(700)}$ avant l'expérience et les spectres DRIFT ont été étudiés pendant le processus de désorption. A 20°C, 6 pics d'absorption différents sont observés pour pyridine adsorbée sur $TiO_{2(700)}$ entre 1200-1700 cm^{-1} qui correspond aux modes cycliques C-C et C-N. La forte absorbance ν_{19b} qui apparaît à 1445 cm^{-1} correspond au mode d'étirement C-N-C de la pyridine. La position de l'absorbance ν_{19b} à 1445 cm^{-1} confirme que la pyridine est chimisorbée sur les sites acides de Lewis. Dans la région ν(CCN), un épaulement est observé à la fois sur le ν_{19a} (pic à 1492 cm^{-1}) et le ν_{19b} (pic à 1445 cm^{-1}) indiquant qu'il y a plusieurs types de sites acides sur la surface de TiO_2. La désorption de la pyridine a été observée en fonction de la température, pour une désorption totale du N-hétérocycle à environ 350°C. Au cours du processus de désorption, aucun autre pic n'est apparu excluant la décomposition de la pyridine. L'étude s'est révélée cohérente avec la littérature rapportée et confirme la présence principalement de sites acides de Lewis. Comme aucun pic dominant correspondant à PyH^+ n'a été observé, on peut conclure que la chimie de l'acide de Lewis est proéminente sur la surface du substrat.

Une étude similaire a ensuite été effectuée avec notre molécule cible, le 2-mIm, pour étudier son interaction avec la surface de $TiO_{2(700)}$. La désorption en fonction de la température de 2-mIm à partir de $TiO_{2(700)}$ a montré que la molécule se coordonne aux sites acides de Lewis de la surface avec des empilements multicouches. L'élongation de la bande ν_{N-H} à 3505 cm^{-1} a montré une intensité maximale autour de 200°C témoignant alors d'espèces isolées en surface (c'est-à-dire en configuration monocouche). Par conséquent, cette température a été choisie pour la synthèse de 2-mIm@$TiO_{2(700)}$: après adsorption de 2-mIm à 120°C sur $TiO_{2(700)}$, le matériau a été désorbé à 200°C sous UHV, l'analyse élémentaire montre une coordination de 3,5 2-mIm/nm^2. Les spectres RMN ^{13}C CPMAS du solide confirment la

coordination de la molécule à la surface par les pics de C's de 2-mIm. Cette première monocouche est conçue comme une interphase pour établir une chimie COMS avec des précurseurs organométalliques.

Enfin, un nouveau support a été développé polyvalent qui peut facilement s'adapter aux dispositifs finaux visés, les cellules photoélectriques (PEC): des nanotubes de TiO_2 sur une gaze de Ti comme futur support pour COMS. Les nanotubes de TiO_2(**TNTs**) sur une grille de Ti sont connus pour donner de meilleurs rendements photocatalytiques par rapport aux poudres de TiO_2. Ceci est dû à i) une absorption de lumière plus élevée; ii) diffusion plus aisée des électrons de l'anode à la cathode lorsque les nanotubes sont supportés sur Ti métal et iii) surface plus importante.[23–27] Les nanotubes de TiO_2 ont été fabriqués sur gaze de Ti car ils offrent une surface spécifique non nulle, 3-D structure méso / macro poreuse, flexibilité. Une technique d'anodisation électrochimique a été utilisée pour synthétiser des TNT sur gaze de Ti. Cette méthode forme un réseau de TNT bien définis, perpendiculaires et alignés. L'anodisation a été effectuée dans une cellule électrochimique avec une électrode de Pt en tant que cathode et une gaze de Ti en tant qu'anode. Différents potentiels appliqués et la durée de la synthèse ont été testés pour obtenir des TNT avec différents structures. Une fois anodisé, la gaze avec des TNT amorphes a été calcinée à 450°C sous air pour former des TNTs cristallins. La structure résultante donne deux types de porosité comme les zéolites poreuses: i) une mésoporosité due aux nanotubes de TiO_2 ayant un diamètre interne compris entre 40 et 120 nm (tel que caractérisé par SEM), ii) une macroporosité due à la gaze de départ du Ti (80 mesh). Pour tous les échantillons, une fois cristallisés par calcination, seule la phase anatase a été déterminée par DRX. Les spectres UV-Vis pour les TNTs-Ti anodisés pendant 1h à 50V ont montré un large spectre d'absorption centré à environ 580-600 nm en dehors de l'absorption caractéristique dans la région UV. Ceci est dû aux phénomènes de diffraction et de diffusion de photocatalyseurs.

Des mesures chrono-ampérométriques ont été réalisées pour TNT-Ti mesh anodisées à 50 V entre 20 et 420 min. sous différents filtres. La forte augmentation et diminution du courant avec la lumière ON/OFF est due à l'absorption optique et à la formation de paires électron-trou indiquant l'activité photoélectrochimique des TNT. La valeur la plus élevée du photocourant a été obtenue pour l'échantillon anodisé pendant 20 min (0,53 $mAcm^{-2}$). Pour le filtre AM 1.5 G, qui mime la lumière du soleil, l'échantillon 5h a affiché une densité de photocourant plus grande que les autres.

Afin d'évaluer la stabilité et l'efficacité du catalyseur, une photoélectrocatalyse a été réalisée pour tous les échantillons TNTs-Ti mesh anodisés à 50 V entre 20-420 min. dans une cellule photoélectrocatalytique (PEC). Les TNTs-Ti ont été assemblés avec Nafion® et GDL et testés dans le dispositif PEC. Lorsqu'il y a une source de lumière, O_2 est produit dans la chambre anodique tandis que la chambre cathodique produit H_2. Tous les photocatalyseurs ont été testés pendant une période de 5h au cours de laquelle ils ont montré une oxydation de l'eau constante et stable (par la production de H_2). L'activité la plus élevée en termes de photo splitting de l'eau a été démontrée par un TNTs-Ti mesh anodisé pendant 5h à 50 V. Un taux de production maximum de H_2 de 0,59 μmol/min. a été atteint, donnant environ 177 μmol en 5 h d'irradiation lumineuse, tandis que l'efficacité de la conversion photo était plus élevée pour l'échantillon anodisé de 20 min. Ces performances sont à l'état de l'art actuel vis-à-vis de la photoproduction de H_2 par TNT sur gaze de Ti.

En conclusion, nous avons caractérisé par la technique COMS la surface de la nanopoudre d'oxyde de titane partiellement déshydroxylée. Les résultats ont montré la présence de trois types d'hydroxyles de surface (un titanol ponté préférentiellement sur le plan cristallin (101), un titanol terminal préférentiellement sur le plan cristallin (001) et une molécule d'eau coordonnée préférentiellement sur le plan cristallin (100) dans un rapport respectif de 1: 0,5: 1,3 pour un total de 0,7 OH /nm^2), de centres "Ti(III)" (0,1 Ti^{3+}/nm^2) ainsi que , majoritairement (ca. 5 /nm^2), des sites dominants acide de Lewis (Ti_{5c}) et basique (O_{2c}). Le complexe Ta a été greffé sur la poudre $TiO_{2(700)}$ pré-traitée en utilisant la technique COMS. La réaction a été analysée, *inter alia*, par DRIFT et l'analyse élémentaire. La présence de différents hydroxyles et d'eau chimisorbée sur $TiO_{2(700)}$, ainsi que l'augmentation de sites de "Ti(III)" ont posé des difficultés pour développer des photocatalyseurs bien définis. La molécule 2-mIm a été coordonné avec succès aux sites acides de Lewis de $TiO_{2(700)}$ comme démontré par DRIFT, analyse élémentaire et SSNMR en laissant accessible pour une réaction de surface successive une liaison N-H pouvant agir comme site d'encrage.

Enfin, un photocatalyseur TNTs-Ti mésoporeux / macroporeux à la structure 3D a été devellopé comme un support possible pour explorer la technique COMS sur des supports auto-portant d'oxyde autres que la poudre. Le TNTs-Ti résultant, présentait un réseau ordonné aligné verticalement de nanotubes de TiO_2 provenant de la gaze de Ti. L'échantillon anodisé pendant 5 h à 50 V était le catalyseur le plus performant parmi les

autres échantillons en termes de taux de production d'H_2 et avait une activité constante et stable pendant un test de 5h dans le dispositif PEC.

Avec l'augmentation des émissions de carbone et l'épuisement continu des ressources non renouvelables, il y a une nécessité rapide pour le développement et la mise en œuvre de la chimie solaire qui peut aider à réduire notre empreint carbone. Ce travail est une première étape dans la compréhension du développement d'un photocatalyseur bien défini par voie COMS qui peut conduire à des catalyseurs combinant la photocatalyse et la chimie hétérogène sur atome de métal de surface isolé.

References

(1) Wernicke, H.-J.; Fischer, R. W. *Chemie Ing. Tech.* **2006**, *78* (7), 825–834.

(2) Somorjai, G. A.; McCrea, K. *Appl. Catal. A Gen.* **2001**, *222* (1–2), 3–18.

(3) Zakharov, V. A.; Yermakov, Y. I. *Catal. Rev.* **1979**, *19* (1), 67–103.

(4) Copéret, C.; Chabanas, M.; Petroff Saint-Arroman, R.; Basset, J.-M. *Angew. Chemie Int. Ed.* **2003**, *42* (2), 156–181.

(5) Basset, J.-M., Psaro, R., Roberto, D., Ugo, R., Eds.; Wiley-VCH Verlag GmbH & Co. KGaA: Weinheim, Germany, **2009**.

(6) Copéret, C.; Comas-Vives, A.; Conley, M. P.; Estes, D. P.; Fedorov, A.; Mougel, V.; Nagae, H.; Núnez-Zarur, F.; Zhizhko, P. A. *Chem. Rev.* **2016**, *116* (2), 323–421.

(7) Aristov. B, Kiselev, A. *Zh. Fiz. Khim.* **1964**, *38* (8), 1984–1989.

(8) Millot, N.; Santini, C. C.; Lefebvre, F.; Basset, J.-M. *Comptes Rendus Chim.* **2004**, *7* (8–9), 725–736.

(9) Bartram, M. E.; Michalske, T. A.; Rogers, J. W. *J. Phys. Chem* **1991**, *95*, 4453–4463.

(10) Gerhard Pfaff; Reynders, P. *Chem. Rev.* **1999**, *99* (7), 1963–1982.

(11) Braun, J. H.; Baidins, A.; Marganski, R. E. *Prog. Org. Coatings* **1992**, *20* (2), 105–138.

(12) Fujishima, a; Honda, K. *Nature* **1972**, *238* (5358), 37–38.

(13) Inoue, Tooru; Fujishima, Akira; Konishi, Satoshi; Kenichi, H. *Nature* **1979**, *277*, 637–638.

(14) Di Paola, A.; Bellardita, M.; Palmisano, L. *Catalysts* **2013**, *3* (1), 36–73.

(15) Mills, A.; Le Hunte, S. *J. Photochem. Photobiol. A Chem.* **1997**, *108* (1), 1–35.

(16) Zhuang, H.; Zhang, Y.; Chu, Z.; Long, J.; An, X.; Zhang, H.; Lin, H.; Zhang, Z.; Wang, X. *Phys. Chem. Chem. Phys.* **2016**, *9636* (18), 9636–9644.

(17) Li, X.; Zhuang, Z.; Li, W.; Pan, H. *Appl. Catal. A Gen.* **2012**, *429–430*, 31–38.

(18) Dvoranová, D.; Brezová, V.; Mazúr, M.; Malati, M. A. *Appl. Catal. B Environ.* **2002**,

37 (2), 91–105.

(19) Transactions, E. C. S.; Society, T. E. **2008**, *3* (43), 1–9.

(20) Yang, L.; Li, Z.; Jiang, H.; Jiang, W.; Su, R.; Luo, S.; Luo, Y. *Appl. Catal. B Environ.* **2016**, *183*, 75–85.

(21) Hamadanian, M.; Karimzadeh, S.; Jabbari, V.; Villagrán, D. *Mater. Sci. Semicond. Process.* **2016**, *41* (JANUARY), 168–176.

(22) Tahir, M.; Amin, N. S. *Energy Convers. Manag.* **2013**, *76*, 194–214.

(23) Roy, P.; Berger, S.; Schmuki, P. *Angew. Chemie - Int. Ed.* **2011**, *50* (13), 2904–2939.

(24) Kontos, A. I.; Likodimos, V.; Stergiopoulos, T.; Tsoukleris, D. S.; Falaras, P.; Rabias, I.; Papavassiliou, G.; Kim, D.; Kunze, J.; Schmuki, P. *Chem. Mater.* **2009**, *21* (4), 662–672.

(25) Nguyen, N. T.; Ozkan, S.; Hwang, I.; Mazare, A.; Schmuki, P. *Nanoscale* **2016**, *8*.

(26) Passalacqua, R.; Ampelli, C.; Perathoner, S.; Centi, G. *Nanosci. Nanotechnol. Lett.* **2012**, *4* (2), 142–148.

(27) Mor, G. K.; Varghese, O. K.; Paulose, M.; Shankar, K.; Grimes, C. A. *Sol. Energy Mater. Sol. Cells* **2006**, *90* (14), 2011–2075.

Riassunto

Per più di novant'anni catalizzatori eterogenei ed omogenei sono stati al servizio delle industrie chimiche, facilitando, per esempio, la conversione di bulk feedstock in prodotti di chimica fine.[1,2] Nonostante entrambi i tipi di catalizzatori presentino dei vantaggi, quali, ad esempio, la presenza di siti attivi identici ed altamente modulabili per i catalizzatori omogenei e l'alta stabilità termica e riciclabilità per i catalizzatori eterogenei. Ci sono tuttavia degli aspetti a cui si potrebbero apportare dei miglioramenti, come l'efficienza, la selettività, la stabilità termica, la riciclabilità del catalizzatore stesso, ecc. La chimica organometallica di superfice, SOMC, tecnica sviluppata negli anni 60[3] e raffinata nel corso degli anni, stabilisce un ponte tra la catalisi omogenea ed eterogenea producendo catalizzatori supportati con siti attivi ben definiti.[4,5] Il metodo prevede la reazione controllata di un complesso organometallico con i gruppi funzionali presenti sulla superficie di un supporto, come mostrato in Figura 1. La tecnica SOMC permette di sviluppare (nel caso ideale) dei catalizzatori eterogenei con una sfera di coordinazione definita da un punto di vista molecolare come nel caso della catalisi omogenea. Il complesso organometallico così immobilizzato sulla superficie può essere direttamente utilizzato come catalizzatore senza ulteriori modifiche, oppure può essere trattato in presenza di alto vuoto o un secondo reagente, per ottenere delle nuove specie isolate cataliticamente attive.

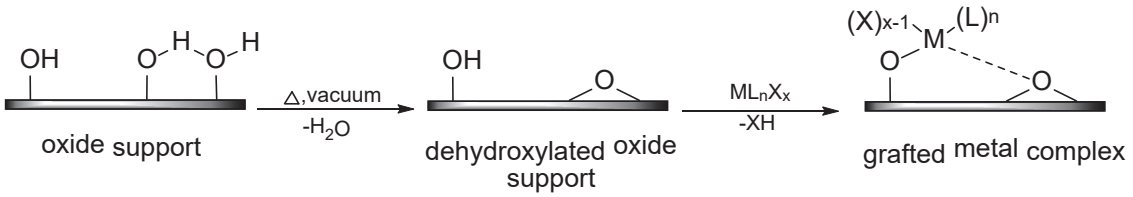

Figura 1 Rappresentazione schematica della preparazione di un catalizzatore dalla struttura ben definita ultizzando le tecniche SOMC su di un ossido solido, la cui superficie può essere descritta correttamente dalla presenza di una collezione di gruppi idrossilici.

In Figura 2 è riportata una rappresentazione schematica della sintesi di un catalizzatore tramite tecniche SOMC e della grande varietà di complessi metallici che possono essere utilizzati come agenti dopanti. I componenti chiave per la sintesi del catalizzatore sono: i) il supporto, ii) il metallo, iii) il legante funzionale e iv) il legante ancillare. Diversi materiali che presentano differenti siti attivi sulla propria superficie, eg. silice, silice-allumina, allumina, zeoliti, alcuni tipi di polimeri, possono essere utilizzati come supporti per il grafting di complessi organometallici, che a loro volta possono presentare diverse

configurazioni metallo-legando.[6] I frammenti graftati sulla superficie sono solitamente caratterizzati tramite metodi avanzati quali NMR allo stato solido, EXAFS e XANES uniti a metodi più comuni quali IR, GC e analisi elementare.

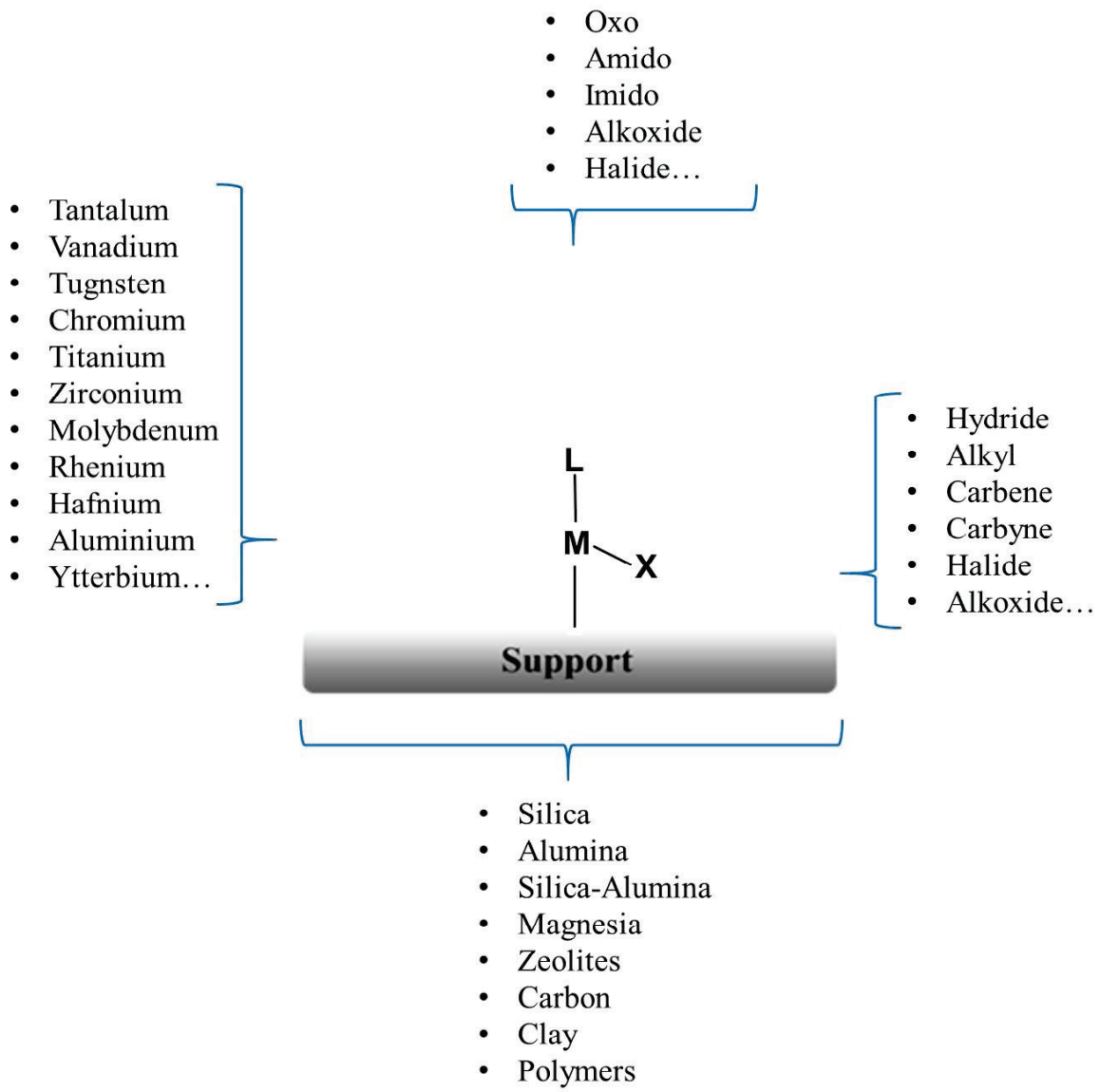

Figura 2 Schema descrittivo della generica struttura dei complessi organometallici di superficie e dell'ampia scelta tra supporti, metalli di transizione, legandi funzionali e spettatori (per semplicità è mostrata solo una specie monopodale, viene omessa per lo stesso motivo anche la possibile assistenza ancillare di specie vicinali caratteristiche della superficie).

La silice è uno dei supporti più studiati. La sua superficie consiste di ponti silossano (≡Si-O-Si≡) e silanoli (≡Si-OH). I silanoli presenti sulla superficie sono divisi principalemnte in tre categorie: geminali, vicinali e isolati.[7] La deidrossilazione della silice in condizioni di

vuoto dinamico a 150°C porta all'allontanamento dell'acqua fisisorbita sulla superficie, mentre il trattamento a temperature più elevate porta al processo di deidrossilazione, dove due gruppi idrossilici vicinali condensano per eliminare una molecola d'acqua e dare un ponte silossano. Questo processo di deidrossilazione condotto a 700°C genera gruppi idrossilici isolati sulla superficie. Dopo un'analisi qualitativa tramite spettrosopia DRIFT, la stima quantitativa dell'abbondanza dei silanoli sulla superficie è condotta tramite una titolazione quantitativa. Il metodo prevede la reazione degli idrossili accessibili con metallo-alchili (*n*-BuLi) o alogenuri achilici (MeMgBr) portando all'evoluzione di alcani come prodotto secondario di reazione, questi ultimi risultano poi essere facilmente quantificabili tramite cromatografia in fase gas.[8,9]

Il greffaggio di un complesso organometallico su di un supporto richiede tipicamente condizioni strettamente anidre e anaerobiche. Generalmente, un precursore organometallico di configurazione M^1-X è scelto in maniera tale che la reazione **M^1-X + M-OH $\rightarrow$ M-O-M^1 + HX** sia termodinamicamente favorita, dove M-OH è il gruppo idrossilico presente sulla superficie. Catalizzatori SOMC di questo tipo sono stati utilizzati per diverse applicazioni quali metatesi di alcani e olefine e polimerizzazione di olefine. Anche se altamente interessante, la maggior parte delle applicazioni di questo tipo di catalizzatori restano nel campo della conversione del fossile. Le preoccupazioni attuali circa le emissioni di CO_2 e dell'utilizzo di risorse non rinnovabili hanno portato alla necessità di uno sfruttamento di fonti di energia rinnovabile, quali l'energia solare.

La titania o TiO_2, ampiamente utilizzata come pigmento[10], in creme solari, pitture[11], unguenti, è anche e soprattutto un supporto fotoattivo, proprietà che ne ha permesso l'applicazione in contesti quali finestre autopulenti, splitting dell'acqua[12], fotoriduzuine della CO_2[13], ecc. In natura esiste generalemte in tre polimorfi: anatasio, rutilo e brookite. I due polimorfi più utilizzati sono l'anatasio e il rutilo, che presentano un band gap rispettivamente di 3.05 eV e 2.98 eV.[14] Anche se il rutilo ha un band gap minore, che permette l'assorbimento nella regione del visibile, l'anatasio mostra una fotoattività maggiore. Molti studi hanno indicato che questa maggiore fotoattività puo' essere legata alla cristallinità maggiore, alla minore dimensione delle particelle e all' area superficiale maggiore dell'anatasio.[15] Per ulteriormente migliorarne l'attività fotocatalitica sono stati utlizzati differenti metodi, quali doping con diversi metalli o non metalli, l'aggiunta di agenti sacrificali quali coloranti.[22] Le applicazioni basate sulle tecniche di modificazione di superficie menzionate precedentemente non sono generalmente incentrate sul controllo

dell'interazione superficie-agente dopante. Questo può portare a fotocatalizzatori che presentano sulla superficie siti attivi ingombrati, fatto che porta come conseguenza una diminuzione dell'efficienza fotocatalitica complessiva. Uno dei modi possibili per recuperare questa perdita di efficienza è quello di sviluppare un fotocatalizzatore con siti attivi ben definiti sulla superficie.

Le tecniche SOMC sono note per fornire un certo grado di controllo nel grafting di dopanti. La titania, come supporto per le tecniche SOMC, non è stata ancora approfonditamente studiata. Esistono solamente pochi esempi in letteratura di SOMC@TiO_2 : i precursori organometallici come $(CH_3)_4Sn$, nickeloceni, rutenoceni, ecc. sono stati fatti reagire con la superficie dell'anatasio.[6] Sono stati utilizzati diversi metodi di caratterizzazione per comprendere l'interazione tra la le specie metalliche presenti sulla superficie e le specie metalliche attive innescata dall'esposizione a fotoni, e che segue un meccanismo di trasferimento di carica metallo-metallo. Quello che però manca nella maggior parte di questi studi, è la quantificazione dei titanoli presenti sulla superficie prima del grafting dei precursori metallici. Inoltre monitorare la reazione tramite la stima quantitativa di prodotti organici rilasciati durante il grafting può dare informazioni decisive sulla struttura delle specie formate sulla superficie della titania. L'obiettivo di questa tesi è sviluppare una procedura di attivazione affidabile che porti ad una struttura ben definita, combinata ad una descrizione qualitativa e quantitativa delle specie reattive per la SOMC.

Per ottenere una superficie ben caratterizzata su cui utilizzare le tecniche SOMC, è stato necessario eliminare tutta l'acqua fisisorbita sulla supreficie e deidrossilare parzialmente la superficie stessa della titania. La TiO_2 anatase (99.7%) commercializzata da alfa aesar è stata calcinata a 450°C sotto aria per assicurare la cristallinità della polvere e per eliminare le impurità orgniche presenti sulla superficie (nel caso ci fossero state). La polvere è stata quindi deirossilata parzialmente a 200°C, 500°C e 700°C sotto UHV per ottenere una polvere bianca, $TiO_{2(700)}$, con diverse aree superficiali e volumi dei pori. Tecniche XRD in combinazione con HRTEM hanno suggerito la presenza dell'anatasio con piani cristallini (101) come piani predominianti per la $TiO_{2(700)}$. Questi risultati sono in linea con la costruzione Gibbs-Curie-Wulff che suggeriva la predominanza dei piani cristallini (101) sugli altri piani, con un 1-6 % di piani cristallini (001).

La spettroscopia DRIFT è stata utilizzata per analizzare qualitativamente la TiO_2 anatase deidrossilata a diverse temperature. A 700°C, tutta l'acqua fisisorbita è stata allontanata ed

è stato possibile osservare tre picchi isolati nella regione 3600-3800 cm^{-1}. In letteratura sono stati identificati dodici diversi tipi di idrossili su differenti piani cristallini della titania, suggerendo l'ambigua e complessa natura degli idrossili presenti sulla superficie. Nel nostro lavoro , il picco a 3670 cm^{-1} è stato assegnato ad un idrossile a ponte su di un piano (101) dell'anatase. Il picco largo a 3715 cm^{-1} e il picco fine a 3741 cm^{-1} sono stati assegnati rispettivamente a molecole di H_2O chemisorbita sulle facce (100) e idrossili terminali sulle facce (001).

La titolazione chimica combinata con analisi FTIR ha permesso la quantificazione dei gruppi idrossilici precedentemente menzionati. Una titolazione chimica può essere semplicemente definita come la reazione tra gli idrossili presenti sulla superficie e un precursore organometallico (come *n*-BuLi), che porta alla produzione di un alcano che può essere quantificato utlilizzando la cromatografia in fase gas (GC). Quando la $TiO_{2(700)}$ è stata trattata con *n*-BuLi è stato supposto che la rezione seguisse il percorso di reazione descritto nelle Eq.1, Eq.2 e Eq.3, reagendo con tutti gli idrossili accessibili e l'acqua coordinata sulla superficie per produrre butano. La quantificazione GC ha portato ad una stima di 0.73 OH/nm^2 che ricade all'interno alla barra di errore del 10% del valore ottenuto tramite spettroscopia FTIR (~ 0.8 OH/nm^2).

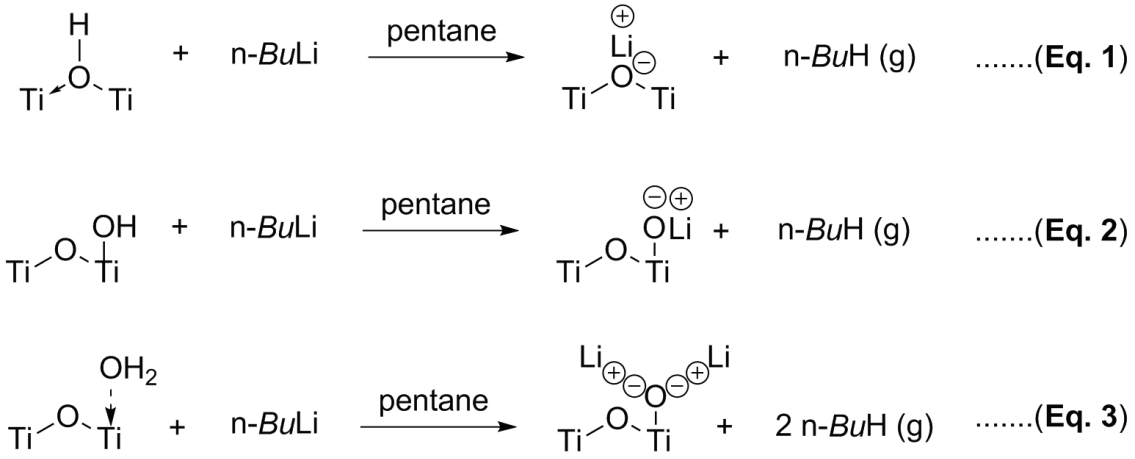

Inoltre, è stata utilizzata la spettroscopia di risonanza elettronica paramagnetica per identificare i centri paramagnetici presenti sulla superficie e nel bulk della $TiO_{2(700)}$. Sono stati ottenuti valori di spin nucleari (in rapporto relativo 35%, 25% e 40%) che corrispondono rispettivamente a valori g di g_1=2.000, g_2=1.974 e g_3=1.996. Un totale netto di 21 μmol spins/g di $TiO_{2(700)}$ è stato ottenuto dagli spettri EPR di cui 13.7 μmol spins/g appartengono a ioni "Ti^{3+}" che corrisponde a circa 0.1 Ti^{3+}/nm^2. La maggior parte degli

ioni "Ti^{3+}" e le vacanze di ossigeno sono state riscontrate nel bulk del sistema e non sulla superfice, suggerendo l'assenza di riducenti sulla superficie della $TiO_{2(700)}$.

Oltre a gruppi idrossilici di superficie, i diversi piani cristallini della TiO_2, quando deidrossilati, presentano un carattere acido di Lewis sulla superficie dovuta ad atomi di titanio pentacoordinati (Ti_{5c}) e un debole carattere basico di bronstead dovuto ad atomi di ossigeno bicoornati (O_{2c}). In media, sono presenti 5 atomi/nm^2 di Ti_{5c} e O_{2c} sulla superficie, indipendentemente dal piano cristallino (Figura 3).

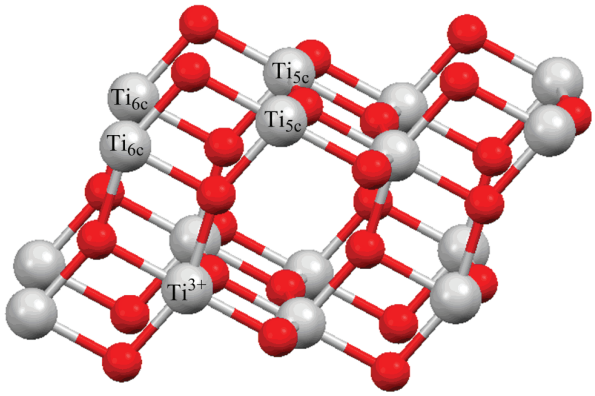

TiO_2 (101)

Ti_{5c} : 5/nm^2 Ti_{6c} : 5/nm^2 Ti^{3+} : 0.1/nm^2

Figura 3 Rappresentazione schematica dei pianicristallini (101), che mostra la presenza di siti acidi di Lewis (Ti_{5c}) e l'attività paramagnetica del (ioni Ti^{3+}).

Successivamente a questa caratterizzazione qualitativa e quantitativa delle specie presenti sulla superficie dell'anatase, la superficie di $TiO_{2(700)}$ è stata esposta ad un complesso organometalico di tantalio. Il grafting è stato effettuato utilizzando tecniche SOMC a temperatura ambiente e in pentano (Eq. 4). Il complesso di tantalo, $Ta[-CH_2C(CH_3)_3]_3[=CHC(CH_3)_3]$ (**1**), è stato utilizzato come precursore per il fatto che le specie risultanti dal greffaggio dello stesso su silice parzialmente deidrossilata a 700°C sono già state ampiamente descritte. Il greffaggio di (**1**) su $TiO_{2(700)}$ è stato monitorato tramite la quantificazione del neopentano rilasciato durante la reazione, che per altro è stato anche indice del successo della stessa. Una volta effettuato il grafting, il solido grigio-blu è stato studiato tramite spettroscopia DRIFT, NMR CPMAS al ^{13}C, EPR e EXAFS e tramite

analisi elementare, il prodotto è stato inoltre idrolizzato, utilizzando H_2O degassata per quantificare il neopentano residuo (Eq. 5).

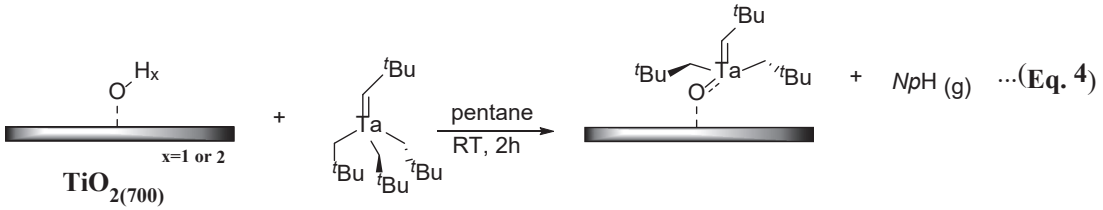

...(**Eq. 4**)

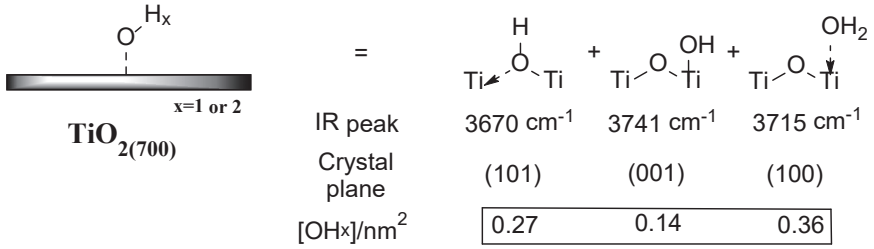

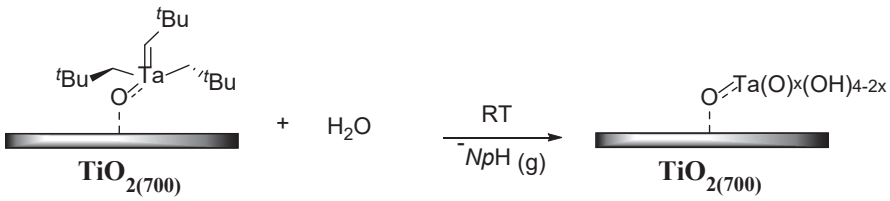

...(**Eq. 5**)

Gli spettri DRIFT del solido grigio-blu mostrano il consumo dei titanoli presenti sulla superficie, indice che la reazione tra il precursore metallico e la superficie è stata quantificata. Inoltre, l'analisi elementrare ha mostrato la presenza di 1 Ta/nm^2 e 14 C/Ta, dimostrando il fatto che la reazione sia andata a completamento e possibilmente la formazione di specie monopodali come nel caso della $SiO_{2(700)}$. Gli spettri EPR mostrano un incremento nell'attività paramagnetica del materiale se paragonato alla $TiO_{2(700)}$, richiamando il noto fenomeno di "self-doping" della TiO_2. Nel nostro caso possiamo proporre un meccanismo basato sulla natura ossofilica del legame tantalo-carbonio: questo può comportarsi in trappola per l'ossigeno, portando alla formale riduzione del Ti(IV) a "Ti(III)", così spiegando l'evoluzione dello spettro EPR osservato. Non è stato possibile ricavare alcuna informazione rilevante dal SSNMR del solido a causa della sua natura paramagnetica, che ha portato ad una perturbazione dei segnali. Per avallare questa ipotesi, saranno condotti uleriori test utilizzando la tecnica SOMC per il $Ta(OEt)_5$.

Le tecniche SOMC generalmente portano alla sintesi di catalizzatori che presentano siti attivi strutturalmente ben definiti su di una superficie substrato. Ma dal momento in cui la $TiO_{2(700)}$ stessa presenta una miscela complessa di differenti piani cristallini, costituiti da diversi tipi di idrossili, affiancati da centri acidi, Ti_{5c}, e paramagnetici, "Ti(III)", e un fenomeno paramagnetico di "self-doping", che aumenta il numero di sito "Ti(III)", è risultato difficile utilizzare le tecniche SOMC con il classico precursore di Ta(V). Per questo motivo, l'acidità di Lewis della superficie della $TiO_{2(700)}$ è stata sfruttata tramite la sua esposizione una molecola coordinante bifunzionale come il 2-metilimidazolo (**2-mIm**), per produrre una superficie omogenea che possegga siti utili al grafting, dopo la coordinazione con i siti acidi presenti sulla superficie.

La superficie della $TiO_{2(700)}$ è stata esaminata tramite spettroscopia DRIFT utilizzando la piridina come moleocola sonda iniziale. La piridina è stata adsorbita sulla $TiO_{2(700)}$ precedentemente agli esperimenti, e gli spettri DRIFT sono stati studiati durante il processo di desorbimento. A 20°C, è possibile osservare sei differenti picchi per la piridina adsorbita sulla $TiO_{2(700)}$ nella regione tra 1200 e 1700 cm^{-1}, che corrispondono ai modi di stiramento dell'anello C-C e C-N. La frequenza di picco e la larghezza dell'intenso assorbimento ν_{19b} che appare a 1445 cm^{-1} corrisponde al modo di stiramento C-N-C della piridina. La posizione dell'assorbimento ν_{19b} a 1445 cm^{-1} conferma che le molecole di piridina sono chemisorbite sui siti acidi di Lewis della TiO_2 anatase. La frequenza di questo modo è grandemente influenzata dall'interazione tra il doppietto isolato sull'azoto della molecola di piridina e la superficie subtrato. Nella regione di stretching ν(CCN), è possibile vedere una spalla a numeri d'onda minori sia per ν_{19a} (picco a 1492 cm^{-1}) che ν_{19b} (picco a 1445 cm^{-1}), indicando che c'è più di un tipo di siti acidi di Lewis sulla superficie della TiO_2. In seguito ad un costante incremento della temperatura è stato osservato un concomitante desorbimento della piridina, fino ad una quasi completa rimozione dell'N-eterociclo intorno a 350°C. Durante il processo di desorbimento, non sono comparsi nuovi picchi, indice del fatto che la piridina non si sia decomposta sulla superficie dell'anatase. Lo studio risulta essere coerente con la letteraatura riportata e conferma la presenza principalmente di siti acidi di Lewis. Dato che non è stato osservato nessun picco corrispondente a PyH^+ si può concludere che sulla superficie dell'ossido è predominante una chimica acida di Lewis.

Uno studio simile è stato anche condotto per la molecola target 2-mIm per studiare la sua interazione con la superficie di $TiO_{2(700)}$. Il desorbimento assistito da temperatura di 2-mIm

dalla $TiO_{2(700)}$ ha mostrato che la molecola si coordina ai siti acidi di Lewis presenti sulla superficie con un impacchettamento di tipo multilayer. La banda di stretching ν_{N-H} a 3505 cm^{-1} mostra un'intensità massima a circa 200°C indicando la natura isolata del pirrolo. Quindi, a scopo preparativo, successivamente all'adsorbimento del 2-mIm a 120°C sulla $TiO_{2(700)}$, è stato eseguito un desorbimento a 200°C sotto condizioni di UHV per ottenere una coordinazione netta di 3.5 2-mIm/nm^2 come riscontrato da analisi elementare. Lo spettro CPMAS NMR al ^{13}C del solido risultante mostra tutti i picchi relativi ai C del 2-mIm confermando ulteriormene il fatto che la coordinazione del linker sulla superficie abbia funzionato. Questo primo monolayer è inteso come interfase per effettuare un'uleriore chimica SOMC con precursori organometallici.

Infine, è stato sviluppato un nuovo supporto strutturato a base di anatasio che si può facilemente applicare a celle fotoelettrocatalitiche (PEC) basato su nanotubi di TiO_2 su griglia di Ti. Nanotubi di TiO_2 (**TNTs**) su di una griglia di Ti sono noti per avere un'efficienza fotocatalitica superiore alle polveri di TiO_2. Questo è dovuto i) al maggiore assorbimento della luce dato dall'ordine del sistema, ii) ad una facile diffusione degli elettroni da anodo a catodo dato che i nanotubi sono supportati su Ti metallico e iii) ad una maggiore area superficiale in un setup compatto.[23-27] I nanotubi di TiO_2 sono stati fabbricati su una griglia di Ti dato che offre un'alta area superficiale specifica, una struttura 3-D meso/macro porosa, una certa flessibilità e bassa dipendenza dall'angolo di incidenza della luce. Per sintetizzare i TNT su griglia di Ti è stata utilizzata una tecnica di ossidazione anodica elettrochimica. Questo metodo forma una di TNT ben definiti e allineati perpendicolarmente che originano dalla superficie substrato (mesh di Ti) e che sono quindi connessi elettricamente e facili da maneggiare. L'anodizzazione è stata effettuata in una cella elettrochimica con un elettrodo in Pt come catodo e la mesh di Ti come anodo. Sono stati testati differenti potenziali e tempi di reazione per ottenere TNT con differenti paramentri stutturali. Una volta anodizzata, la griglia con TNT amorfi è stata calcinata a 450°C sotto aria per formare TNT cristallini. La struttura risultante mostra due tipi di porosità: i) una mesoporosità dovuta ai nanotubi di TiO_2, i quali hanno un diametro interno tra 40 e 120 nm (come risulta dalle caratterizzazioni SEM), ii) una macroporosità data dalla struttura delle griglie di Ti (80 mesh). Per tutti i campioni, una volta cristallizzati tramite calcinazione, è stato possibile analizzare tramite XRD la presenza della sola fase anatase. Gli spettri UV-vis per le TNT-mesh di Ti anodizzati per un'ora a 50V mostrano

un ampio spettro di assorbimento centrato a circa 580-600 nm, oltre all'assorbimento caratteristico nella regione UV. Questo è dovuto ai fenomeni di diffrazione e scattering.

Misure cronoamperometriche per le TNT su griglia di Ti anodizzati a 50V sono state effettuate tra 20-420 minuti sotto diversi filtri. I netti aumenti e diminuzioni di corrente con luce ON/OFF sono dovuti all'assorbimento ottico e alla formazione di coppie vacanza-elettrone che sono indicativi della attività fotoelettrochimica dei TNT. Il valore più alto di fotocorrente è stato ottenuto per il campione anodizzato per 20 minuti (0.53 mA cm^{-2}). Per il filtro AM 1.5, che simula la luce solare che raggiunge la superficie terrestre, il campione anodizzato per 5 ore mostra una densità di fotocorrente elettrica superiore agli altri.

Per valutare stabilità ed efficienza del catalizzatore, test di fotocatalisi sono stai effettuati per tutti i campioni TNT- griglia Ti anodizzati a 50V tra 20-420 minuti in una cella fotoelettrocatalitica (PEC). I TNT-mesh di Ti sono stati assemblati con Nafion® e GDL e testati in apparecchi PEC. Quando la sorgente luminosa viene accesa, O_2 viene prodotto nella camera anodica mentre la camera catodica produce H_2. Tutti i fotocatalizzatori sono stati testati per un periodo di 5 ore durante il quale hanno mostrato un'ossidazione dell'acqua costante e stabile (mediata dalla produzione di H_2). L'attività maggiore in termine di fotosplitting dell'acqua è stato mostrato dalla TNT- griglia Ti anodizzata per 5 ore a 50V. Un massimo nella velocità di produzione di H_2 di 0.59 μmol/min è stato ottenuto, dando circa 177 μmol in 5 ore di irradiazione luminosa, mentre l'efficienza di fotoconversione è stata più elevata per il campione anodizzato per 20 minuti. Questi risultati sono migliori dello stato dell'arte nella fotoproduzione di H_2 tramite TNT su mesh di Ti.

Per concludere, abbiamo caratterizzato dal punto di vista SOMC la superficie di una polvere di titania anatasio parzialmente deidrossilata. I risultati mostrano la presenza di tre tipi di idrossili sulla superficie (un titanolo a ponte (preferenzialmente su di un piano cristallino (101)), un titanolo terminale (preferenzialmente su un piano cristallino (001)) e una molecola d'acqua coordinata (preferenzialmente su un piano cristallino (100)) in rapporto relativo 1.0:0.5:1.3 per un totale di 0.7 OH/nm^2 sui diversi piani cristallini dell'anatasio) insieme a centri di "Ti(III)" (0.1 Ti^{3+}/nm^2) e atomi di titanio pentacoordinati siti acidi di Lewis (ca. 5 Ti_{5c}/nm^2) e basici di Bronsted (O_{2c}). Il complesso organometallico di Ta è stato greffato sulla polvere precedentemente trattata di $TiO_{2(700)}$, utilizzando tecniche SOMC. La reazione è stata analizzata tramite DRIFT, EPR e analisi elementare,

dimostrando l'incremento dei siti "Ti(III)". La molecola 2-mIm è stata coordinata con successo ai siti acidi di Lewis della $TiO_{2(700)}$ come dimostrato da caratterizzazioni DRIFT, SSNMR e analisi elementare, lasciando un NH accessibile, disponibile come sito per una successiva reazione di superficie.

Infine, un fotocatalizzatore TNT/ griglia di Ti con ordine mesoporoso/macroporoso è stato sviluppato come possibile supporto per esplorare le tecniche SOMC su ossidi autoportanti (quindi non sotto forma di polveri). I TNT/ griglia di Ti risultanti mostrano una serie ordinata di nanotubi di TiO_2 verticalmente allineati, che originano dalla griglia di Ti. Il campione anodizzato per 5 ore a 50V è risultato essere il catalizzatore più performante in confronto agli altri campioni in termini di velocità di produzione di H_2, ed ha presentato un'attività stabile e costante durante un test di 5 ore in apparecchiatura PEC.

Con l'aumentare delle emissioni di carbonio, risulta essere imminente la necessità di uno sviluppo e implementazione di una chimica mossa dal solare che possa aiutare a ridurre l'mpronta carbonio dei processi. Questo lavoro è un primo passo verso la comprensione dello sviluppo di fotocatalizzatori strutturalmente ben definiti tramite un approccio SOMC, che possa portare a catalizzatori che combinino fotocatalisi e chimica eterogenea su atomi metallici isolati su di una superficie.

References

(1) Wernicke, H.-J.; Fischer, R. W. *Chemie Ing. Tech.* **2006**, *78* (7), 825–834.

(2) Somorjai, G. A.; McCrea, K. *Appl. Catal. A Gen.* **2001**, *222* (1–2), 3–18.

(3) Zakharov, V. A.; Yermakov, Y. I. *Catal. Rev.* **1979**, *19* (1), 67–103.

(4) Copéret, C.; Chabanas, M.; Petroff Saint-Arroman, R.; Basset, J.-M. *Angew. Chemie Int. Ed.* **2003**, *42* (2), 156–181.

(5) *Modern Surface Organometallic Chemistry*; Basset, J.-M., Psaro, R., Roberto, D., Ugo, R., Eds.; Wiley-VCH Verlag GmbH & Co. KGaA: Weinheim, Germany, **2009**.

(6) Copéret, C.; Comas-Vives, A.; Conley, M. P.; Estes, D. P.; Fedorov, A.; Mougel, V.; Nagae, H.; Núnez-Zarur, F.; Zhizhko, P. A. *Chem. Rev.* **2016**, *116* (2), 323–421.

(7) Aristov. B, Kiselev, A. *Zh. Fiz. Khim.* **1964**, *38* (8), 1984–1989.

(8) Millot, N.; Santini, C. C.; Lefebvre, F.; Basset, J.-M. *Comptes Rendus Chim.* **2004**, *7* (8–9), 725–736.

(9) Bartram, M. E.; Michalske, T. A.; Rogers, J. W. *J. Phys. Chem* **1991**, *95*, 4453–4463.

(10) and, G. P.; Reynders*, P. **1999**.

(11) Braun, J. H.; Baidins, A.; Marganski, R. E. *Prog. Org. Coatings* **1992**, *20* (2), 105–138.

(12) Fujishima, a; Honda, K. *Nature* **1972**, *238* (5358), 37–38.

(13) Inoue, Tooru; Fujishima, Akira; Konishi, Satoshi; Kenichi, H. *Nature* **1979**, *277*, 637–638.

(14) Di Paola, A.; Bellardita, M.; Palmisano, L. *Catalysts* **2013**, *3* (1), 36–73.

(15) Mills, A.; Le Hunte, S. *J. Photochem. Photobiol. A Chem.* **1997**, *108* (1), 1–35.

(16) Zhuang, H.; Zhang, Y.; Chu, Z.; Long, J.; An, X.; Zhang, H.; Lin, H.; Zhang, Z.; Wang, X. *Phys. Chem. Chem. Phys. Phys. Chem. Chem. Phys* **2016**, *9636* (18), 9636–9644.

(17) Li, X.; Zhuang, Z.; Li, W.; Pan, H. *Appl. Catal. A Gen.* **2012**, *429–430*, 31–38.

(18) Dvoranová, D.; Brezová, V.; Mazúr, M.; Malati, M. A. *Appl. Catal. B Environ.* **2002**, *37* (2), 91–105.

(19) Transactions, E. C. S.; Society, T. E. **2008**, *3* (43), 1–9.

(20) Yang, L.; Li, Z.; Jiang, H.; Jiang, W.; Su, R.; Luo, S.; Luo, Y. *Appl. Catal. B Environ.* **2016**, *183*, 75–85.

(21) Hamadanian, M.; Karimzadeh, S.; Jabbari, V.; Villagrán, D. *Mater. Sci. Semicond. Process.* **2016**, *41* (JANUARY), 168–176.

(22) Tahir, M.; Amin, N. S. *Energy Convers. Manag.* **2013**, *76*, 194–214.

(23) Roy, P.; Berger, S.; Schmuki, P. *Angew. Chemie - Int. Ed.* **2011**, *50* (13), 2904–2939.

(24) Kontos, A. I.; Likodimos, V.; Stergiopoulos, T.; Tsoukleris, D. S.; Falaras, P.; Rabias, I.; Papavassiliou, G.; Kim, D.; Kunze, J.; Schmuki, P. *Chem. Mater.* **2009**, *21* (4), 662–672.

(25) Nguyen, N. T.; Ozkan, S.; Hwang, I.; Mazare, A.; Schmuki, P. *Nanoscale* **2016**, *8*.

(26) Passalacqua, R.; Ampelli, C.; Perathoner, S.; Centi, G. *Nanosci. Nanotechnol. Lett.* **2012**, *4* (2), 142–148.

(27) Mor, G. K.; Varghese, O. K.; Paulose, M.; Shankar, K.; Grimes, C. A. *Sol. Energy Mater. Sol. Cells* **2006**, *90* (14), 2011–2075.

Table of Content

Chapter 5: 3D-type meso/macro porous structured photoanodes based on Ti mesh

Chapter 1

Introduction to SOMC & TiO_2

Chapter 1
Introduction to SOMC & TiO_2

Part I: SOMC on silica

Part II: TiO_2-A photoactive support

Part III: Goal of the thesis

Chapter 1

Part I: SOMC on silica

1.1 Surface organometallic chemistry (SOMC)

In the 20th century, chemical industries have changed our lives by shaping our modern technological society *via* supplying us with energy, medicines, crop protection, foodstuffs, and new materials worldwide. Introduction of catalysis is one of the key factors responsible for evolution of such an industry driven society. Catalysts have been successfully used in the industry for more than 100 years. More than 90% of industrial processes has at least one catalytic step in its process of delivering the end product.[1,2] This catalytic step may proceed *via* either homogeneous catalysis or heterogeneous catalysis (enzymes being currently the "assuage" of nature, this being currently changing)[2].

A homogeneous catalyst is by definition in the same phase as the reactant and product. It is usually a well-defined molecular compound soluble in the reactant phase. Homogeneous catalysts offer capacity to draw from a formidable library of ligands to tailor the reactivity around the metal, the case of the metal based catalytic synthesis. While the presence of single active sites make homogeneous catalysts an attractive option, the limited thermal excursion allowed by solvent and/or by the ligand ensemble of the catalyst itself and the difficulty in separation process from the reaction mixture can in part explain the limited examples of homogeneous catalytic systems (Ziegler-Natta catalyst[3], Wackers process[4], Cativa process[5]…).

On the other hand, heterogeneous catalysts have an outstanding industrial track record in part explained by the scalability of the system with respect to homogeneous (solution) system, easement in separation of catalysts from reaction products, their

highly thermal stability, applicability to continuous flow processes, manageable costs and their recyclability.[6–8] Heterogeneous catalysts are prepared by a variety of methods such as wetness impregnation, sol gel method, mechanical mixing, wet kneading, co-precipitation etc.[9,10] One problem which can be associated with these methods is the creation of multiple surface species which can drop activity with respect to the ideal "single site" catalyst.[11]

In a strive to combine the advantages of homogeneous and heterogeneous catalysis a new powerful approach was developed around the 1960's known as Surface Organometallic Chemistry (**SOMC**).[12–25] In the early 1960's, emerged the idea that heterogeneous catalysts could be described as a collection of molecularly well-defined reactive sites. This allowed to apply the concept of (homogeneous) molecular catalytic systems to heterogeneous catalysis.[26,27]

Surface Organometallic Chemistry or SOMC is a method that allows to react organometallic complexes with surface sites of a support in a controlled fashion to obtain well-defined catalysts.[28] In systems such as oxides, where the effective surface can be expected to display surface hydroxyls, this approach controls the concentration of the grafted complex as a function of the OH density of the surface (Figure 1.1). The principal advantage of SOMC lies in its capability to produce surface sites with a known coordination sphere, thus assisting structure–activity relationship and rational design of heterogeneous catalysts. The starting requirements to apply an SOMC approach would be the presence of a well-characterized support in terms of nature and concentration of surface reactive moieties and an organometallic complex of ML_nX_x (L= functional ligand, X= Ancillary ligand) type which reacts in a well-defined way with the surface species.[29]

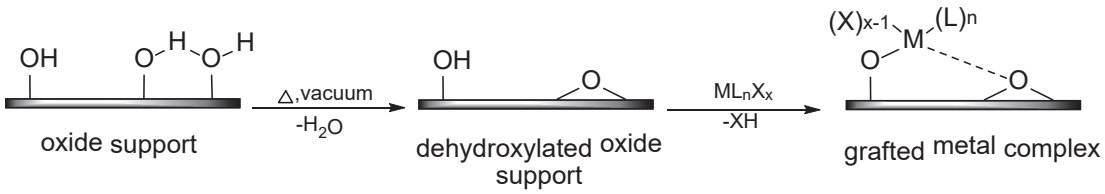

Figure 1.1 Schematic representation of preparation of a well-defined catalyst using SOMC on a solid oxide whose ultimate surface can be correctly described by a collection of surface hydroxyls.

Once the organomettalic complex is grafted on the support it can be used as a catalyst by itself or can be thermally treated in presence of a reactive (or inert) gas or vacuum to obtain isolated surface species.[30–33]

Well-defined catalysts developed by SOMC mainly comprises of four different components: i) the support, ii) the metal, iii) the functional ligand and iv) the ancillary ligand. A huge variety of these different components are used to prepare complexes as shown in Figure 1.2. Each component can play a specific role in the overall catalytic

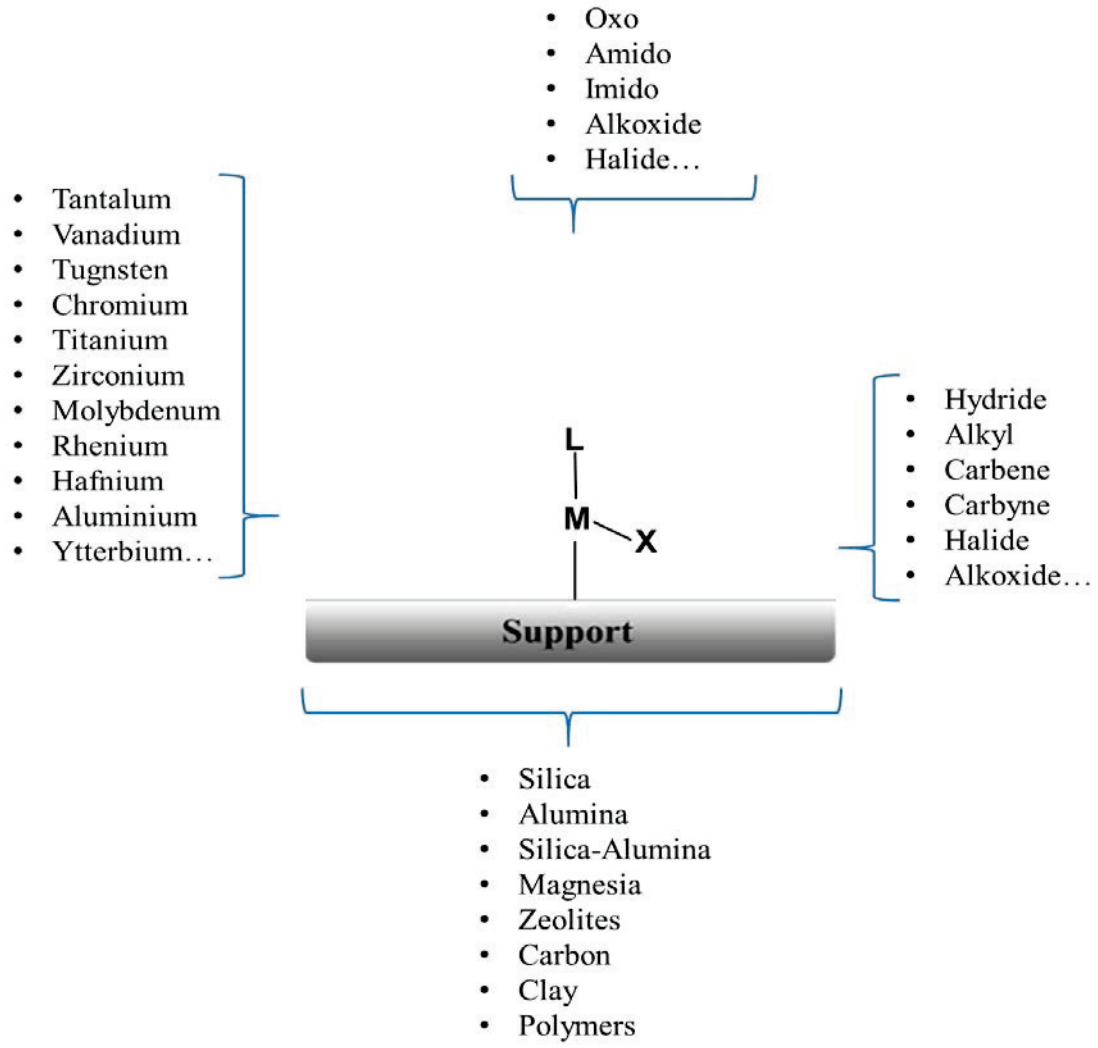

Figure 1.2 The generic structure of surface organometallic compounds and the possibility of bearing different possible supports, transition metals, functional and spectator ligands (only monopodal species is shown for simplicity, likewise, possible ancillary assistance from neighbouring surface moieties is omitted too).

cycle, such as in molecular catalysis.[34] The coordination sphere of the grafted complex on the surface of the support are usually characterized by means of advanced techniques such as SSNMR and EXAFS.[35–37]

1.2 The Support

Organometallic complexes can be grafted on various supports such as silica[38], alumina[39–41], silica-alumina[42,43], zeolites[44] etc. The essence of the support belongs to the sort of grafting site it carries. Different supports have different grafting sites as shown in Table 1.1. Depending on the nature, density and homogeneity of the reactive sites on the surface of these materials, different behaviors can be observed, leading to completely different catalytic applications.[8]

Table 1.1 Grafting sites present in some supports used for SOMC[8,28]

Support	*Grafting site*
Silica	Hydroxyl groups called silanols (≡Si-O-(H))
Silica-Alumina	Silanol groups; Si–O(H)–Al bridges
Alumina	Hydroxyl groups (at least five different types); Al–O–Al bridges (where the bond is not covalent); Lewis acid sites
Magnesia	Hydroxyl groups; lacunar magnesium sites
Zeolites	Protons with different locations which can be more or less accessible; extra-framework aluminium sites; silanol groups on the external surface of the crystallites
Carbon	All chemical functions can be found: alcohols, amines, ethers, thiols, ketones, aldehydes, carboxylic acid, etc

Silica an amorphous material, is one of the most well-established support for performing SOMC, consisting of SiO_4 tetrahedra linked by siloxane (≡Si-O-Si≡) bridges and surface silanols (≡Si-OH). Depending on the surface area, silica can be found in different types such as silica gel, flame silica, porous and mesoporous silica (MCM-41[45] and SBA-15[46]). Silanols found on the surface of silica are hydrophilic in nature and can be used for covalent grafting of organometallic complexes. Heating under dynamic vacuum at *ca.* 150°C, all physisorbed water molecules are desorbed (Figure 1.3).

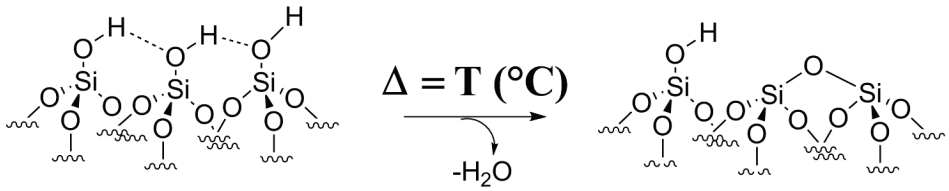

Figure 1.3 Scheme describing elimination of physisorbed water from the surface of amorphous silica which leads to formation of different types of silanols and siloxane bridges (≡Si-O-Si≡)

Heating at higher temperature leads to condensation between adjacent hydroxyl groups, resulting into formation and evolution of water molecules and formation of ≡Si–O–Si≡ bridges. In the year 2000, Zhuravlev[47] constructed a model as a function of temperature, determining the nature and quantity of silanols per unit surface. As

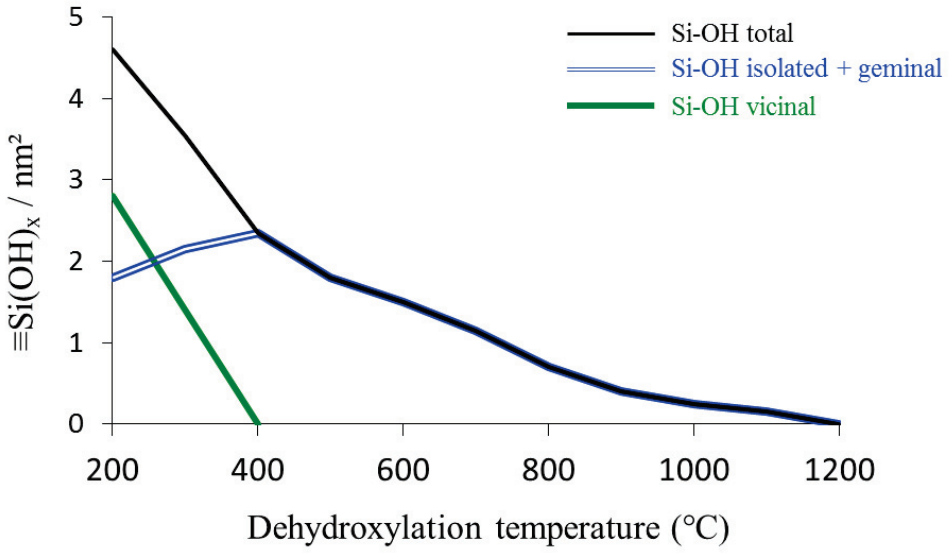

Figure 1.4 Evolution of the quantity and nature of the silanols present on the surface of silica between 200°C and 1200°C, adapted from Zhuravlev.

shown in Figure 1.4, an increase in the temperature causes dehydroxylation of surface silanols thereby decreasing the overall density of silanols (-OH/nm^2). As the temperature increases, the dehydroxylation leads to generation of siloxane bridges by diminishing the proportion of geminal and vicinal silanols. This process of formation of siloxane bridges eventually creates isolated silanols. Dehydroxylation at 200°C (**$SiO_{2-(200)}$**) yields a surface primarily consisting of vicinal hydroxyl pairs as shown in Figure 1.5. Further heating at 500°C (**$SiO_{2-(500)}$**), gives isolated silanols while dehydroxylation at 700°C (**$SiO_{2-(700)}$**) prepares isolated hydroxyls that are reasonably

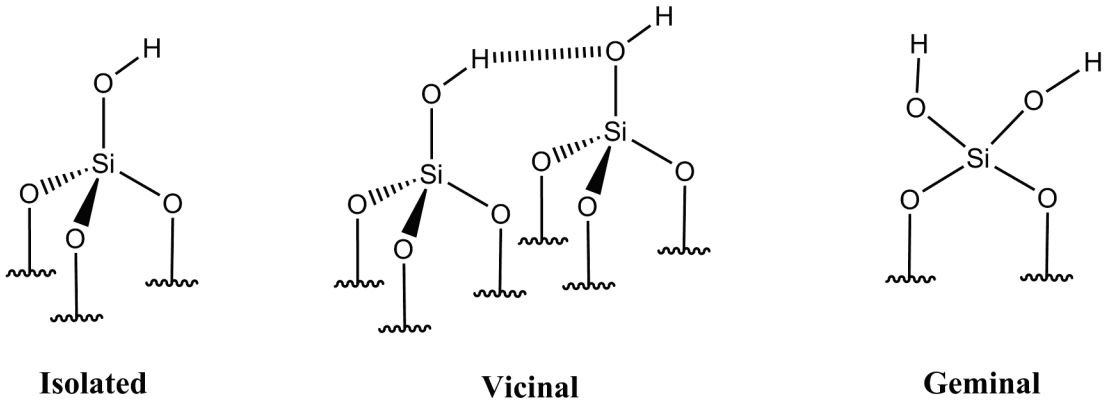

Figure 1.5 Different hydroxyl groups present on the surface of silica.

considered so far away that well-defined grafted organometallic isolated species will be expected upon reaction with these hydroxyl groups.

Infrared spectroscopy is useful to characterize the surface silanols. Infrared spectrum of silica desorbed at 150°C shows mainly in the ν_{OH} domain, a very broad band between 3700 cm^{-1} and 3500 cm^{-1} attributed to ≡Si–OH groups linked via hydrogen bonds.[48] The intensity of the broad infrared band decreases as the temperature increases and a sharp band at *ca.* 3750 cm^{-1} appears for ($SiO_{2-(700)}$) which corresponds to isolated silanols.[49,50]

The concentration of hydroxyl groups on $SiO_{2-(200)}$, $SiO_{2-(500)}$ and $SiO_{2-(700)}$ can be determined by chemical titration methods which involves reaction of accessible hydroxyls with metal alkyls (*n-Bu*Li) or metal alkyl halides (MeMgBr). The chemical titration of surface silanols is a core step in SOMC as it provides a quantitative order of approximation of accessible hydroxyls (mechanistic aspect in Chapter 3). Using this technique, an OH density of *ca.* 2.6, 1.4 and 0.7 OH/nm^2 has been reported for $SiO_{2-(200)}$, $SiO_{2-(500)}$ and $SiO_{2-(700)}$ and has been verified using quantitative solid-state ^{1}H MAS NMR.[35,51]

Therefore, we can conclude that even the simplest support silica; doesn't consist of a single species on its surface. For other oxides such as alumina the situation is more complex and more than five different types of hydroxyl groups can be identified without taking into account the Lewis acid sites. For this reason, most of the studies in literature are reported on silica dehydroxylated at high temperatures.

1.3 Organometallic complexes

Combination of different metals, functional and ancillary ligands forms organometallic complexes. While the ligands control the reactivity of the grafted metal, the character

of the overall catalyst depends on the size of the central metal atom, its oxidation state, coordination sphere etc.[52] Homoleptic and heteroleptic transition metal complexes are mainly used in the preparation of SOMC based catalysts.

1.4 Grafting an organometallic complex

Grafting a metal precursor onto oxide supports requires strict anhydrous and anaerobic conditions. This is because metal complexes are generally sensitive to air and water in solution, presence of water can affect the dehydroxylated oxide support *via* physisorption and the increased sensitivity of surface grafted species supported on high surface area oxides.

Generally, an organometallic precursor with an M^1—X configuration is chosen for which the reaction $\mathbf{M^1—X + M—OH \rightarrow M—O—M^1 + HX}$ is favoured thermodynamically, with M—OH being the hydroxyl group of the support. Homoleptic complexes usually leads to formation of a single complex on the surface site thereby producing single site well-defined moieties on the entire support.[8] On the contrary, heteroleptic organometallic complexes such as alkoxides or chloride derivatives; the by-products of the reaction (HCl or alcohols) can react with the surface hydroxyls or M—O—M resulting in modification of surface properties. Structural information of the resultant complex can be determined using solid-state NMR, gas quantification methods as well as elemental analysis. An example to better understand the features of this technique has been discussed below.

1.5 Application of SOMC based catalysts

SOMC has been able to prepare well-defined catalysts for numerous catalytic applications such as alkane metathesis (silica-supported tantalum hydride)[53], olefin metathesis ($[(\equiv SiO)W(\equiv C\ t\text{-}Bu)(OCH_2t\text{-}Bu)_3]$)[54,55], alkene polymerization ($[(\equiv SiO)ZrCp^*Me][MeB(C_6F_5)_3]$)[56], N_2 to NH_3 transformation[57], ethylene to propylene conversion, oxo/imido heterometathesis etc.[28] Most of these conversion processes are petrochemical transformation (some being biomass conversion). But the capacity to perform this chemistry on photoactive supports would consent the use of solar fuels (as feedstocks) and could therefore constitute the solar driven chemistry.

Part II: TiO_2-A photoactive support

1.6 Photoactive support for solar driven chemistry

The ongoing trends in CO_2 emissions justified an immediate need for restraining the carbon footprint to move towards a carbon-sober future.[58,59] Among the routes explored, the direct use of renewable energy sources and in particular solar energy, to drive chemical transformations is actively researched both to generate the so called "solar fuels" and also to drive chemical feedstock transformation to materials and bulk chemicals (not limited therefore to fuel use).[60]

1.7 Titania- A photoactive catalyst

Titanium dioxide or TiO_2, a white solid, has been widely used since its commercial production in the early 20th century as a pigment[61] and in sunscreens[62,63], paints[64], ointments, toothpaste[65], self-cleaning glasses etc. After the ground-breaking discovery of photocatalytic water splitting on a TiO_2 electrode by Fujishima and Honda in 1972[66], enormous efforts have been devoted to the research of TiO_2 material, which has led to many promising applications in areas ranging from photovoltaics and photocatalysis to photo-electrochromics and sensors.[67–70] Between 1977 and 1979, initial attempts of photocatalytic N_2 reduction and photoelectrocatalytic CO_2 reduction were performed with successful results.[71,72] Most of these applications are mainly divided into "energy" and "environmental" categories, thus making TiO_2 an interesting material for research and industrial sectors. These applications depended not only on the properties of the TiO_2 material itself but also on the modifications of the TiO_2 material host (e.g., with inorganic and organic dyes, metal doping etc.) and on the interactions of TiO_2 materials with the environment.[73,74] In particular, TiO_2 nanomaterials unlike the bulk behaves differently in terms of the movement of electrons and holes in semiconductor nanomaterials and the transport properties related to phonons and photons.[75–78] The high surface area brought about by small particle size is beneficial to many TiO_2-based devices, as it facilitates reaction/interaction between the devices and the interacting media, which mainly occurs on the surface or at the interface and strongly depends on the surface area of the material. Thus, the performance of TiO_2-based devices is largely influenced by the sizes of the TiO_2 building units at the nanometer scale.

Titania materials in diverse types and forms have shown pronounced potential as an ideal and influential photocatalyst for various significant reactions due to its chemical stability, nontoxicity, and high reactivity.[79] TiO_2 primarily exists in three different crystalline phases, namely: i) Anatase, ii) Rutile and iii) Brookite. The atoms are packed in a tetragonal geometry for anatase and rutile while an orthorhmic packing is followed by brookite (Figure 1.6).[80] In all the polymorphs, titanium cations are six fold

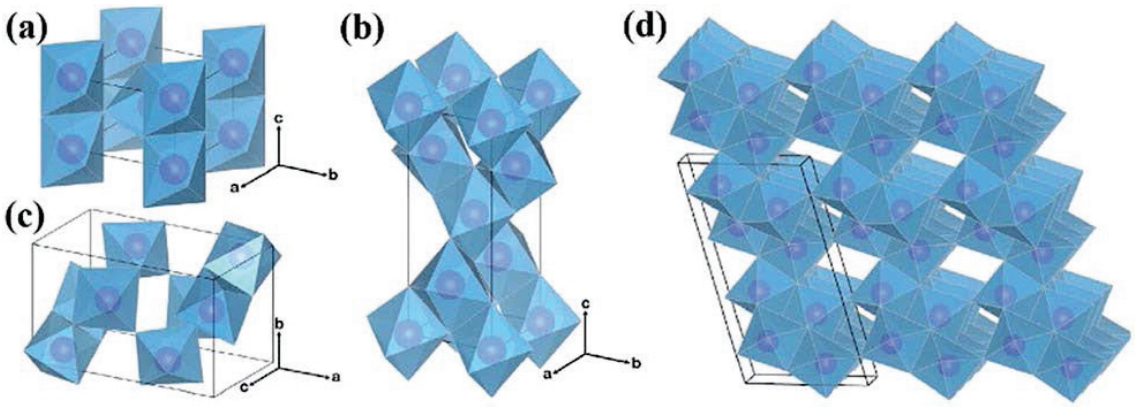

Figure 1.6 Crystal structures of TiO_2 polymorphs: (a) rutile, (b) anatase, (c) brookite and (d) and TiO_2(Bulk). Purple spheres represent Ti atoms, and the blue octahedra represent TiO_6 blocks. Oxygen atoms at the corner of the octahedra are omitted for clarity.[81]

coordinated to oxygen anions, forming distorted TiO_6 octahedra.[81] Amongst these, anatase and rutile are the most used supports due to their band gap positions as well as difficulty in synthesizing brookite in pure phase.[82–85] For bulk TiO_2, band gaps of anatase and rutile as shown in Figure 1.7 tells us that rutile phase can absorb more extensive range of light and should theoretically, show more photoactivity but this is not the case. This is related to several factors such as i) band gap positions of anatase and rutile[86], ii) lower absorption capability of rutile in the near UV region[87,88] and iii) lower mobility of photogenerated carriers[89,90].

Therefore, to obtain higher photocatalytic activity it is important to go for pure anatase TiO_2 without having any rutile phase.

Many studies have indicated that anatase TiO_2 with a higher crystallinity, smaller particle size, and larger surface area is favorable for photocatalysis.[86,91–93] But even at nanometer scale anatase TiO_2 suffers from disabilities such as poor absorption of

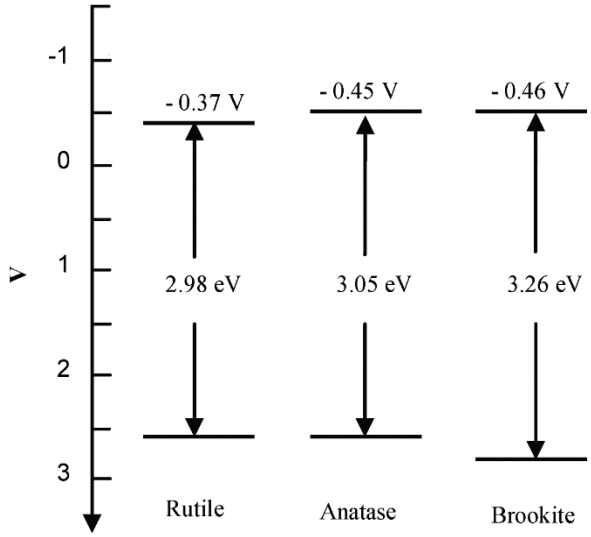

Figure 1.7 Electrochemical potentials of the band edges of anatase, brookite, and rutile at pH = 7.[82]

visible light, rapid electron-hole recombination and lower surfac area.[79,94–96] Numerous attempts have been made to overcome these limitations of the polymorph by modifying the structure of titania[97–99], doping different metals and non-metals[73,100–104], adding sacrificial layers such as dyes and sensitizing it with novel enzymes and polymers[105,106]. Few examples of this series of dopants and sensitizers that have been used so far is shown in Figure 1.8.

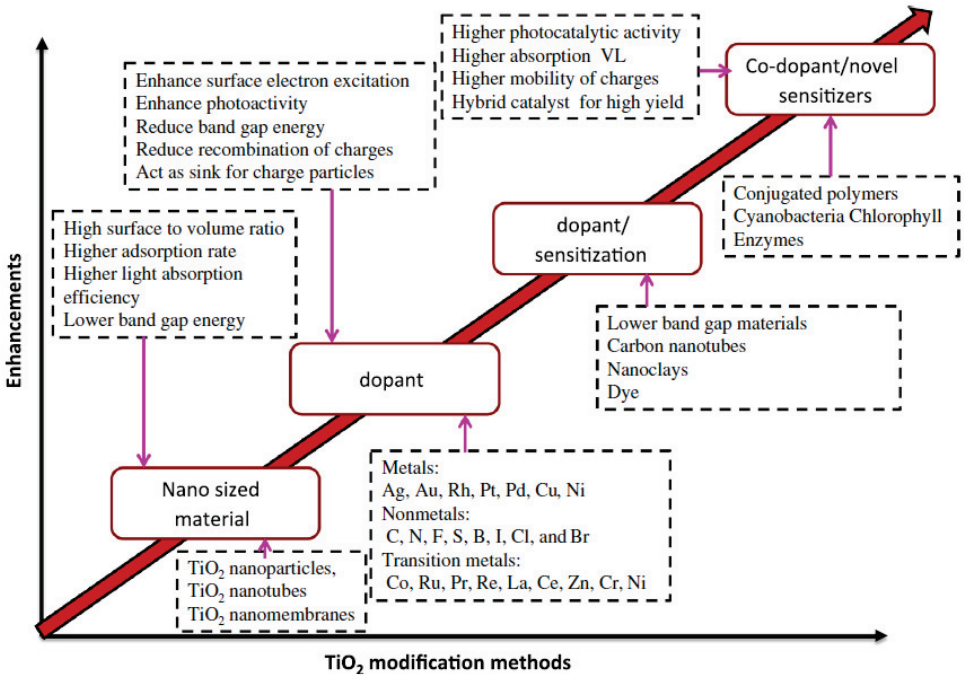

Figure 1.8 Schematic presentation of different modification techniques with their enhancement effects.[116]

The entire research scenario in TiO_2 photocatalysis is based on two strong pillars: i) Development of titania photocatalysts that can harvest solar photons for visible light catalysis and ii) controlled synthesis of photocatalytic materials with unique nanostructure processes of heterogeneous photocatalysis is so laggard that the current development of photocatalysts is losing its direction. Furthermore, most of the aforementioned modifications are unable to control the bonding between the dopant and TiO_2's surface and morphology.

Although elementary, advances in understanding the fundamentals leading to a heterogeneous catalyst with variable active sites causing a depletion in the overall activity of the catalyst. Therefore, there is potential interest in combining the photoactivity of TiO_2 with the unique properties of SOMC grafting to obtain well-defined photocatalysts.

1.8 Surface organometallic chemistry on Titania

Several attempts has been made by different research groups to perform SOMC using different organometallic precursors on TiO_2 (Figure 1.9).[28,107–109] In 1985, tris allyl Rhodium complex was grafted on titania pretreated at 200°C for ethene hydrogenation and ethane hydrogenolysis by Iwasawa *et. al.*[110] Later in 1992, Dufour *et. al.*[40] reported

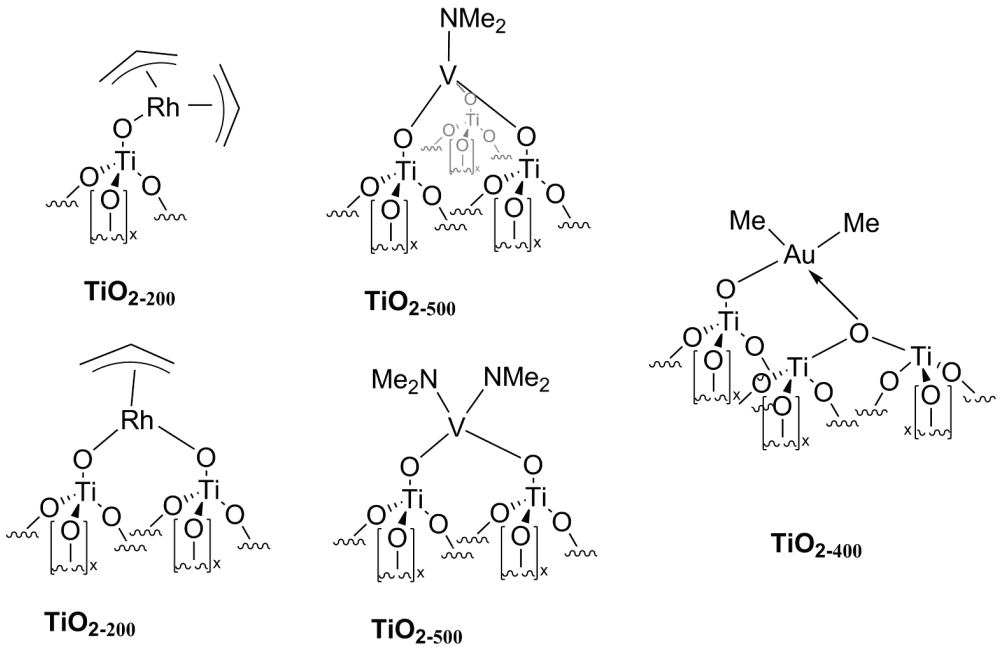

Figure 1.9 Proposed chemical structures of grafted organometallic species on titania's surface ($TiO_{2\text{-}T}$, where T is the dihydroxylation temperature in °C) after reaction with with $Rh(allyl)_3$, $V(NMe_2)_4$ and $AuMe_2(acac)$ (allyl = C_3H_5, acac = $CH_3COCH_2COCH_3$).

similar chemistry with TiO_2 P25 Degussa pretrated at 200°C under vacuum and characterized the surface species by infrared spectroscopy.

Guzman *et. al.*[108] used $Au(III)(CH_3)_2(C_5H_7O_2)$ as a grafting complex on TiO_2 P25 Degussa treated at 400°C under vacuum for CO oxidation. XANES and EXAFS data demonstated the formation of mononuclear Au(III) specie bonded to two O atoms. EPR sepctroscopic studies were performed by Grasser *et. al.*[111] as a model study to understand the coordination environment of V(IV) complex grafted on titania. Metallocenes such as Nickelocene and Ruthenocene have been used as organometallic precursors to obtain well-defined catalysts (Figure 1.10) for visible light water splitting and CO_2 reduction reactions respectively.[112,113] XANES and EXAFS were used to

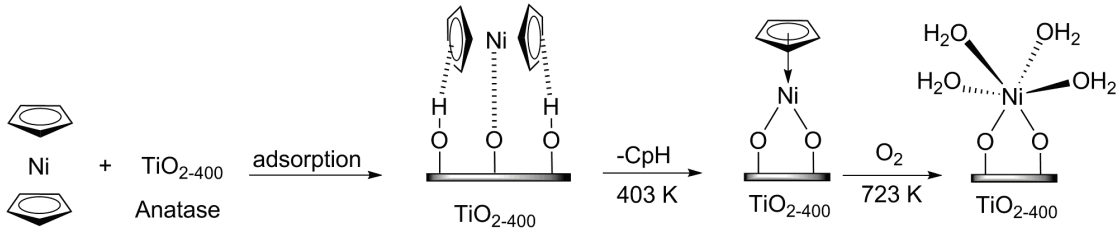

Figure 1.10 Schematic representation of grafting reaction between nickelocene and TiO_2 anatase (dehydroxylated at 400°C) and proposed structure of single-dispersed mononuclear nickel-oxo active species.

characterize the grafted species where as IR spectroscopy was used to monitor the grafting process. These systems work on the physical mechanism of metal to metal charge transfer (MMCT) wherein visible light harvested green electrons are generated on the grafted metal and then transferred to the bulk of TiO_2. This phenomena is due to the weak absorption of anatase in visible region of the spectrum. MMCT is an unique mechanism that also helps in charge separation and delays electron-hole recombination due to the diffusion process. When water photooxidation was performed between catalysts obtained by wetness impregnated Ni and SOMC grafted Ni it showed that the latter was twice as efficient as the former. The surface species formed in case of Ru grafting was proposed to be CpRuH-O-Ti ($Cp=\eta\text{-}C_5H_5$) which showed an excellent quantum efficiency of 0.56% for CO_2 to CH_4 conversion. An artificial donor–catalyst–acceptor triad photosystem where TiO_2 and C_5H_5-RuH served as an electron collector and CO_2 reduction site and the light absorption and water-oxidation site, respectively. This hybrid system formed a long lived electron-hole charge separation state to

perform CO_2 to CH_4 conversion. Other organometallic complex such as $(CH_3)_4$—Sn[114] was grafted on TiO_2 anatase pre-treated at 673K as in the above two examples. When performed photocatalytic water splitting, SOMC grafting proved more efficient than the corresponding wetness impregnated catalyst proving the need and prominence of a well-defined catalyst.

Bimetallic supported catalytic systems composed of Sn, Ru/TiO_2 and Ni, Sn/TiO_2 has also been developed using SOMC.[107,109] These bimetallic systems display improved photocatalytic reforming and water splitting efficiencies then their individual metal counter parts (Rh/TiO_2, Ni/TiO_2, Sn/TiO_2). This is because of further diffusion of the photo-generated electron by MMCT mechanism and therefore increasing the recombination time period as shown in Figure 1.11.

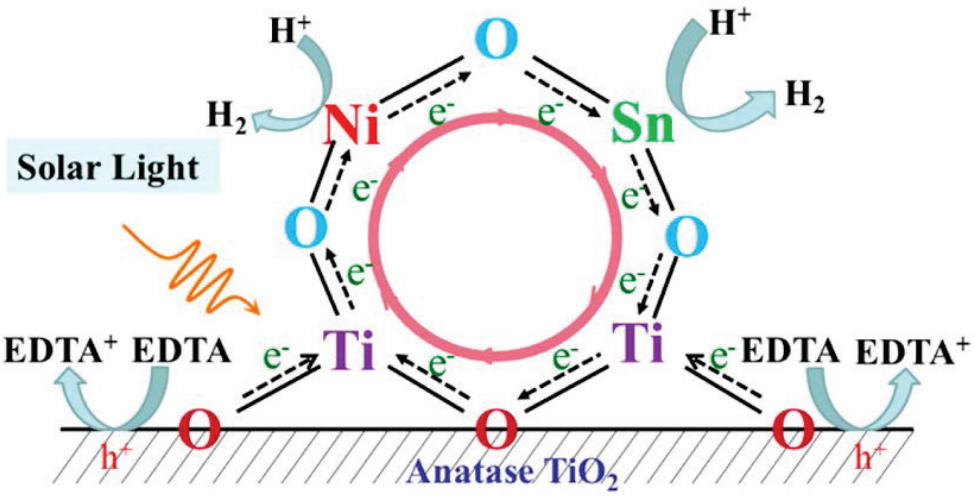

Figure 1.11 Schematic representation of electron delocalization in the ring of the [−Ti−O−Sn−O−Ni−O−Ti−O−] heteroatomic cluster.[107]

Unlike heterogeneous photo-catalysts prepared by methods such as wetness impregnation, spin coating, mechanical mixing, sol-gel method etc. SOMC can offer superior photo-catalysts by controlling and producing homogeneous surface active sites. This plays a vital role as formation of metal clusters with different M-O bonds can give rise to electron injections at different time intervals into bulk titania thereby reducing its overall activity. Furthermore, the efficiency can also be decreased due to the incompetence of some metal cluster with variable M-O bonds to harvest the incoming photons efficiently. Since, SOMC aims at “homogeneous” M-O bonds on the entire surface of titania, the electron injections are in a similar fashion as well as

all the surface bonded metal species have comparable light absorption and therefore higher photo-activity.

Part III: Goal of the thesis

1.9 Goal of the thesis

Although impressive, most of the examples mentioned above featuring catalysts prepared by SOMC on titania lack a common aspect; qunatitative analysis of surface hydroxyls and quantitative monitoring of the grafting reaction. TiO_2 anatase is composed of different crystal planes[115] such as (101), (001), (110) etc. having different concentration of surface hydroxyls and chemisorbed H_2O. Qualitative analysis can provide us information about the presence of these species but a lack of quantitative estimation of these surface species before grafting can lead to formation of non-homogeneous surface and can lead to deviation in understanding the fundamental chemistry of photocatalsysis on well-defined catalysts. At the same time, monitoring the reaction by quantitative estimation of organics released during the grafting process can provide incisive information about the structure of the surface species formed on the surface of titania.

Therefore, the aim of this PhD thesis was to establish the molecular foundation of a SOMC model on TiO_2. Firstly, a detailed quantitative and qualitative analysis of different reactive species on the surface of TiO_2 anatase from a SOMC point of view was carried out to understand the basic grafting procedure (chapter 3). $Ta[-CH_2C(CH_3)_3]_3[=CHC(CH_3)_3]$ was chosen as an organometallic precursor as its one of the most studied complex and has a well-defined structure on silica (chapter 4) and can be used as a reference for comparison. Doing so will allow us to get profound insights into the fundamental principles of photocatalytic reactions that employs MMCT mechanism which can eventually lead to high performance photocatalysts for solar driven chemistry. Furthermore, to take advantage of the large quantity of pentacoordinated Ti(IV) surface site, reactivity with 2-mehtyl imidazole was explored and is reported in chapter 4. Finally, we went on determining a self standing ordered TiO_2 nanotubes-Ti mesh system as future support for SOMC in PEC devices as reported in chapter 5. Chapter 6 includes the general conclusions and future prospects with respect to SOMC on TiO_2.

1.10 References

(1) Wernicke, H.-J.; Fischer, R. W. *Chemie Ing. Tech.* **2006**, *78* (7), 825–834.

(2) Somorjai, G. A.; McCrea, K. *Appl. Catal. A Gen.* **2001**, *222* (1–2), 3–18.

(3) Vittoria, A.; Meppelder, A.; Friederichs, N.; Busico, V.; Cipullo, R. *ACS Catal.* **2017**, *7* (7), 4509–4518.

(4) Beyramabadi, S. A.; Eshtiagh-Hosseini, H.; Housaindokht, M. R.; Morsali, A. *Organometallics* **2008**, *27* (1), 72–79.

(5) Anthony Haynes, Peter M. Maitlis, G. E. M.; Sunley, G. J.; Adams, H.; Badger, P. W.; Bowers, C. M.; Cook, D. B.; Elliott, P. I. P.; Ghaffar, T.; Helena Green; Griffin, T. R.; Payne, M.; Pearson, J. M.; Taylor, M. J.; Paul W. Vickers, A.; Watt, R. J. *J. Am. Chem. Soc.* **2004**, *126* (9), 2847–2861.

(6) Takehira, K.; Hayakawa, T.; Ishikawa, T. *Bull. Chem. Soc. Jpn.* **1980**, *53* (8), 2103–2110.

(7) Dalton, J. C. S.; Austin, J. M.; Groenewald, T.; Spiro, M. *J. Chem. Soc., Dalt. Trans.* **1980**, *0*, 854–859.

(8) Lefebvre, F. In *The Royal Society of Chemistry*; **2014**; pp 1–26.

(9) Hutchings, G. J.; Védrine, J. C. In *Springer Berlin Heidelberg: Berlin, Heidelberg*; Springer, Berlin, Heidelberg, **2004**; pp 215–258.

(10) Ezinkwo, G. O.; Tretyakov, V. P.; Aliyu, A.; Ilolov, A. M. *ChemBioEng Rev.* **2014**, *1* (5), 194–203.

(11) Leach, B. *Applied Industrial Catalysis.*; Elsevier Science, **1983**.

(12) Copéret, C.; Chabanas, M.; Petroff Saint-Arroman, R.; Basset, J.-M. *Angew. Chemie Int. Ed.* **2003**, *42* (2), 156–181.

(13) Candy, J.-P.; Copéret, C.; Basset, J.-M. In *Surface and Interfacial Organometallic Chemistry and Catalysis*; Copéret, C., Chaudret, B., Ed.; Springer-Verlag: Berlin/Heidelberg, **2005**; pp 151–210.

(14) Dufaud, V.; Niccolai, G. P.; Thivolle-Cazat, J.; Basset, J.-M. *J. Am. Chem. SOC* **1995**, *117*, 4288–4294.

(15) Basset, J.-M.; Baudouin, A.; Bayard, F.; Candy, J.-P.; Copret, C.; De Mallmann, A.; Godard, G.; Kuntz, E.; Lefebvre, F.; Lucas, C.; Norsic, S.; Pelzer, K.; Quadrelli, A.; Santini, C.; Soulivong, D.; Stoffelbach, F.; Taoufik, M.; Thieuleux, C.; Thivolle-Cazat, J.; Veyre, L. In *Modern Surface Organometallic Chemistry*; Wiley-VCH Verlag GmbH & Co. KGaA: Weinheim, Germany, **2009**; pp 23–73.

(16) Marks, T. J. *Acc. Chem. Res* **1992**, *25* (2), pp 57-65.

(17) Wegener, S. L.; Marks, T. J.; Stair, P. C. *Acc. Chem. Res.* **2012**, *45* (2), 206–214.

(18) Tada, M.; Iwasawa, Y. *Coord. Chem. Rev.* **2007**, *251*, 2702–2716.

(19) Anwander, R. *Chem. Mater.* **2001**, *13*, 4419–4438.

(20) Liang, Y.; Anwander, R. *Dalt. Trans.* **2013**, *42* (35), 12521.

(21) Guzman, J.; Gates, B. C. *Dalt. Trans.* **2003**, *0* (17), 3303.

(22) Serna, P.; Gates, B. C. *Acc. Chem. Res* **2014**, *47*, pp 2612-2620.

(23) Thomas, J. M.; Raja, R.; Lewis, D. W. *Angew. Chemie Int. Ed.* **2005**, *44* (40), 6456–6482.

(24) Dal Santo, V.; Liguori, F.; Pirovano, C.; Guidotti, M. *Molecules* **2010**, *15* (6), 3829–3856.

(25) Rimoldi, M.; Mezzetti, A. *Catal. Sci. Technol.* **2014**, *4* (9), 2724–2740.

(26) Yermakov, Y. I.; Kuznetsov, B. N. *J. Mol. Catal.* **1980**, *9* (1), 13–40.

(27) Zakharov, V. A.; Yermakov, Y. I. *Catal. Rev.* **1979**, *19* (1), 67–103.

(28) Copéret, C.; Comas-Vives, A.; Conley, M. P.; Estes, D. P.; Fedorov, A.; Mougel, V.; Nagae, H.; Núnez-Zarur, F.; Zhizhko, P. A. *Chem. Rev.* **2016**, *116* (2), 323–421.

(29) Chabanas, M.; Quadrelli, E. A.; Fenet, B.; Copéret, C.; Thivolle-Cazat, J.; Basset, J.-M.; Lesage, A.; Emsley, L. *Angew. Chemie Int. Ed.* **2001**, *40* (23), 4493.

(30) McDaniel, M. P.; Welch, M. B. *J. Catal.* **1983**, *82* (1), 98–109.

(31) Banks, R. L.; Bailey, G. C. *Ind. Eng. Chem. Prod. Res. Dev.* **1964**, *3* (3), 170–173.

(32) Tina M. Trnka; Grubbs, R. H. *Acc. Chem. Res.* **2001**, *34* (1), 18–29.

(33) Hoveyda, A. H.; Schrock, R. R. *Chemistry (Easton).* **2001**, *7* (5), 945–950.

(34) Hartwig, J. F. (John F. *Organotransition metal chemistry : from bonding to catalysis*; **2010**.

(35) Millot, N.; Santini, C. C.; Lefebvre, F.; Basset, J.-M. *Comptes Rendus Chim.* **2004**, *7* (8–9), 725–736.

(36) Romain Petroff Saint-Arroman; Mathieu Chabanas; Anne Baudouin; Christophe Copéret; Jean-Marie Basset; Anne Lesage, and; Lyndon Emsley. *J. Am. Chem. Soc.* **2001**, *123* (16), 3820–3821.

(37) Mathieu Chabanas; Anne Baudouin; Christophe Copéret, and; Basset, J.-M. *J. Am. Chem. Soc.* **2001**, *123* (9), 2062–2063.

(38) Bilhou, J. L.; Bilhou-Bougnol, V.; Graydon, W. F.; Basset, J. M.; Smith, A. K. *J. Mol. Catal.* **1980**, *8* (4), 411–429.

(39) Nédez, C.; Lefebvre, F.; Basset, J.-M. *Langmuir* **1996**, *12* (4), 925–929.

(40) Dufour, P.; Houtman, C.; Santini, C. C.; Basset, J.-M. *J. Mol. Catal.* **1992**, *77* (3), 257–272.

(41) Theolier, A.; Smith, A. K.; Leconte, M.; Basset, J. M.; Zanderighi, G. M.; Psaro, R.; Ugo, R. *J. Organomet. Chem.* **1980**, *191* (2), 415–424.

(42) Le Roux, E.; Taoufik, M.; Baudouin, A.; Copéret, C.; Thivolle-Cazat, J.; Basset, J.-M.; Maunders, B. M.; Sunley, G. J. *Adv. Synth. Catal.* **2007**, *349* (1–2), 231–237.

(43) Hugues, F.; Bassett, J. M.; Taarit, Y. Ben; Choplin, A.; Primet, M.; Rojas, D.; Smith, A. K. *J. Am. Chem. Soc.* **1982**, *104* (25), 7020–7024.

(44) Théolier, A.; Custodero, E.; Choplin, A.; Basset, J.-M.; Raatz, F. *Angew. Chemie* **1990**, *102* (7), 803–805.

(45) Wang, X. X.; Lefebvre, F.; Patarin, J.; Basset, J.-M. *Microporous Mesoporous Mater.* **2001**, *42* (2–3), 269–276.

(46) Bendjeriou-Sedjerari, A.; Pelletier, J. D. A.; Abou-Hamad, E.; Emsley, L.; Basset, J.-M. *Chem. Commun.* **2012**, *48* (48), 3067–3069.

(47) Zhuravlev, L. T. *Colloids Surfaces A Physicochem. Eng. Asp.* **2000**, *173*, 1–38.

(48) Aristov. B, Kiselev, A. *Zh. Fiz. Khim.* **1964**, *38* (8), 1984–1989.

(49) Zimnoch, J. H.; Santos, D.; Krug, C.; Barbosa, M.; Rosa, D.; Stedile, F. C.; Dupont, J.; De, M.; Forte, C. *J. Mol. Catal. A Chem.* **1999**, *139*, 199–207.

(50) Kazanskii, V. B. *Kinet. Catal.* **1987**, *28* (3), 482–489.

(51) Bartram, M. E.; Michalske, T. A.; Rogers, J. W. *J. Phys. Chem* **1991**, *95*, 4453–4463.

(52) Samantaray, M. K.; Dey, R.; Kavitake, S.; Basset, J.-M. Springer, Cham, **2015**; pp 155–187.

(53) Copéret, C.; Maury, O.; Thivolle-Cazat, J.; Basset, J.-M. *Angew. Chemie Int. Ed.* **2001**, *40* (12), 2331–2334.

(54) Buffon, R.; Leconte, M.; Choplin, A.; Basset, J.-M. *J. Chem. Soc. Dalt. Trans.* **1994**, 12, 1723.

(55) Buffon, R.; Leconte, M.; Choplin, A.; Basset, J.-M. *J. Chem. Soc. Chem. Commun.* **1993**, 4, 361.

(56) Michelle Jezequel; Véronique Dufaud; Maria José Ruiz-Garcia; Fernando Carrillo-Hermosilla; Ute Neugebauer; Gerald P. Niccolai; Frédéric Lefebvre; François Bayard; Judith Corker; Steven Fiddy; John Evans; Jean-Pierre Broyer; Jean Malinge, and; Jean-Marie Basset. . *Am. Chem. Soc.* **2001**, *123* (15), 3520–3540.

(57) Avenier, P.; Taoufik, M.; Lesage, A.; Solans-Monfort, X.; Baudouin, A.; de Mallmann, A.; Veyre, L.; Basset, J.-M.; Eisenstein, O.; Emsley, L.; Quadrelli, E. A. *Science* **2007**, *317* (5841), 1056 LP-1060.

(58) Quadrelli, E. A.; Centi, G. *ChemSusChem* **2011**, *4* (9), 1179–1181.

(59) Quadrelli, E. A.; Centi, G.; Duplan, J.-L.; Perathoner, S. *ChemSusChem* **2011**, *4* (9), 1194–1215.

(60) Majcen, Nineta; Vilela, B. *EuCheMS* **2017**, 1–22.

(61) Gerhard Pfaff; Reynders, P. *Chem. Rev.* **1999**, *99* (7), 1963–1982.

(62) Salvador, A.; Pascual-Martí, M. C.; Adell, J. R.; Requeni, A.; March, J. G. *J. Pharm. Biomed. Anal.* **2000**, *22* (2), 301–306.

(63) Zallen, R.; Moret, M. P. *Solid State Commun.* **2006**, *137* (3), 154–157.

(64) Braun, J. H.; Baidins, A.; Marganski, R. E. *Prog. Org. Coatings* **1992**, *20* (2), 105–138.

(65) Yuan, S.; Chen, W.; Hu, S. *Mater. Sci. Eng. C* **2005**, *25* (4), 479–485.

(66) Fujishima, a; Honda, K. *Nature* **1972**, *238* (5358), 37–38.

(67) Grätzel, M. *Nature* **2001**, *414* (6861), 338–344.

(68) Hagfeldt, A.; Graetzel, M. *Chem. Rev.* **1995**, *95* (1), 49–68.

(69) Linsebigler, A. L.; Lu, G.; Yates, J. T. *Chem. Rev.* **1995**, *95* (3), 735–758.

(70) Mills, A.; Le Hunte, S. *J. Photochem. Photobiol. A Chem.* **1997**, *108* (1), 1–35.

(71) Schrauzer,N. Guth, T. D. *J. Am. Chem. Soc.* **1977**, *99* (22), 7189–7193.

(72) Inoue, Tooru; Fujishima, Akira; Konishi, Satoshi; Kenichi, H. *Nature* **1979**, *277*, 637–638.

(73) Zhuang, H.; Zhang, Y.; Chu, Z.; Long, J.; An, X.; Zhang, H.; Lin, H.; Zhang, Z.; Wang, X. *Phys. Chem. Chem. Phys.* **2016**, *9636* (18), 9636–9644.

(74) Harima, Y.; Fujita, T.; Kano, Y.; Imae, I.; Komaguchi, K.; Ooyama, Y.; Ohshita, J. *J. Phys. Chem. C* **2013**, *117* (32), 16364–16370.

(75) Alivisatos, A. P. *Science (80-.).* **1996**, *271* (5251), 933–937.

(76) Alivisatos, A. P. *J. Phys. Chem.* **1996**, *100* (31), 13226–13239.

(77) Clemens Burda; Xiaobo Chen; Radha Narayanan, and; Mostafa A. El-Sayed. *Chem. Rev.* **2005**, *105* (4), 1025–1102.

(78) Murray, C. B.; Kagan, C. R.; Bawendi, M. G. *Annu. Rev. Mater. Sci.* **2000**, *30* (1), 545–610.

(79) Schneider, J.; Matsuoka, M.; Takeuchi, M.; Zhang, J.; Horiuchi, Y.; Anpo, M.; Bahnemann, D. W. *Chem. Rev.* **2014**, *114*, 9919–9986.

(80) Zhang, Y.; Jiang, Z.; Huang, J.; Lim, L. Y.; Li, W.; Deng, J.; Gong, D.; Tang, Y.; Lai, Y.; Chen, Z. *RSC Adv.* **2015**, *5*, 79479–79510.

(81) Ge, M.; Cao, C.; Huang, J.; Li, S.; Chen, Z.; ZHANG, K.-Q.; Al-deyab, S. S.; Lai,

Y. *J. Mater. Chem. A* **2016**, *4*, 6772–6801.

(82) Di Paola, A.; Bellardita, M.; Palmisano, L. *Catalysts* **2013**, *3* (1), 36–73.

(83) Landmann, M.; Rauls, E.; Schmidt, W. G. *J. Phys. Condens. Matter* **2012**, *24*, 195503–195506.

(84) Setvin, M.; Franchini, C.; Hao, X.; Schmid, M.; Janotti, A.; Kaltak, M.; Van De Walle, C. G.; Kresse, G.; Diebold, U. *Phys. Rev. Lett.* **2014**, *113* (8), pp 086402(5).

(85) Zhang, J.; Zhou, P.; Liu, J.; Yu, J. *Phys. Chem. Chem. Phys.* **2014**, *16* (16), 20382–20386.

(86) Rao, M. V.; Rajeshwar, K.; Verneker, V. R. P.; DuBow, J. *J. Phys. Chem.* **1980**, *84* (15), 1987–1991.

(87) J. Jitputtia,S. Pavasupree, Y. Suzuki, S. Y. *J. Solid State Chem.* **2007**, *180* (5), 1743–1749.

(88) Karakitsou, K. E.; Verykios, X. E. *J. Phys. Chem.* **1993**, *97* (6), 1184–1189.

(89) Kolen'ko, Y. V.; Churagulov, B. R.; Kunst, M.; Mazerolles, L.; Colbeau-Justin, C. *Appl. Catal. B Environ.* **2004**, *54* (1), 51–58.

(90) Odling, G.; Robertson, N. *ChemSusChem* **2015**, *8* (11), 1838–1840.

(91) Sreethawong, T.; Suzuki, Y.; Yoshikawa, S. *Catal. Commun.* **2005**, *6* (2), 119–124.

(92) Sreethawong, T.; Suzuki, Y.; Yoshikawa, S. *J. Solid State Chem.* **2005**, *178* (1), 329–338.

(93) Korzhak, A. V.; Ermokhina, N. I.; Stroyuk, A. L.; Bukhtiyarov, V. K.; Raevskaya, A. E.; Litvin, V. I.; Kuchmiy, S. Y.; Ilyin, V. G.; Manorik, P. A. *J. Photochem. Photobiol. A Chem.* **2008**, *198* (2–3), 126–134.

(94) Tian, Q.; Zhang, Z.; Yang, L.; Hirano, S. *J. Mater. Chem. A* **2015**, *3* (28), 14721–14730.

(95) Albo, R. *Am. Perfum. Aromat.* **1960**, *75*, 7–35.

(96) Mollavali, M.; Falamaki, C.; Rohani, S. *Int. J. Hydrogen Energy* **2015**, *40* (36), 12239–12252.

(97) Mohamed, A. M.; Aljaber, A. S.; AlQaradawi, S. Y.; Allam, N. K. *Chem. Commun. (Camb).* **2015**, *51* (63), 12617–12620.

(98) Eda, S.; Moriyasu, K.; Fujishima, M.; Nomura, S.; Tada, H. *RSC Adv.* **2013**, *3* (26), 10414.

(99) Yue, X.; Jin, X.; Wang, R.; Ni, L.; Jiang, S.; Qiu, S.; Zhang, Z. *Mater. Chem. Phys.* **2015**, 1–9.

(100) Li, X.; Zhuang, Z.; Li, W.; Pan, H. *Appl. Catal. A Gen.* **2012**, *429–430*, 31–38.

(101) Dvoranová, D.; Brezová, V.; Mazúr, M.; Malati, M. A. *Appl. Catal. B Environ.* **2002**, *37* (2), 91–105.

(102) Transactions, E. C. S.; Society, T. E. **2008**, *3* (43), 1–9.

(103) Yang, L.; Li, Z.; Jiang, H.; Jiang, W.; Su, R.; Luo, S.; Luo, Y. *Appl. Catal. B Environ.* **2016**, *183*, 75–85.

(104) Hamadanian, M.; Karimzadeh, S.; Jabbari, V.; Villagrán, D. *Mater. Sci. Semicond. Process.* **2016**, *41*, 168–176.

(105) Hoshino, K.; Kuchii, R.; Ogawa, T. *Appl. Catal. B Environ.* **2008**, *79* (1), 81–88.

(106) Martini, L. A.; Moore, G. F.; Milot, R. L.; Cai, L. Z.; Sheehan, S. W. *J.Phys.Chem.C* **2013**, *117* (28), pp 14526−14533.

(107) Huang, H.; Lin, J.; Fan, L.; Wang, X.; Fu, X.; Long, J. *J. Phys. Chem. C* **2015**, *119* (19), 10478–10492.

(108) Guzman, J.; Kuba, S.; Fierro-Gonzalez, J. C.; Gates, B. C. *Catal. Letters* **2004**, *95* (1–2), 77–86.

(109) Gu, Q.; Long, J.; Fan, L.; Chen, L.; Zhao, L.; Lin, H.; Wang, X. *J. Catal.* **2013**, *303* (September 2016), 141–155.

(110) Iwasawa, Y.; Sato, H. *Chem. Lett.* **1985**, 507–510.

(111) Grasser, S.; Haeßner, C.; Köhler, K.; Lefebvre, F.; Basset, J.-M. *Phys. Chem. Chem. Phys.* **2003**, *5* (9), 2–7.

(112) Huang, H.; Lin, J.; Zhu, G.; Weng, Y.; Wang, X.; Fu, X.; Long, J. *Angew. Chemie - Int. Ed.* **2016**, *55* (29), 8314–8318.

(113) Fan, L.; Long, J.; Gu, Q.; Huang, H.; Lin, H.; Wang, X. *J. Catal.* **2014**, *320* (1), 147–159.

(114) Gu, Q.; Long, J.; Zhou, Y.; Yuan, R.; Lin, H.; Wang, X. *J. Catal.* **2012**, *289* (September), 88–99.

(115) Bourikas, K.; Kordulis, C.; Lycourghiotis, A. *Chem. Rev.* **2014**, *114* (19), 9754–9823.

(116) Tahir, M.; Amin, N. S. *Energy Convers. Manag.* **2013**, *76*, 194–214.

Chapter 2

Experimental and Instrumental Technicalities

Chapter 2
Experimental and Instrumental Technicalities

Chapter 2

2.1 Introduction

Heterogeneous catalyst have interesting properties that are often linked to their physical and chemical properties such as morphology, crystallinity, crystallite and agglomerate size, surface area, porosity, electronic configuration, magnetic properties and surface's activity. TiO_2 is known for its photo-catalytic activity and its application as a heterogeneous catalyst needs to be characterized via surface analysis to determine applications of the final product. Relating material properties to structural characteristics also enables researchers to understand catalytic performance and design improved catalysts and catalyst supports.

In this work, X-ray diffraction, electron paramagnetic resonance and transmission electron microscopy were used to study the crystal structure, crystal size and phase, morphology and the identity and oxidation state of atoms in the structure. Physisorption and chemical titration techniques were used to study surface properties and porosity including the surface area, active metal surface area, pore diameter/width, pore geometry and number of active sites per geometric area of surface. DRIFT, FTIR and elemental analysis analysed the qualitative and quantitative aspects of surface species and grafted species. In this chapter, a brief overview of these techniques is presented. The materials used in the experimental work and the experimental methodologies used for all other tests are described in the pertinent chapters.

2.2 Synthetic procedures

2.2.1 Synthesis of $TiO_{2(700)}$ anatase nano powder

TiO_2 anatase nanopowder Alfa aesar (99.7%, 12 nm APS), Sigma Aldrich (< 25 nm, 99.7%) and Nanoarc™ (99.9%, 32 nm APS) were calcined at 450°C under dry air for 3h at heating and cooling rates of 3°C/min. This ensures the crystallinity of the nanoparticles. TiO_2 was then transferred under inert atmosphere into a 30cm long quartz reactor inside the glove box. Once sealed with the cap it was removed from glove box and subjected to dehydroxylation at 200°C, 500°C and 700°C for 12h under dynamic ultrahigh vacuum system (UHV) i.e. upto 10^{-5} Torr with heating and cooling rates of 3°C/min. respectively. After dehydroxylation, the samples were moved and stored inside glove box in sealed vials and characterized by DRIFT, UV-Vis., chemical titration etc.

2.2.2 Dehydration of 2-methyl Imidazole

2-Methyl imidazole (**2-mIm**) (ACROS Chemicals, 99%) was dehydrated at 90°C under dynamic vacuum (10^{-3} Torr) in a long tube. Typically a long tube containing 1g of 2-methyl Imidazole was half-immersed in an oil bath pre-heated at 90°C and the long tube was kept sealed under dynamic vacuum. At this point, sublimation of 2-mIm starts in the hotter region and crystals re-grow in the colder region of the tube. This process was continued for few hours to ensure complete removal of water. The tube was then moved into glove box and stored in a sealed vial. ^{1}H NMR ($CDCl_3$, 300 MHz): δ = 2.4 (3H, s, $-CH_3$), 6.9 (2H, s, -HC=CH-), 9.7 (1H, s, -NH).

2.2.3 Synthesis of $Ta[-CH_2C(CH_3)_3]_3[=CHC(CH_3)_3]$ precursor

$Ta[-CH_2C(CH_3)_3]_3[=CHC(CH_3)_3]$ (**1**) was prepared using TaCl5 and NpMgCl as reported by Schrock *et.al.*[1] The method consisted of 3 different steps involving purification and drying of neopentyl chloride, synthesis of neopentyl magnesium chloride and synthesis of organometallic complex (**1**).

a) Purification and drying of neopentyl chloride

100mL of neopentyl chloride (Strem chemicals) was stirred for 13h with 50mL of conc. H_2SO_4 (conc. H_2SO_4 is highly corrosive!!!). After 13h, stirring was stopped and the mixture was allowed to settle for 1h giving a dark orange acid layer and a colourless organic layer. The two layers were separated using a separating funnel. This procedure was repeated 3 times. The stirring duration was also varied depending on the colour of the acidic layer until a colourless layer was obtained. The organic layer at this stage was then washed with 2 x 50 mL of distilled water, 50 mL of sat. $NaHCO_3$ (pH=9) and again with 2 x 50 mL distilled water. Neopentyl chloride was then dried over CaH_2 for 30 minutes under sonication. It was then filtered on a glass wool, dried again on $CaCl_2$ for 72h at room temperature and distilled under reduced pressure. It was then freeze-pump-thawed (1 time) and stored in a rota flow schlenk flask.

b) Synthesis of Neopentyl magnesium Chloride

Three neck 250 ml round bottom flask containing Magnesium turnings (Sigma Aldrich, 6.8 g, 1.4 equiv), water condenser, calibrated addition burette (25 ml), magnetic bar were oven dried overnight and assembled while hot. System was kept under vacuum for 15 minutes followed by three cycles of argon and vacuum. Finally, it was kept under argon and then diethyl ether (70 ml) was cannulated into the flask. The reaction mixture was then stirred for 18 hr. Neopentyl chloride (24 ml, 1.0 equiv) was added dropwise for a period of 30 min. through an addition burette into the system while refluxing for 20h at 55°C. After 20h, the reaction was allowed to cool and then filtered over celite to give yellowish-brown solution. NpMgCl was then titrated with hydrazine of salicylaldehyde to determine the concentration of the NpMgCl solution. The colour of indicator turns yellow with the addition of NpMgCl and finally turns organish to indicate the end point.

c) Synthesis of $Ta[-CH_2C(CH_3)_3]_3[=CHC(CH_3)_3]$

Tantalum pentachloride (Strem Chemicals, 4.67g, 13.03 mmol, 1.0 equiv) was transferred into a schlenk fitted with addition burette. 120 ml of diethyl ether was added to the reaction mixture by addition burette followed by addition of 2/3 of NpMgCl dropwise. Colour of the solution changed from light yellow to dark green to brown. The reaction mixture was then stirred for 30 min. followed by addition of rest 1/3 NpMgCl. The brown solution obtained after filtration was evaporated under partial vacuum with slow heating with heat gun to afford a thick brown gel. This gel was then

subjected to sublimation to obtain brownish orange colored crystals of Ta[-$CH_2C(CH_3)_3]_3[=CHC(CH_3)_3]$. The crystals obtained were stored in a sealed vial inside glove box. ^1H NMR (C_6 D_6, 300 MHz): δ = 1.9 (^1H, s, =CH $^tBu_3$), 1.45 (9H, s, $=CHC(CH_3)_3$), 1.15 (27H, s, CH_2 $C(CH_3)_3$), 0.83 (6H, s, CH_2).

2.2.4 Pseudo CVD of 2-mIm on $TiO_{2(700)}$

300 mg of $TiO_{2(700)}$ anatase and 10 mg of 2-mIm were transferred into two pyrex crucibles inside the glove box respectively. The crucibles were then transferred into a pyrex reactor containing a spherical connector. The reactor was then removed from glove box and evacuated at UHV(~10^{-5} Torr) and placed into an oven pre heated at 120°C for 30 min. Upon, completion of reaction the reactor was allowed to cool to room temperature and then moved into glove box. $TiO_{2\ (700)}$ with chemisorbed as well as physisorbed 2-mIm was transferred into a sealed long glass tube inside glove box. The tube was then subjected to calcination at 200°C under UHV for 1h with heating and cooling rates of 3°C/ min. The final product obtained was then stored in glove box in a sealed vial and characterized by DRIFT, elemental analysis and SSNMR.

2.2.5 Impregnation of $Ta[-CH_2C(CH_3)_3]_3[=CHC(CH_3)_3]$ onto $TiO_{2(700)}$

In a double schlenk separated by a glass frit, $TiO_{2(700)}$ and Ta[-$CH_2C(CH_3)_3]_3[=CHC(CH_3)_3]$ (**1**) were placed in the two schlenk's respectively. Pentane distilled and dried on NaK alloy followed by degassing through freeze-pump-thaw cycles was introduced into schlenk containing complex (**1**). After complete dissolution, the solution was transferred into adjoining schlenk containing $TiO_{2(700)}$ via glass frit. The reaction took place at 25°C for 2h under magnetic stirring. At the end of reaction, the supernatant was separated and the solid was washed twice with pentane, dried under UHV and stored in a sealed vial inside glove box. The resultant solid was characterized by DRIFT, SSNMR, Elemental analysis etc.

2.2.6 Preparation of TNTs-Ti mesh photoanodes

Highly ordered TiO_2 nanotube arrays were prepared by controlled anodic oxidation of a macroporous Ti substrate (TNTs-Ti mesh). The method can be described as an electrochemically-induced growth of a thin TiO_2 layer on the external surface of a commercial Ti mesh, due to the application of a constant oxidizing voltage in the presence of fluoride-based electrolytes. The starting metallic substrate (supplied by Alfa Aesar) consists of Ti wires (0.13 mm diameter) regularly woven to form an 80 mesh gauze with an open geometric area of 36 %. Prior to the anodization, the Ti gauze

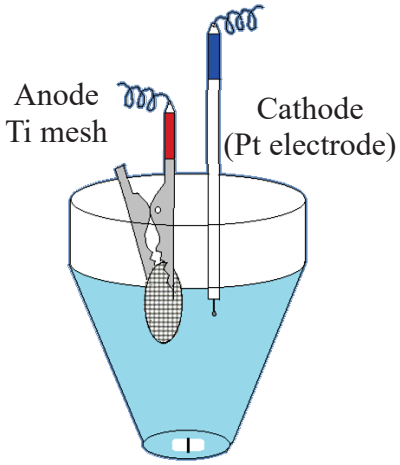

Figure 2.1 Schematic representation of electro-chemical cell used for anodic oxidation at University of Messina.

was sonicated for 30 min in isopropyl alcohol to remove any organic impurities and dried in air. Then, the clean substrate was located in a stirred electrochemical cell (Figure 2.1) to act as the working electrode, while a platinum wire was used as the cathode. A potentiostat (Agilent E3612A DC Power Supply) and a multimeter (Keithley 2000) interfaced to a personal computer were used to apply a constant bias between the two electrodes (in the range 40-60 V) for times of 1-7 h and save the current profile data. The constant set voltage was gradually reached by a programmed ramp rate of 5 V min^{-1}. The electrolyte bath was a 100 mL ethylene glycol solution with 2 vol% distilled H_2O and 0.3 wt % ammonium fluoride (Sigma Aldrich). At the end of the anodization process, the TNTs-Ti mesh was annealed at 450°C for 3 h under air with heating and cooling rates of 3°C min^{-1}, in order to induce crystallization of the amorphous TiO_2 nanotubes to the anatase phase. The internal part of the Ti wires, remaining non-oxidized after the anodization, acts as a conductive metallic mesh for

the collection of the electrons, which are then transferred to the cathode side through an external circuit.

2.3 Instrumental Techniques

2.3.1 Diffuse reflectance infrared fourier transform spectroscopy (DRIFTS)

Diffuse Reflectance Infrared Fourier Transform Spectroscopy (DRIFTS) is an infrared spectroscopy technique used on powder samples. DRIFT spectra were recorded on a Nicolet 6700-FT spectrometer using a cell equipped with CaF_2 window. Typically, 64 scans were accumulated for each spectrum (resolution 4 cm^{-1}).

2.3.2 In-operando DRIFTS-GC/MS

The experiments were carried out in an integrated system comprising mass flow controllers (Brooks), FT-IR adapted high temperature reaction chamber (Harrick Scientific) and online GC/MS (Agilent GC 6850 MS 5975C). The reaction chamber was equipped with ZnSe windows and fitted into the Praying Mantis optical unit also provided by Harrick. In the glove box, about 20 mg of powder sample was placed onto a porous stainless steel frit in the reaction chamber. Once the cell was inserted into the spectrophotometer, a controlled mass flow of argon (6 ml min^{-1}) was introduced into the reaction chamber at 1 bar. Heating was programmed from 20°C to 500°C temperature, using heating rate of 2°C min^{-1}. A DRIFT spectrum of 64 scans was recorded every minute. FT-IR spectra were recorded in a Nicolet 6700 spectrophotometer with a MCT detector and 4 cm^{-1} resolution.

2.3.3 Fourier transform infrared spectroscopy (FTIR)

Transmission FT-IR spectroscopy was used to study pellets. A pellet was prepared inside glove box using $TiO_{2(700)}$ nano powder. The pellet was then placed between the 2 windows of the round cell. A Nicolet 5700-FT spectrometer and infrared cell equipped with ZnSe windows was used to perform FT-IR spectroscopy. Typically, 32 scans were accumulated for each spectrum (resolution 1 cm^{-1}).

2.3.4 UV-Vis spectroscopy

UV-visible spectroscopy were performed on Perkin Elmer Lambda 1050 spectrophotometer equipped with Praying Mantis^{TM} and unique PMT, InGaAs and PbS 3-detector module was used to record absorption spectra of solid powder. The absorption spectrum was measured as function of wavelength in the range of 200-800nm. Dry $BaSO_4$ was used as a reference to calibrate the instrument. A cell equipped with a quartz dome was used to record absprtion spectra of all samples. Jasco V570 spectrometer equipped with an integrating sphere for solid samples using $BaSO_4$ as reference was used for measuring the absorption spectrum of TNTs-Ti mesh.

2.3.5 N_2 adsorption and desorption isotherms

Belsorp-Max from BEL-JAPAN was used to measure nitrogen adsorption desorption isotherm at 77K after degassing the sample. Typically, ~300 mg of powder was filled in the cell. For $TiO_{2(200)}$, $TiO_{2(500)}$ and $TiO_{2(700)}$ the BET cells were filled inside glove box. The specific surface area of the sample powder was then calculated according to the BET model which takes into account the amount of gas adsorbed on the surface of the powder sample as a function of adsorbate gas pressure. BJH method was used to calculate the pore size.

2.3.6 Nuclear magnetic resonance spectroscopy (NMR)

Solution NMR spectra were recorded on BRUKER AVANCE 300 spectrometer (^{1}H: 300.1 MHz, ^{13}C: 75.4 MHz). Chemical shifts are given in ppm (h) relative to TMS (tetramethylsilane). Spectra were recorded using the residual peak of the deuterated solvent as internal standard.

Solid state NMR spectra were collected on BRUKER AVANCE III 500 spectrometer operating at 125 MHz for ^{13}C. The zirconia impeller of 4mm is filled with the desired product inside glove box under Argon and sealed with a kel-f stopper. It was then transferred into the probe Bruker CP 4 mm spectrometer allowing rotation of the rotor at a speed of 10 kHz. The time between two acquisitions was always optimized to allow complete relaxation of the protons.

2.3.7 Gas Chromatography (GC)

Gas phase analysis was performed on a HP 5890 gas chromatograph, equipped with a flame ionization detector (FID) and a KCl/Al_2O_3 on fused silica column (50 m × 0.32 mm). Gaseous alkanes from the reaction were filled into a glass balloon of known volume. A spherical syringe joint was used to extract 300µL of gaseous product into a gas syringe and was injected into GC.

2.3.8 X-ray Diffraction Spectroscopy (XRD)

The crystallographic information of all samples was investigated by Mr. Ruben Vera at CDHL, University of Lyon (Villeurbanne) by powder X-ray diffraction (XRD, Bruker D8 Advance, Cu, Kα radiation, λ =1.5406 Å, 40 kV, 40 mA). The samples were prepared in the form of fine homogeneous powder. A thin smooth layer of the samples mounted on a non-crystalline substrate such as PMMA (Poly (methylmethacrylate)) was held in the path of X-rays. The diffracted X-rays correspond to all sets of planes in the crystal powder which could be orientated in every possible direction relative to the X-ray beam. The XRD patterns with diffraction intensity versus 2θ were recorded, usually from 10° to 70° at a scanning speed of 2° per min. A LYNXEYE XE detector with an opening of 3° was used to detect the diffracted beam. The well–known Bragg's equation can be used to determine the interlayer space of the crystals $d= \lambda/ (2\sin \theta)$, where θ is the diffraction angle. The average crystallite sizes, Dhkl, can be calculated by the Debye-Scherrer formula with the full width at half maximum (FWHM) of the peaks $D_{hkl}= 0.9 \lambda/ (FWHM \times \cos\theta)$. X-Ray Diffraction (XRD) using a D2 Phaser Bruker diffractometer equipped with a Cu-Kα radiation source and operated at 30 kV and 10 mA. Data were collected at a scanning rate of 0.025° s^{-1} in a 2θ range from 12° to 80° for TNTs-Ti mesh.

2.3.9 Electron paramagnetic resonance spectroscopy (EPR)

Electron paramagnetic resonance (EPR) experiments were performed by Mr. Lhoussain Khrouz at ENS de Lyon on a Bruker EXELSYS E500 spectrometer at 120 K. A microwave frequency (ν) of 9.4 GHz and a power of 6 mW were used. The relative spin concentration and the g factor were calculated using g mark as an internal

standard (V(IV) diluted in SiO_2). The air-tight reactor cell for EPR measurements was made of quartz (4 mm i.d.) and was normally charged with a precise weight of sample, ca. 0.01 g, within a glove-box. The simulations were done on Matlab toolbox using easyspin method.

2.3.10 High Resolution Transmission Electron Microscopy (HRTEM)

Conventional TEM micrographs were performed at the "Centre Technologique des Microstructures", UCBL, Villeurbanne, France, using a JEOL 2100F electron microscope. The acceleration voltage was 200 kV. The samples were prepared by dispersing a drop of the ethanol suspension of a ground sample on a Cu grid covered by a carbon film.

2.3.11 Scanning Electron Microscopy (SEM)

The structural and morphological characterization of the TNTs were performed by a scanning electron microscope (SEM) with Quanta 250 FEG FEI high resolution field emission gun, equipped with energy dispersive x-ray (EDX) analyser, at the "Centre Technologique des Microstructures" (CTμ, Villeurbanne, France).

2.3.12 Elemental Analysis

Elemental analysis (C, H and N) were performed at the Welience – Pôle Chimie Moléculaire Faculté des Sciences Mirande (Dijon, France), using CHNS/O thermo electron flash 1112 Series elemental analyser. A Heraeus/Mannertz/Pascher C-H-N analyser and iCap 6500 (Thermo Fisher Scientific) were used to analyse organometallic complexes at the Mikoanalytisches Labor Pascher in Remagen-Bandorf, Germany.

2.3.13 Chronoamperometry

Chronoamperometry measurements were performed by Francesco Tavella at University of Messina by the use of a three-electrode photo-electrochemical cell, with

a Pt wire as counter-electrode and a saturated Ag/AgCl reference electrode. All the tests were performed at room temperature in 1 M KOH solution at 0.1 V using a 2049 AMEL potentiostat-galvanostat.

2.3.14 Photo-Electro Catalytic device (PEC)

The experimental apparatus for photocatalytic water splitting was developed by Prof. Siglinda Perathoner, Prof. Gabriele Centi and Dr. Claudio Ampelli at University of Messina. The set-up consists of a solar illuminator source, a photo-electrocatalytic (PEC) device and a gas chromatograph for on-line analysis. The lamp housing is furnished with a Xe-arc lamp (ORIEL, 300 W), a set of lenses for light collection and focusing, and a water filter to eliminate the infrared radiation. In particular, the following filters were used to select the desired wavelength region:

- AM 1.5 G (simulating the standard terrestrial solar spectrum);

- UVC blocking filter (LSZ178, Lot Oriel);

- UVB/UVC blocking filter (LSZ179, Lot Oriel);

- Vis-IR blocking filter (LSZ177, Lot Oriel).

The PEC reactor, made of Plexiglas and equipped with a quartz window, is homemade. It has a two-electrode configuration with two compartments for separated evolution of H_2 and O_2. The photoanode is the anodized Ti mesh (with TiO_2 nanotubes), while the cathode is a commercial gas diffusion layer (GDL S10BC SIGRACET®, 0.5 mg Pt cm^{-2}). As shown in Figure 2.2, the two electrodes were joined together as a MEA (Membrane Electrode Assembly, in analogy with fuel cells) by a proton-conductive membrane (Nafion® 212). The irradiated area was 3.7 cm^2 and 1 M NaOH and 0.5 M H_2SO_4 aqueous solutions were used as electrolytes in the anodic and cathodic compartments, respectively. Each solution circulates continuously between the solar cell and an outer reservoir. A potentiostat-galvanostat (AMEL 2049) was used to measure the generated photocurrent. H_2 and O_2 amounts were periodically determined by a gas chromatograph (GC), equipped with a molecular sieve 5Å column and a thermal conductivity detector (TCD). Figure 1 shows a schematic depiction of the MEA with details about the charge transport through the membranes in the PEC cell.

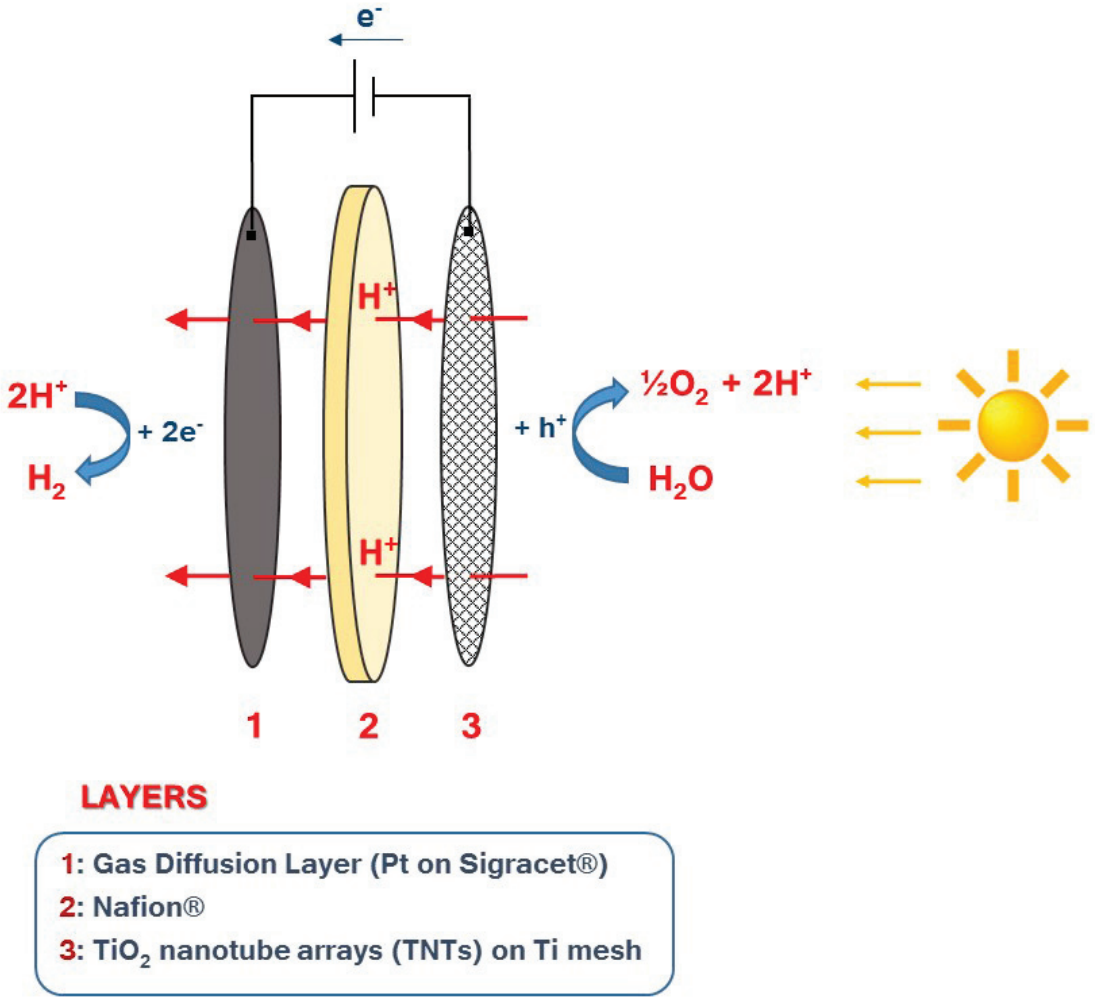

Figure 2.2 Schematic depiction of the MEA (Membrane Electrode Assembly) with a 3D-type structured Ti mesh as photoanode in the PEC cell.

2.4 References

(1) Schrock, R. R. *Acc. Chem. Res.* **1979**, *12* (3), 98–104.

Chapter 3

Characterization of Titania surface properties from a SOMC perspective

Chapter 3

Characterization of Titania surface properties from a SOMC perspective

Chapter 3

3.1 Introduction

TiO_2 has been considered of paramount importance due to its application in photocatalysis and photoelectrochemistry.[1–6] TiO_2 exists in different polymorphs such as anatase, rutile and brookite. Among these anatase and rutile are the most common crystal structures.[7] Both anatase and rutile crystals are formed by a Titanium atom surrounded by 6 oxygen atoms to form a TiO_6 octahedra (Figure 3.1). The octahedron in TiO_2 rutile is asymmetrical, showing slightly orthorhombic distortion, whereas the

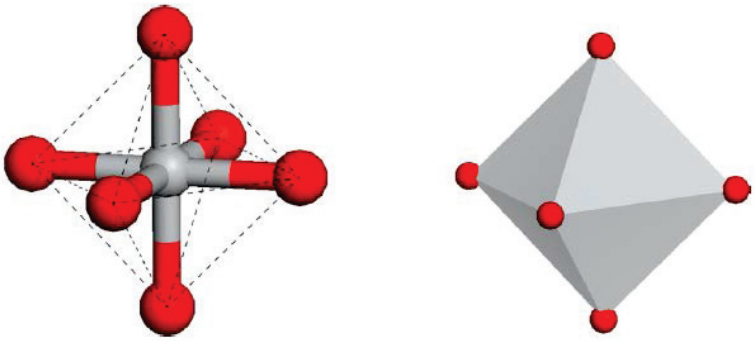

Figure 3.1 Schematic representation of the distorted TiO_6 octahedron of TiO_2 (anatase and rutile). Each Ti atom (grey ball) is coordinated to the six neighbouring oxygen atoms (red balls) through two apical and four equatorial bonds of lengths 1.979 and 1.932 Å, respectively, for anatase (the corresponding lengths for rutile are 1.976 and 1.946 Å, respectively).[59]

TiO_2 anatase clearly shows orthorhombic distortion, resulting in lower symmetry than the orthorhombic system. The bandgap of TiO_2 anatase is 3.2 eV while TiO_2 rutile exhibits a band gap of 3.0 eV.[8] Despite of the higher band gap anatase exhibits superior photoactivity then rutile due to its low packing density (3.8-3.9 g/cm^3).[7,9] Anatase is thermo-dynamically the less stable polymorph, but also the more probable phase when the TiO_2 grain size is very small (~ 10 nm) as calculated from surface energy.[10] The

physical and chemical properties of TiO_2 anatase and the grafting species largely depends on the surface of particles a few nanometers in size.[11] Therefore, it is essential to characterize qualitatively and quantitatively the entities that are present on the surface of TiO_2 anatase before undertaking SOMC.

Anatase crystals primarily consists of (101), (100), (001), (110) and (103) crystal planes exposed to the surface depending on their preparation procedure. Figure 3.2 depicts a schematic representation of ideal anatase crystal planes. Mostly, the observed shapes exhibit (101) and (001) surfaces, although sometimes other facets may be

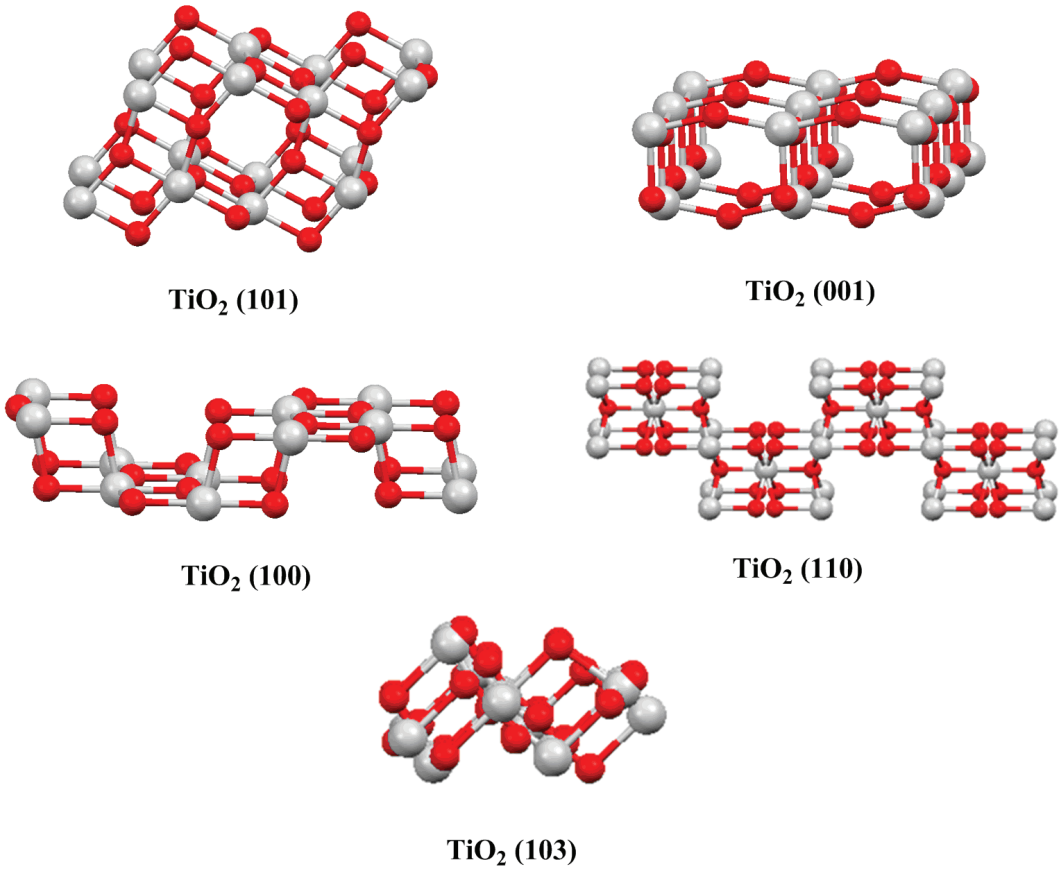

Figure 3.2 Schematic representation of anatase (101), (001), (100), (110) and (103) crystal planes.

observed depending on the synthesis conditions.[12–14] The facets play an important role in determining the activity of TiO_2 as a catalyst. It also plays a vital role in understanding the position and type of surface hydroxyls present on the titania support which in turn helps in understanding the mechanism of SOMC grafting on titania's surface.

By default, for anatase crystals generally (101) and (001) are exposed in Wulff construction.[15] On the (101) facet, both 5-fold and 6-fold coordinated Ti atoms(Ti_{5c}, Ti_{6c}) as well as 2-fold and 3-fold coordinated O atoms (O_{2c}, O_{3c}) are present. On the (001) facet, Ti_{5c} atoms as well as O_{2c} and O_{3c} atoms are exposed. On the (100) facet, both O_{2c} and O_{3c} atoms are exposed, whereas the outermost Ti atoms are 5-fold coordinated. Moreover, Ti_{6c} atoms and O_{3c} atoms are present at the bottom of surface grooves. The first layer of (110) facet comprises of Ti_{4c} and O_{2c} atoms exposed to the surface whereas Ti_{6c} and O_{3c} atoms are on the second layer. The atoms of the first layer on the ideal surface form linear O−Ti−O units and are arranged in a rectangular structure. The (103) surface has two possible terminations called "faceted" ((103)f) and "smooth" ((103)s) terminations.[16] The 1-fold-coordinated oxygen does not appear. From the discussion above, it is clear that undercoordinated oxygen is always present on all the surfacs as O_{2c}. O_{1c} does not appear. In contrast, the undercoordinated Ti atoms are present in two forms, as Ti_{5c} {(101), (100), (001), "faceted" (103)} and 4-fold-coordinated {"smooth" (103) and (110)}. Therefore, since we have the predominance of (101) we can expect the presence of surface hydroxyls or chemisorbed water on (101) facet.

Table 3.1 summarizes the coordinated and uncoordinated Ti and O atoms present on different facets of anatase crystal. As one may observe an average of 10 atoms/nm^2 are present for both the elements. Uncoordinated Ti species acts as lewis acidic sites while the corresponding O species acts as bronsted base. In presence of water molecules on surface of anatase increase the formation of bronsted sites (surface hydroxyls) thereby decreasing the concentration of lewis acidic sites. Therefore, when anatase comprising of surface water molecules is treated *via* a) UV irradiation, b) calcination or annealing under reduced pressure or c) particle (Electron, Neutron and γ-ray) bombardment; most of the surface water molecules are eradicated thereby increasing the concentration of surface Lewis sites. These surface Lewis acidic (Ti_{5c}, Ti_{4c}) sites act as active centres for formation of stable coordination bonds.

Table 3.1 Surface density (sites per nm^2) of atoms exposed by different crystal facets of anatase.[17]

Anatase crystal surface	*Ti_{6c}*	*Ti_{5c}*	*Ti_{4c}*	*O_{2c}*	*O_{3c}*
(101)	5.1	5.1		5.1	5.1
(100)	5.4	5.4		5.4	5.4
(001)		6.9		6.9	6.9
(110)			3.8	7.7	

Apart, from surface Lewis acidity, the surface of anatase encompasses different hydroxyls, physisorbed and chemisorbed water on different crystal planes. Since, it is important to control the concentration of hydroxyls on oxides to perform SOMC (as discussed in chapter 1), partial dehydroxylation is usually carried out to eliminate the physisorbed water and model the surface hydroxyl entities. In case of TiO_2 anatase, various kinds of surface hydroxyls and coordinated water upon partial dehydroxylation have been reported in literature. These surface entities have been mainly characterized by infrared spectroscopy. Table 3.2 reports a brief summary of different peak assignments of surface hydroxyls and coordinated water on different crystal planes of anatase.

Table 3.2 Infrared frequencies of different hydroxyls/H_2O groups on TiO_2 anatase observed experimentally.

Sr. No.	*ν (OH) (cm^{-1})*	*Surface structural implications*	*Plane of anatase*	*Reference*
1	1600-1640	Ti_{5c}-OH_2	(101)	[17]
2	3474	H-bonded OH's	(101)	[18]
3	3495	chemisorbed H_2O	(100)	[19]
4	3573	H-bonded OH's	(101)	[18]
5	3620-3680	Ti_{6c}-OH_2	(101)	[17]
6	3634	non H-bonded OH's	(101)	[18]
7	3640	isolated OH's		[20]

Sr. No.	*ν (OH) (cm^{-1})*	*Surface structural implications*	*Plane of anatase*	*Reference*
8	3665	H-bonded OH's	(001)	[21]
9		bridging OH's		[22]
10	3670	bridging OH's	(101)	[18]
11		Ti^{4+}-OH-Ti^{4+}		[20]
12	3675	free surface OH's		[23]
13	3676	isolated OH's	(001)	[19]
14	3685	bridging OH's		[22]
15	3690	Ti^{4+}-OH-Ti^{3+}		[20]
16		Ti_{6c}-OH	(100)	[17]
17	3694	chemisorbed H_2O	(100)	[19]
18	3696	non H-bonded OH's	(101)	[18]
19		Ti^{3+}-OH	(001)	[20]
20		Ti_{6c}-OH_2	(100)	[17]
21	3715	isolated OH's	(100)/(010)	[19]
22		isolated OH's	(001)	[21]
23	3720	free surface OH's		[23]
24	3730	terminal OH's	(101)	[18]
25	3735	free surface OH's		[23]
26	3738	Ti^{3+}-OH	(101)	[20]
27	3730-3742	Ti_{5c}-OH	(001)	[17]
28	3740	Si-OH impurity		[23]

3.2 Results and Discussion:

Unlike Silica, titania is a crystalline system which undergoes morphological changes such as phase transitions[24–26] as well as atomic changes such as reduction and oxidation of cations and anions upon thermal treatment[27,28]. Our initial goal was to ensure that no phase transition should occur in order to ensure the presence of anatase phase in our support regardless of dehydroxylation temperature since anatase is the most photoactive catalyst.[29–34] To achieve this, commercial TiO_2 anatase nanopoowder (Alfa aesar, 12 nm average particle size, 123 m^2/g) was subjected to calcination at 450°C under air to remove surface organic contaminants (if any) but also assures crystallinity of TiO_2 nanoparticles. The nanopowder while still hot was transferred under inert atmosphere in a quartz reactor and was dehydroxylated at 200°C, 500°C and 700°C under dynamic UHV. The white solid at the end of dehydroxylation was moved into glove box to avoid adsorption of water.

3.2.1 Phase identification, crystallite size, surface area, crystal facets and crystallinity

Sample preparation for XRD was done under air at room temperature for all samples since adsorption of molecular H_2O will not affect the crystallinity of TiO_2 anatase. N_2 adsorption/desorption technique was used to measure the pore size and surface area where as the crystallite diameter was measured using the scherrer formula. Table 3.3 illustrates the pore size, surface area, crystallite size and XRD pattern of TiO_2 at room temperature and TiO_2 dehydroxylated at 200°C, 500°C and 700°C.

Table 3.3 Average crystallite diameters and surface areas calculated from adsorption and desorption branches anatase TiO_2 calcined at 450°C under air for 3h and dehydroxylated under UHV at 200°C, 500°C and 700°C for 12h.

Dehydroxylation temperature	*Sample*	*Phase*	*Crystallite diameter[b]*	*Surface area (m^2/g)*
r.t.[a]	r.t.	Anatase	12 nm	123
200°C	$TiO_{2(200)}$	Anatase	15 nm	110
500°C	$TiO_{2(500)}$	Anatase	16 nm	111
700°C	$TiO_{2(700)}$	Anatase	21 nm	53

a: Commercial TiO_2 anatase was subjected to N_2 adsorption/desorption without any pre-treatment
b: Crystallite diameter calculated using the Scherrer formula

Increasing the temperature for dehydroxylation, the surface area decreases while the pore size increases. This is in agreement with Joseph *et. al.*[35] where agglomeration of small grains takes place to form big crystals which changes the porosity from intercrystallite pores to interagglomerate pores as shown in Figure 3.3. Therefore, one can expect the terminal or bridging hydroxyls and chemisorbed water on the surface of TiO_2 undergoing dehydration to form such agglomerates.

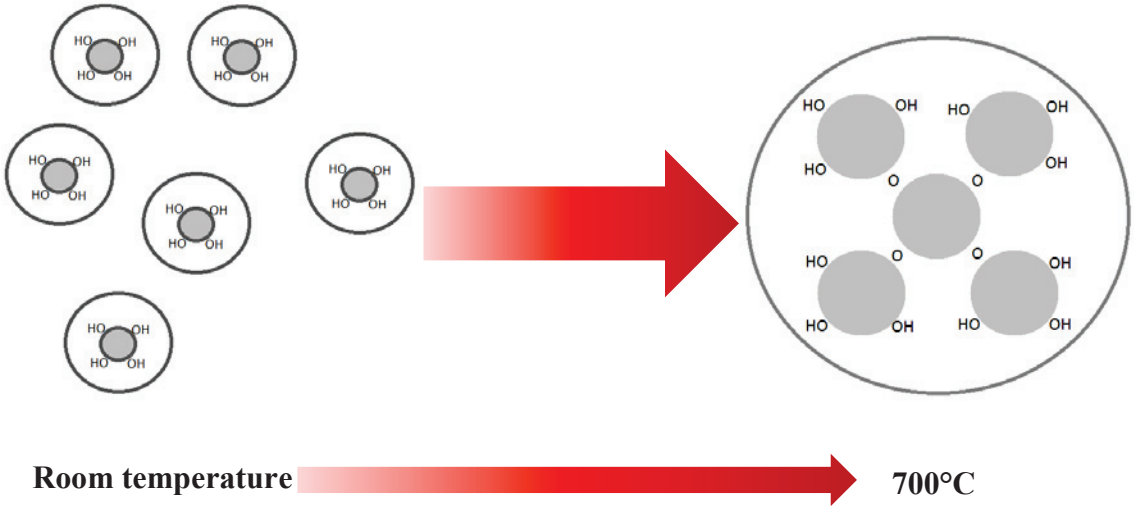

Figure 3.3 Pictorial representation of agglomeration of TiO_2 nanoparticles.

High resolution transmission electron microscopy (HRTEM) was used to identify the facets present in $TiO_{2(700)}$. As seen from Figure 3.4, atomic plane with a lattice spacing of 0.352 nm was obtained which corresponds to (101) plane. This confirms the presence of (101) facets on $TiO_{2(700)}$.

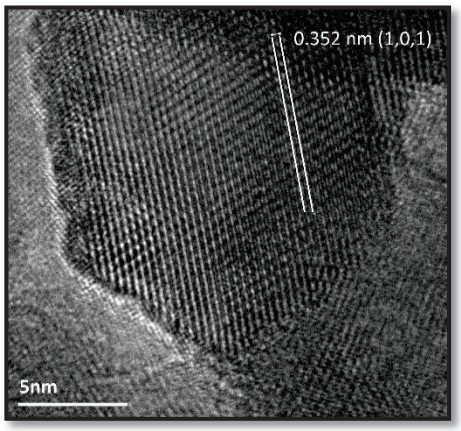

Figure 3.4 HRTEM image of $TiO_{2(700)}$ calcined at 450°C for 3h and dehydroxylated at 700°C for 12h.

For TiO_2 anatase, the order of average surface energies (γ) is $\gamma_{\{111\}}$ (1.61 J m^{-2}) > $\gamma_{\{110\}}$ (1.09 J m^{-2}) > $\gamma_{\{001\}}$ (0.90 J m^{-2}) > $\gamma_{\{010\}}$ (0.53 J m^{-2}) > $\gamma_{\{101\}}$ (0.44 J m^{-2}).[36,37] Surfaces with high energies often decrease rapidly during the crystal growth process so as to reduce the surface energy. This phenomena has been studied first principle calculations and experimental techniques.[38] According to the Wulff construction[17] (Figure 3.5), the relaxed shape of an anatase TiO_2 crystal can be theoretically constructed as a slightly

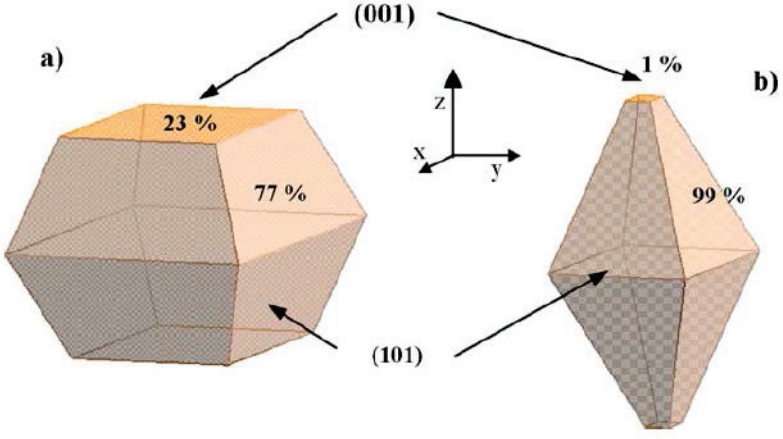

Figure 3.5 Gibbs–Curie–Wulff morphologies of anatase–TiO_2 nanocrystallites based on energy values: (a) before relaxation and (b) after relaxation.[17]

truncated tetragonal bipyramid enclosed by eight equivalent (101) facets on the lateral

surfaces and two equivalent (001) facets on the top/bottom surfaces. Concerning the unrelaxed state, it was observed that 77% of the crystal surface was (101) whereas 23% was (001). Therefore, the contribution of (001) reduces from 23% to 1%[17] or 6%.[16] Thus, a predominance of (101) facet can be expected during the heat treatment and crystal growth process.

XRD used to understand the crystal phases showed (Figure 3.6) peaks positioned at (101), (004), (200), (105), (211) and (204) corresponding to anatase crystal planes and

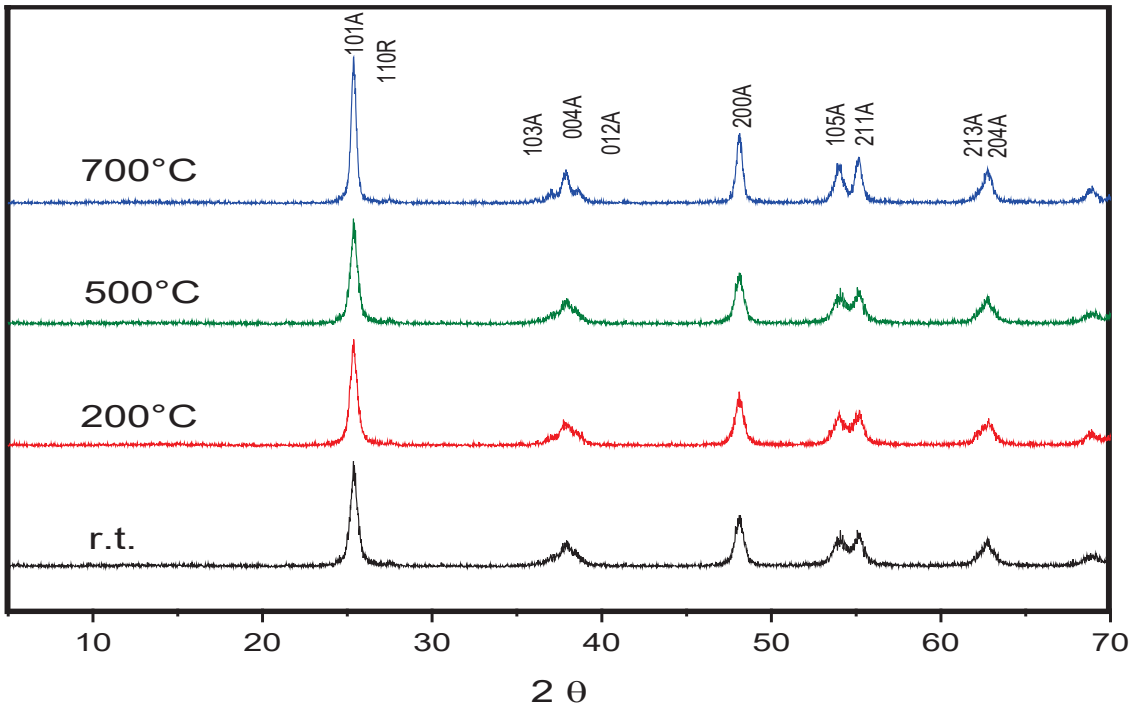

Figure 3.6 X-ray diffraction patterns of anatase TiO_2 at room temperature (r.t.), calcined at 450°C under air for 3h and dehydroxylated under UHV at 200°C, 500°C and 700°C for 12h respectively.

at (110) for rutile crystal planes are in good agreement with crystallographic data for anatase phase (JCPDS 21-1272) and rutile phase (JCPDS 21-1276). Semi-quantitative measurements suggests a low percentage of rutile present (**3±0.5%**) in otherwise anatase crystallites. Change in dehydroxylation temperatures causes no evident change in the concentration of anatase and rutile phases. This is related to the size of the crystallites formed by agglomeration.

H. Zhang and J. F. Banfield[10] showed a relation between size dependency and transformation sequence between the three titania polymorphs (anatase, rutile and brookite). The three polymorphs are sufficiently close in their energies and can be

reversed by small differences in surface energy. Since, the crystal sizes may differ depending on the method of preparation, it can alter the transformation process. Therefore, even at high temperature the anatase phase (in our case) is fairly stable. Increasing the temperature leads to sharper and more intense diffraction lines in XRD revealing a higher degree of crystallinity.

3.2.2 Qualitative analysis of surface species on TiO_2 anatase

Once dehydroxylated, the solid was then characterized using DRIFT spectroscopy. Dehydroxylayted samples were introduced into a cell equipped with a CaF_2 window inside the glove box. The spectra was recorded at room temperature. Figure 3.7a and 3.7b shows the IR absorption spectra of TiO_2 anatase at room temperature and dehydroxylated at 200°C, 500°C and 700°C under UHV after calcination at 450°C respectively. At room temperature (figure 3.7a), a broad peak between 1600-1650 cm^{-1} corresponds to δ_{OH} bending mode due to the presence of physisorbed water. A broad

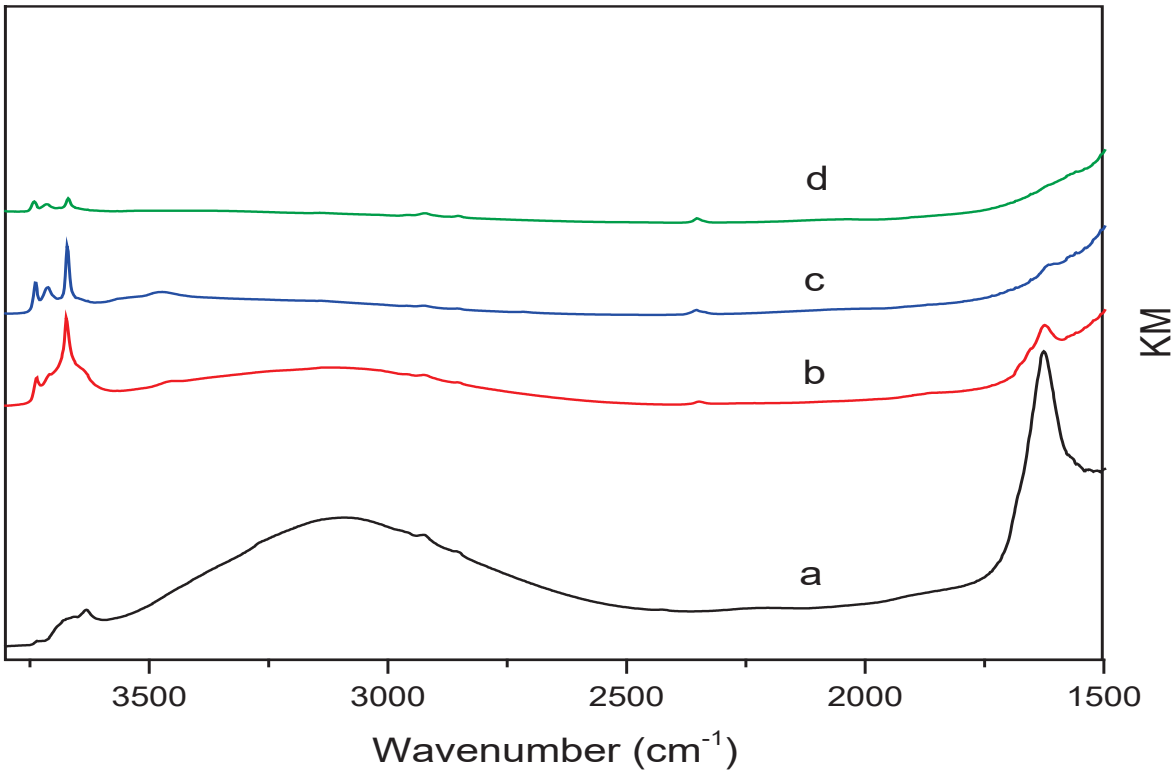

Figure 3.7a DRIFT spectra between 1500-3800 cm^{-1} for TiO_2 anatase at a) room temperature and after calcining at 450°C for 3h under air and dehydroxylating at b) 200°C, c) 500°C and d) 700°C for 12h under UHV respectively.

peak stretching from 2500-3800 cm^{-1} is due to the ν_{OH} stretching indicating the

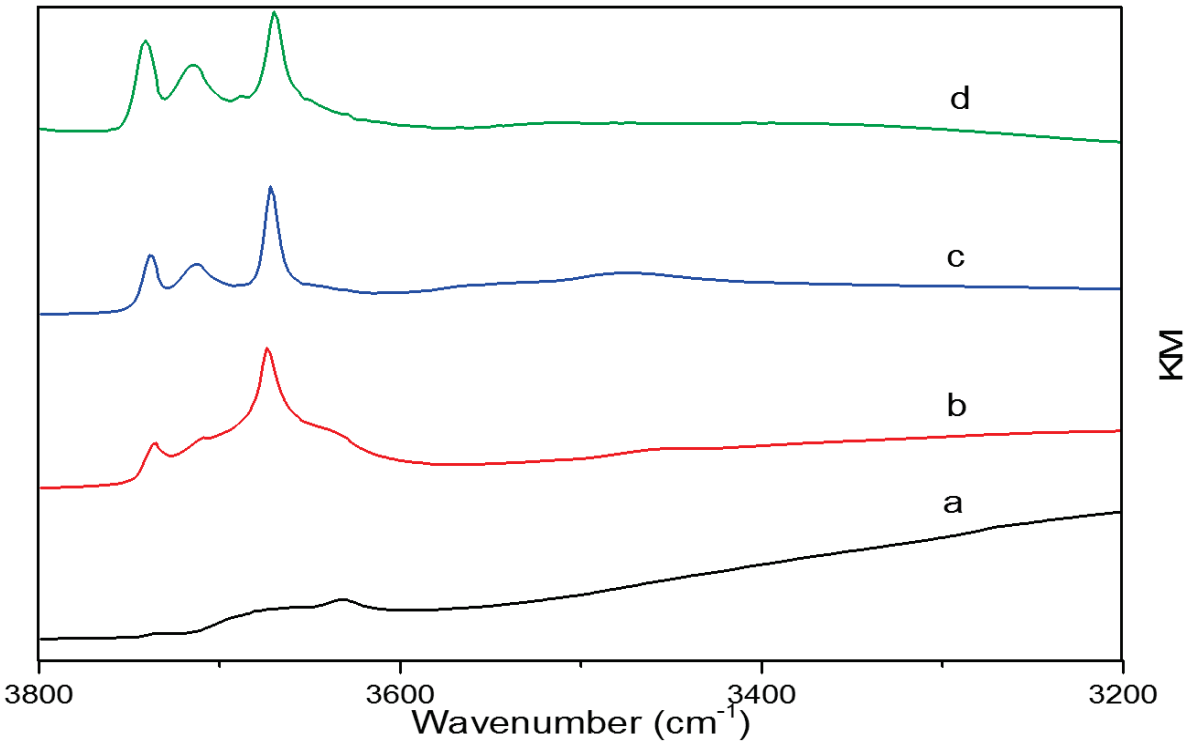

Figure 3.7b DRIFT spectra between 3200-3800 cm^{-1} for TiO_2 anatase at a) room temperature and after calcining at 450°C for 3h under air and dehydroxylating at b) 200°C, c) 500°C and d) 700°C for 12h under UHV respectively.

presence of water and hydroxyl groups associated with each other via H-bonding on surface of TiO_2.[39] Aside from this, peaks at 2850, 2920 and 2960 cm^{-1} relates to νC-H stretching that occurs due to presence of traces of hydrocarbon impurities since TiO_2 almost always contains impurities.[40] For TiO_2 anatase dehydroxylated at 200°C, the concentration of surface adsorbed water is decreased as seen from figure 3.7b. This is due to the removal of physisorbed layer that was H-bonded with the chemisorbed layer. Apart from this, a new peak appears at 2350 cm^{-1} which corresponds to asymmetric νCO_2 stretching. This may be due to the background artifact in IR spectra and can be either positive or negative due to incomplete subtraction of background signal. The overall spectrum was affected by the intense absorption of the TiO_2 support due to the presence of defect sites in the band gap.[41] These sites upon absorption of light promotes electrons in the conduction band. On the contrary, radiation in the IR region induces small thermal excitations that promotes electrons which are close to the conduction band. Thus, a high density of these sites generates a continuum of electronic excitations and affecting the infrared spectra. Therefore, to have a clear picture of different peaks the infrared spectra's were integrated using peak integration method in ORIGIN.

At 500°C, the broad peak in 3000-3400 cm^{-1} disappears and a weak peak appears at 3473 cm^{-1} as shown in figure. This peak is attributed to presence of trace amounts of molecular water.[19] Since, dehydroxylation at 500°C still contains adsorbed H_2O, heat treatment at higher temperatures is necessary to remove the traces of molecular water and get access to the Lewis acidity of TiO_2 surface.

TiO_2 anatase when dehydroxylated at 700°C ($TiO_{2(700)}$) for 12h under UHV, agglomerates forming particles with bigger particles size and lower surface area. As seen in figure, the primitive bands present in the starting material in 2850-2960 cm^{-1} region were still present. Dehydroxylating at such high temperatures, eradicates the presence of chemisorbed water on anatase (001) as the surface morphology supports hydroxyls rather than water. In 3600-3800 cm^{-1} range, 3 different peaks originate at 3670 cm^{-1}, 3715 cm^{-1} and 3741 cm^{-1} which corresponds to different hydroxyl species on TiO_2 anatase surface.

As reported in the introduction (Table 3.2), Finnie *et. al*.[18] assigned the sharp peak at 3670 cm^{-1} to the bridging hydroxyls of $(Ti^{4+})_2$−OH on anatase (101). The intensity of these hydroxyls is not affected by adsorption of H_2O indicating that the bridging hydroxyls do not interact with water molecules via hydrogen bonding. Huang *et. al.*[20] reported a IR spectra with peak at 3715 cm^{-1} ascribed to Ti^{3+}−OH positioned at the (001) planes of TiO_2 anatase. They justified this by the presence of Ti^{3+} signals present in their EPR spectra. Tanaka *et. al.*[19] reported the presence of chemisorbed water on (100) facet might form a pair of stretching bands at 3495 cm^{-1} and 3694 cm^{-1}. Although, there was no mention about the coordination number or the oxidation state of Ti atoms and so we cannot relate them to our results. Additionally, since the signals corresponding to Ti^{3+} signals are absent in the EPR spectra (see later Figure 3.9) and given the fact that the peak in the FTIR is broad (as opposed to expected sharp peak for well-defined hydroxyls) we suspect this mode to be due to water molecule coordinated to a Ti_{6c}^{4+} on (100) plane of TiO_2 anatase.[17] Similarly, the peak at 3741 cm^{-1} is assigned to hydroxyls coordinated to Ti_{5c}^{4+} present on the (001) plane.[42] The presence of Si-OH as an impurity with such an intense peak was ruled out since the purity of sample is 99.97%. It is important to note that TiO_2 is a complex system and thus the hydroxyls determined via DRIFT may or may not be the only hydroxyls present on the surface.[20] Therefore, what we can conclude is the definitive presence of a terminal hydroxyl on (001), a bridging hydroxyl on (101) and a chemisorbed H_2O on

(100) based on experimental values while the absence of other hydroxyls on different facets of anatase cannot be assured.

3.2.3 Quantitative analysis of surface hydroxyls on TiO_2 anatase

TiO_2 anatase has been thoroughly investigated in literature in terms of availability of different hydroxyl/water species present on its surface.[43,44,22] However, very less reports are present on quantification of these hydroxyl species where the solid is dehydroxylated at high temperature.[45,46] Furthermore, quantification of surface hydroxyls is necessary to develop a well-defined catalyst *via* SOMC. Therefore, we decided to estimate the concentration of surface hydroxyls on $TiO_{2(700)}$ using i) infrared spectroscopy and ii) chemical titration method.

i) By infrared spectroscopy

Infrared spectroscopy uses the theory of Beer-Lambert law to deduce a relationship between absorbance ratio and concentration of target species.[47] Usually, a solid pellet (of known weight and diameter) is made by applying high pressure from the sample under examination. When the infrared beam is transmitted, a peak is generated due to molecular vibrational frequency of different moieties in the support. The area under the curve for this peak/s is then employed to obtain the concentration of the desired species.

A quantitative estimation of surface hydroxyls on $TiO_{2(700)}$ was carried out using similar technique.[48] FTIR instrument was calibrated with MCM-41 dehydroxylated at 500°C where a hydroxyl density of 1.4 OH/nm^2 or 2.32 mmol OH/g was known.[49] A linear relation between the amount of OH and the area of the peak was obtained:

$$Q(\text{mmol}) = 0.0023 \text{ X } S \text{ (a.u.)} \quad \text{..... } \textbf{(Eq. 3.1)}$$

where, Q: concentration of hydroxyl in mmol

S: area under the curve

As shown in Figure 3.8, a linear relationship similar to that of MCM-41 was obtained by plotting the concentration of different hydroxyls on $TiO_{2(700)}$ vs area obtained by integrating different peaks. Since, a linear relationship is obtained for both the studies,

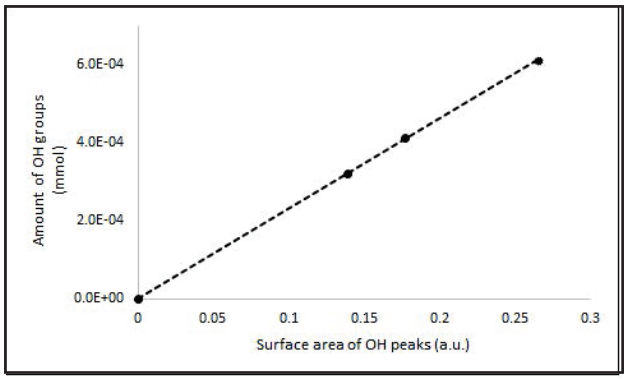

Figure 3.8 Plot showing concentration of hydroxyls (mmol) vs area obtained from integrating different peaks in FTIR spectra.

Eq 3.1 can be also applied to determine the concentration of titanols on $TiO_{2(700)}$. To ensure that the extinction coefficient did not vary drastically, density function theory (DFT) was peerformed using models of the three moeties under examination (**Annex I**).

To quantify titanols, a pellet (25 mg) of $TiO_{2(700)}$ was exposed to infrared beam. The resultant ν(OH's) region consisted of peaks at 3670 cm^{-1}, 3715 cm^{-1} and 3741 cm^{-1} which when integrated gave an area of 0.2653, 0.1770 and 0.1390 respectively. Using Eq. 3.1, the peaks at 3670 cm^{-1}, 3715 cm^{-1} and 3741 cm^{-1} corresponded to 0.024 mmol OH/g (0.27 OH/nm^2), 0.016 mmol OH/g (0.18 OH/nm^2) and 0.012 mmol OH/g (0.14 OH/nm^2) respectively. Since, the peak at 3715 cm^{-1} was considered a coordinated water on (100) crystal plane, the resultant of OH stretching band generated in FTIR was multiplied by 2. Doing so, gave us the concentration of coordinated water as 0.032 mmol OH/g (0.36 OH/nm^2). The sum of these concentrations i.e. 0.068 mmol OH/g or ~0.8 OH/nm^2 was the net quantity of titanols obtained on the surface of $TiO_{2(700)}$. To further estimate the accuracy of the above obtained quantification chemical titration method was used to assess the concentration of titanols.

ii) By chemical titration method

On inorganic oxides other than titania such as silica; silanols have been chemically titrated by reaction of n-*Bu*Li and quantification of butane released (see Eq.3.2).[50]

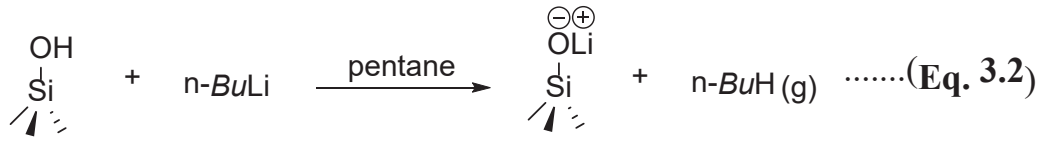

.....(**Eq. 3.2**)

Reagents such as MeMgBr, triisobutyl aluminium etc. has been also utilized as titrating agents to quantify the surface hydroxyls onto solid support.[51] The method involves quantitative reaction of n-*Bu*Li with surface hydroxyls/chemisorbed water on $TiO_{2(700)}$ to yield butane (see Eq. 3.3, 3.4, 3.5) which can then be quantified by GC. We applied such titration method to the dehydroxylated titania discussed above, $TiO_{2(700)}$. The titration was performed on $TiO_{2(700)}$ that is calcined at 450°C and dehydroxylated at

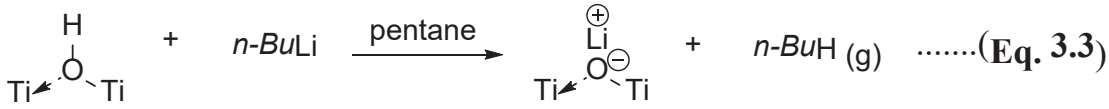

.....(**Eq. 3.3**)

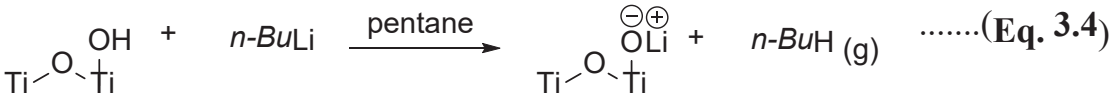

.....(**Eq. 3.4**)

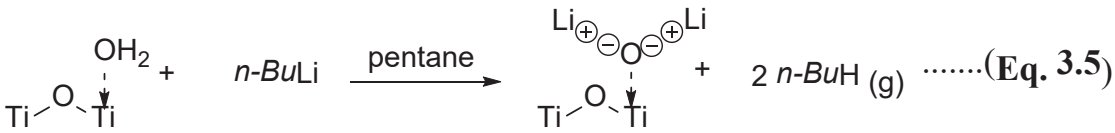

.....(**Eq. 3.5**)

700°C. An excess of n-*Bu*Li was added to dry pentane containing $TiO_{2(700)}$ (ca. 500mg).

0.064 mmol of *Bu*H/g of $TiO_{2(700)}$ was released during the reaction (as determined by GC) that corresponded to 0.73 OH/nm^2 or 0.064 mmol OH/g of titanols present on $TiO_{2(700)}$. An error of 10% was determined between the two experimental procedures. The error lies between the error bars since the concentration of the wanted species is so low. Furthermore, since only 1g of TiO_2 anatase can be calcined and dehydroxylated at a time, different batches were used to perform these experiments. Therefore, a slight variation in the concentration can be expected.

In conclusion, about 0.064 mmol OH/g of dehydroxylated support was estimated along with the nature of titanols and their position on surface of anatase using DRIFT, FTIR and chemical titration methods.

3.2.4 Analysis of surface and bulk magnetic properties *via* EPR spectroscopy

EPR spectroscopy was performed to identify the presence of "Ti^{3+}" ions and anionic vacancies if any, present on the surface or in the bulk of TiO_2 anatase desorbed at 700°C. A known quantity of $TiO_{2(700)}$ was transferred into EPR cell inside the glove box and the cell was capped to ensure there is no leak. The spectra was recorded at 120K in an outgassed chamber. As shown in Figure 3.9, a simulation was run based on the original experiment to acquire precise g values. Nuclear spins with 35%, 25% and 40% spins were obtained corresponding to g values with g_1 = 2.000, g_2 = 1.974 and g_3 = 1.996 respectively. A net total of 21 µmol spins/g of $TiO_{2(700)}$ were calculated form the EPR spectra amongst which 13.7 µmol spins/g belongs to "Ti^{3+}" ions.

Signal at g_1 = 2.000 was identified as the oxygen vacancies created in the bulk of titania or super oxides created on the surface due to thermal treatment under vacuum (F-centers).[52,53,54,55] The Ti_{5c}–O_{2c} bond on the relaxed surface (~1.83 Å) is much shorter

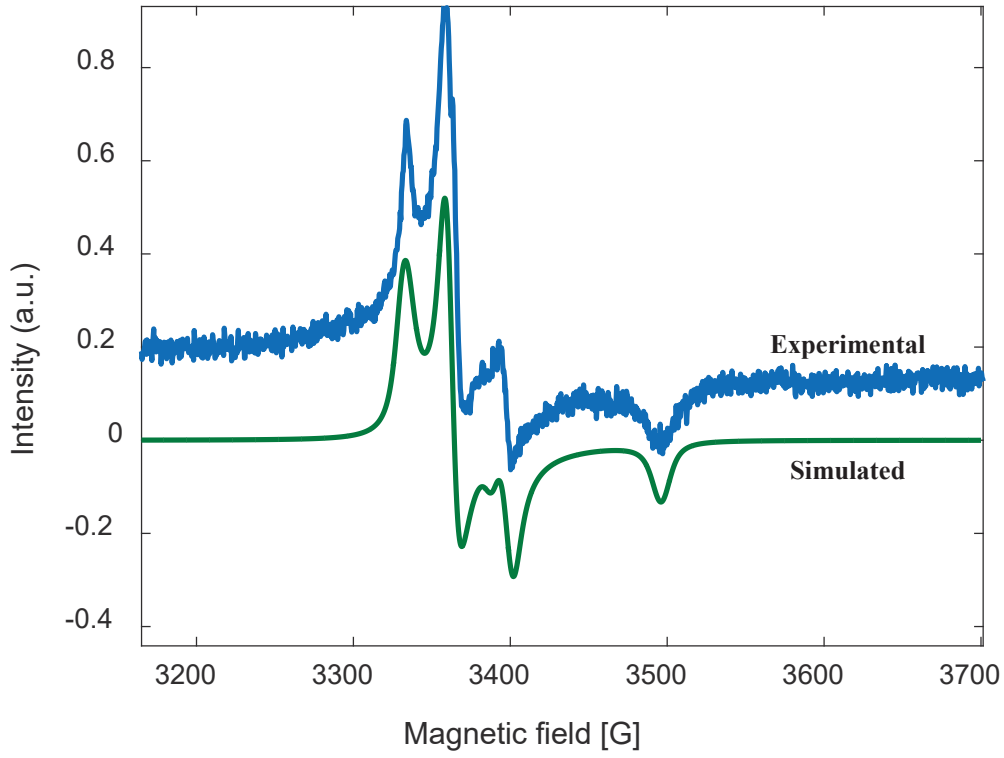

Figure 3.9 Experimental and simulated EPR spectra of TiO_2 anatase calcined at 450°C for 3h and dehydroxylated at 700°C for 12h.

than that on the bulk-terminated one (~2.00 Å) and therefore the stiffness of this bond is why oxygen vacancies are generally present in the subsurface or bulk rather than the

surface of (101).[56] Since, (101) is the predominant crystal plane on $TiO_{2(700)}$ most of the oxygen vacancies are expected in the bulk except few that are present on (001) or (100) facets. These free electrons on the surface of titania may act as reduction sites and can create irregularities while executing surface chemistry. The magnetic activity at $g_2 = 1.974$ and $g_3 = 1.996$ was related to the isolated "Ti^{3+}" centres present in the bulk.[57,58] This further proves that the broad peak at 3715 cm^{-1} in the DRIFT is related to a water molecule coordinated to a hexa- coordinated Ti^{4+} on (100) plane of TiO_2 anatase and not to Ti^{3+}–OH positioned at the (001) plane of TiO_2 anatase since the "Ti^{3+}" ions are absent on the surface of titania.

3.3 Different commercial TiO_2

Titanium dioxide (anatase) from other commercial sources such as Sigma Aldrich (**SA**) and Nanoarc™ (**NA**) were also implemented to the same heat treatment as that of titania from Alfa aesar. The aim behind was to achieve a cleaner hydroxyl free surface to get access to lewis acidic nano sites on the surface of titania while still being in the anatase regime.

TiO_2 anatase nano powder from SA and NA was calcined at 450°C under air and then dehydroxylated at 700°C under UHV; similar treatment like TiO_2 anatase from Alfa Aesar. Once, dehydroxylated the solids were characterized using DRIFT spectroscopy and XRD to understand the surface species (if any) and the crystallinity respectively.

The DRIFT spectra for dehydroxylated SA and NA solids are shown in Figure 3.10. NA solid (Figure 3.10a) mainly displays a broad peak corresponding to chemisorbed water. In 3600-3800 cm^{-1} region, a weak broad signal was observed which can be ascribed to H-bonded surface hydroxyls. The intensity is very low indicating the near absence of hydroxyls in this sample. In case of SA support (Figure 3.10b), a broad peak at 3500 cm^{-1} and two strong and broad peaks in 3600-3800 cm^{-1} corresponds to water stretching and H-bonded hydroxyl stretching. Thus, we realized that it was difficult to achieve a clean surface using only thermal treatment and we can attain a maxima but not a complete clean surface.N_2 adsorption and desorption experiment yield surface area of the two solid NA and SA to be 13 m^2/g and 18 m^2/g respectively. Such low surface area indicate that the agglomeration of smaller particles lead to

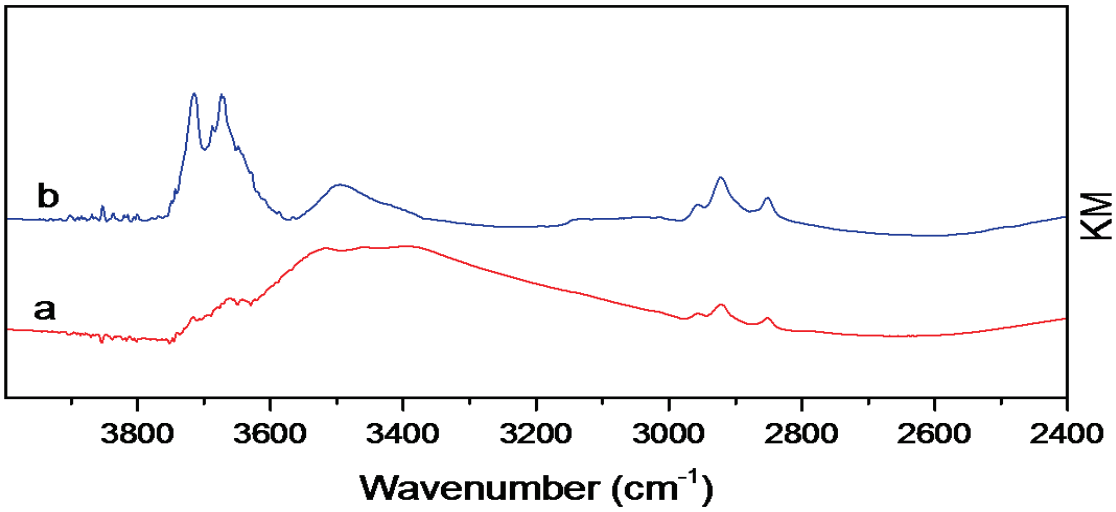

Figure 3.10 DRIFT spectra after calcining at 450°C for 3h under air and dehydroxylating at 700°C for 12h under UHV for TiO_2 a) Nanoarc™ and b) Sigma Aldrich respectively.

formation of larger particles by insitu dehydration. Thus, conversion of anatase to rutile was expected from these samples and XRD was done to confirm these results. XRD spectra shown in Figure 3.11 clearly shows complete conversion to rutile in case of NA TiO_2 and a mix of anatase and rutile crystal phases in case of SA TiO_2. This is related to the crystallite size and agglomeration of particles as discussed previously.

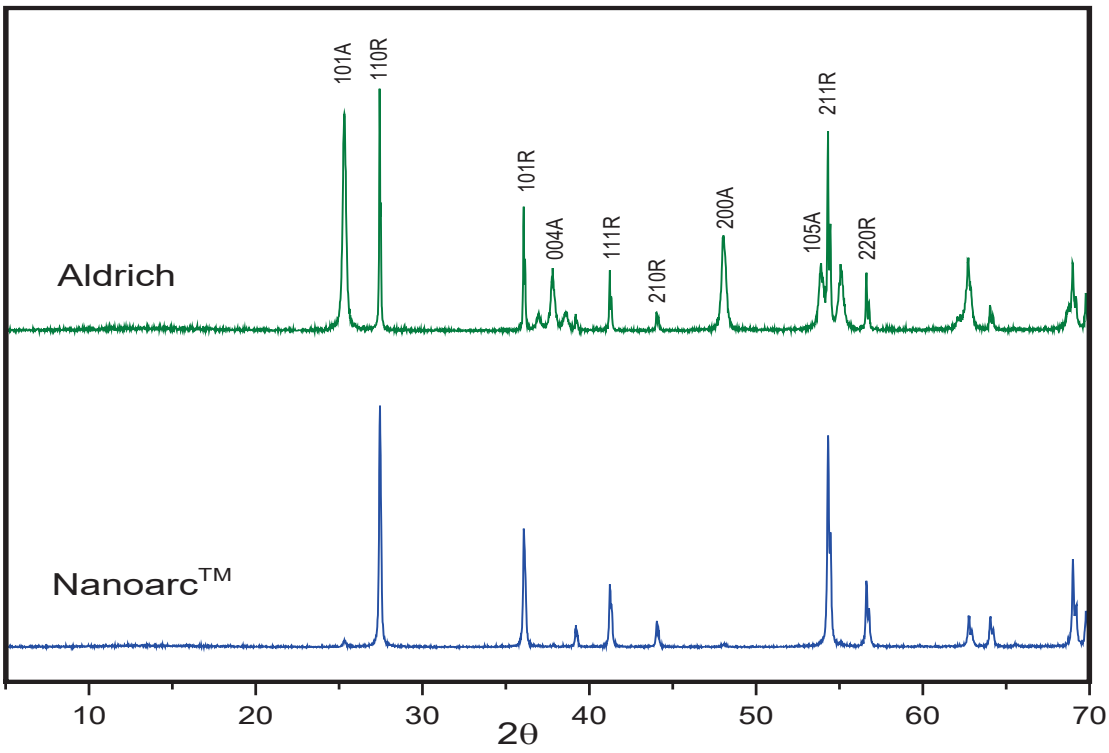

Figure 3.11 X-ray diffraction patterns of TiO_2 from different commercial sellers calcined at 450°C under air for 3h and dehydroxylated under UHV at 700°C for 12h respectively.

The grain size for treated solids as calculated from Scherrer's formula was 64 nm for NA and between 40 and 100 nm for SA solid. Busca *et. al.*[43] reported the differences in surface activity and lewis acidic sites for different anatase preparations. He studied how different preparations led to different surface sites and behaved differently upon thermal treatment. This is what we also observe here with three different commercial TiO_2 powder. Although, we are ambivalent about their preparation procedure we observed conversion of anatase TiO_2 to rutile TiO_2 by thermal etching thus making them impractical for our goal.

3.4 Conclusion

TiO_2 anatase was calcined at 450°C under air and dehydroxylated at 700°C under UHV. The resultant solid was composed of 97% anatase and 3% rutile phase as characterized by semi-quantitative measurements using XRD. Such a treatment led to the agglomeration of smaller anatase crystallites (~ 12 nm) to form bigger crystals (~21 nm) as calculated by Scherrer equation. Particles in the size range of 15-35 nm are known to behave as a better potocatalyst then the particles of lower diameter.[45] This is because in this range the surface concentration of holes [h^+] increases and the [OH] concentration decreases.

XRD and HRTEM identified the existence and predominance of (101) facet. The qualitative analysis of surface species on anatase by DRIFT spectroscopy suggested the presence of mainly 3 species *i.e.* a bridiging hydroxyl on (101), a terminal hydroxyl on (001) and a coordinated water molecule on (100) crystal plane respectively (Figure 3.12). Quantitative analysis using FTIR spectroscopy and chemical tritration generated a value of 0.068 mmol OH/g or 0.8 OH/nm^2 and 0.064 mmol OH/g or 0.7 OH/nm^2 respectively. A 10% error margin between the 2 values suggested accuracy of the hydroxyls concentration. These analyses confirms that the surface is partially dehydroxylated and also contains accessible lewis acidic (Ti_{5c}) sites. Furthermore, EPR spectroscopy indicated the presence of oxygen vacancies and "Ti^{3+}" ions (13.7 µmol Ti^{3+}/g) are mainly in the bulk of the system and therefore has no influence on the surface characteristics of the system. This corresponds to the fact that all the Ti atoms on the surface are in +4 oxidation state and cannot act as a reductant.

Thus, a well-defined correlation between the nature and concentration of different surface species was established. These analyses sheds light on the complexity of this system (TiO_2 anatase) comprising of surface hydroxyls, coordinated water, lewis acidic sites, weak bronsted basic sites and anionic vacancies.

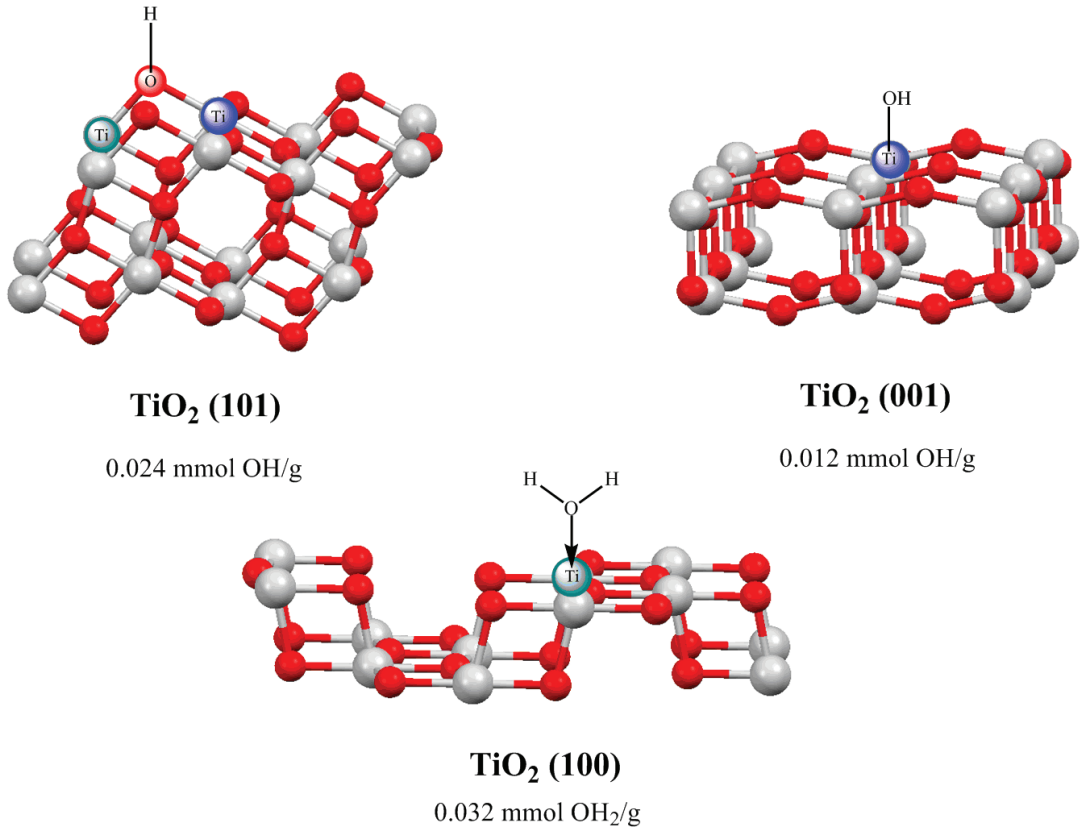

Figure 3.12 Schematic representation of the anatase crystal facets a) (101) with a bridging hydroxyl group, b) (001) with a terminal group and c) (100) with a chemisorbed H_2O on the surface.

3.5 References

(1) Roy, P.; Berger, S.; Schmuki, P. *Angew. Chemie - Int. Ed.* **2011**, *50* (13), 2904–2939.

(2) Chen, X.; Mao, S. S. *Chem. Rev.* **2007**, *107* (7), 2891–2959.

(3) Grätzel, M. *Nature* **2001**, *414* (6861), 338–344.

(4) Linsebigler, A. L.; Lu, G.; Yates, J. T. *Chem. Rev.* **1995**, *95* (3), 735–758.

(5) L. Kavan; M. Grätzel; S. E. Gilbert; C. Klemenz, and; Scheel, H. J. *J. Am. Chem. Soc.* **1996**, *118* (28), pp 6716–6723.

(6) Fujishima, A.; Zhang, X.; Tryk, D. A. *Surf. Sci. Rep.* **2008**, *63* (12), 515–582.

(7) Luttrell, T.; Halpegamage, S.; Tao, J.; Kramer, A.; Sutter, E.; Batzill, M. *Sci. Rep.* **2015**, *4* (1), 4043.

(8) Kumar, S. G.; Devi, L. G. *J. Phys. Chem. A* **2011**, *115* (46), 13211–13241.

(9) Liu, G.; Wang, L.; Yang, H. G.; Cheng, H.-M.; Qing, G.; Lu, M. **2009**, *20*, 831–843.

(10) Zhang, H.; Banfield, J. F. *J. Phys. Chem. B* **2000**, *104* (15), 3481–3487.

(11) Xu, A.-W.; Gao, Y.; Liu, H.-Q. *J. Catal.* **2002**, *207* (2), 151–157.

(12) Burnside, S. D.; Shklover, V.; Barbé, C.; Comte, P.; Arendse, F.; Brooks, K.; Grä, M. *Chem. Mater.* **1998**, *10* (9), pp 2419-2425.

(13) Gao, Y.; Elder, S. . *Mater. Lett.* **2000**, *44* (3–4), 228–232.

(14) Chemseddine, A.; Moritz, T. *Eur. J. Inorg. Chem.* **1999**, *1999* (2), 235–245.

(15) Diebold, U.; Ruzycki, N.; Herman, G. S.; Selloni, A. *Catal. Today* **2003**, *85* (2–4), 93–100.

(16) Lazzeri, M.; Vittadini, A.; Selloni, A. *Phys. Rev. B - Condens. Matter Mater. Phys.* **2001**, *63* (15), 1554091–1554099.

(17) Arrouvel, C.; Digne, M.; Breysse, M.; Toulhoat, H.; Raybaud, P. *J. Catal.* **2004**, *222* (1), 152–166.

(18) Finnie, K. S.; Cassidy, D. J.; Bartlett, J. R.; Woolfrey, J. L. *Langmuir* **2001**, *17* (3), pp 816–820.

(19) Tanaka, K.; White, J. M. *J. Phys. Chem.* **1982**, *86* (1971), 4708–4714.

(20) Huang, H.; Lin, J.; Fan, L.; Wang, X.; Fu, X.; Long, J. *J. Phys. Chem. C* **2015**, *119* (19), 10478–10492.

(21) Primet, M.; Pichat, P.; Mathieu, M.-V. *J.Phys.Chem.C* **1971**, *75* (1216–1220).

(22) Soria, J.; Sanz, J.; Sobrados, I.; Coronado, J. M.; Hernández-Alonso, M. D.; Fresno, F. *J. Phys. Chem. C* **2010**, *114* (39), 16534–16540.

(23) Hadjiivanov, K.; Klissurski, D.; Busca, G.; Lorenzelli, V. *J. CHEM. SOC. FARADAY TRANS* **1991**, *87* (1), 175–178.

(24) Arbiol, J.; Cerdà, J.; Dezanneau, G.; Cirera, A.; Peiró, F.; Cornet, A.; Morante, J. R. *J. Appl. Phys.* **2002**, *92* (2), 853–861.

(25) Gao, Y. *Thin Solid Films* **1999**, *346* (1–2), 73–81.

(26) D. Mardare, P. H. *Mater. Sci. Eng. B* **1999**, *68* (1), 42–47.

(27) Carter, E.; Carley, A. F.; Murphy, D. M. *J. Phys. Chem.* **2007**, *111*, 10630–10638.

(28) Xiong, L. Bin; Li, J. L.; Yang, B.; Yu, Y. *J. Nanomater.* **2012**, *2012*, 1–13.

(29) J. Jitputtia,S. Pavasupree, Y. Suzuki, S. Y. *J. Solid State Chem.* **2007**, *180* (5), 1743–1749.

(30) G. L. Chiarello, E. Selli, L. F. *Appl. Catal. B Environ.* **2008**, *84* (1–2), 332–339.

(31) Karakitsou, K. E.; Verykios, X. E. *J. Phys. Chem.* **1993**, *97* (6), 1184–1189.

(32) Yan, J.; Wu, G.; Guan, N.; Li, L.; Li, Z.; Cao, X. *Phys. Chem. Chem. Phys.* **2013**, *15* (26).

(33) Luttrell, T.; Halpegamage, S.; Tao, J.; Kramer, A.; Sutter, E.; Batzill, M. *Sci. Rep.* **2014**, *4*, 4043.

(34) Zhang, J.; Zhou, P.; Liu, J.; Yu, J. *Phys. Chem. Chem. Phys.* **2014**, *16* (16), 20382–20386.

(35) Joseph, K.; Raj, A.; Viswanathan, B. *Indian J. Chem.* **2009**, *48*, 1378–1382.

(36) Xu, H.; Reunchan, P.; Ouyang, S.; Tong, H.; Umezawa, N.; Kako, T.; Ye, J. *Chem. Mater.* **2013**, *25* (3), 405–411.

(37) Liu, M.; Piao, L.; Zhao, L.; Ju, S.; Yan, Z.; He, T.; Zhou, C.; Wang, W. *Chem. Commun.* **2010**, *46*, pp 1664-1666.

(38) Yang, H. G.; Sun, C. H.; Zhang Qiao, S.; Zou, J.; Liu, G.; Smith, S. C.; Cheng, H. M.; Gao, &; Lu, Q. *Nat.* **2008**, *453*, pp 638-641.

(39) Martra, G. *Appl. Catal. A Gen.* **2000**, *200* (1–2), 275–285.

(40) Setvín, M.; Daniel, B.; Mansfeldova, V.; Kavan, L.; Scheiber, P.; Fidler, M.; Schmid, M.; Diebold, U. *Surf. Sci.* **2014**, *626*, 61–67.

(41) Berger, T.; Sterrer, M.; Diwald, O.; Kno, E.; Panayotov, D.; Thompson, T. L.; Yates, J. T. *J. Phys. Chem. B* **2005**, *109*, 6061–6068.

(42) Dzwigaj, S.; Arrouvel, C.; Breysse, M.; Geantet, C.; Inoue, S.; Toulhoat, H.; Raybaud, P. *J. Catal.* **2005**, *236* (2), 245–250.

(43) Busca, G.; Saussey, H.; Saur, O.; Lavalley, J. C.; Lorenzelli, V. *Appl. Catal.* **1985**, *14* (C), 245–260.

(44) Morterra, C. *J. Chem. SOC. Faraday Trans. I* **1988**, *84* (5), 1617–1637.

(45) Carneiro, J. T.; Savenije, T. J.; Moulijn, J. A.; Mul, G. *J. Phys. Chem. C* **2010**, *114* (1), pp 327–332.

(46) Munuera, G.; Moreno, F.; Prieto, J. A. *Zeitschrift für Phys. Chemie* **1972**, *78* (3_4), 113–117.

(47) Sun, D. Q.; Zhang, L. W.; Zhang, X. L. *Adv. Mater. Res.* **2011**, *287–290*, 953–960.

(48) *Comptes Rendus Chim.* **2004**, *7* (8–9), 725–736.

(49) Fabien Bini; Cécile Rosier; Romain Petroff Saint-Arroman; Eva Neumann; Céline Dablemont; Aimery de Mallmann; Frédéric Lefebvre; Gerald P. Niccolai; Jean-Marie Basset; Mark Crocker, and; Buijink, J.-K. *Organometallics* **2006**, *25* (15), pp 3743–3760.

(50) Larabi, C.; Quadrelli, E. A. *Eur. J. Inorg. Chem.* **2012**, *2012* (18), 3014–3022.

(51) Sato, M.; Kanbayashi, T.; Kobayashi, N.; Shima, Y. *J. Catal.* **1967**, *7*, 342–351.

(52) Sun, Y.; Egawa, T.; Shao, C.; Zhang, L.; Yao, X. *J. Phys. Chem. Solids* **2004**, *65* (11), 1793–1797.

(53) Naccache, C.; Meriaudeau, P.; Che, M.; Tench, A. J. *Trans. Faraday Soc.* **1971**, *67*, 506–512.

(54) Setvin, M.; Franchini, C.; Hao, X.; Schmid, M.; Janotti, A.; Kaltak, M.; Van De Walle, C. G.; Kresse, G.; Diebold, U. *Phys. Rev. Lett.* **2014**, *113* (8), pp 086402(5).

(55) Serwicka, E. *Elsevier Sci. Publ. B.V* **1985**, *13*, 287–293.

(56) Li, Y.-F.; Aschauer, U.; Chen, J.; Selloni, A. *Acc. Chem. Res.* **2014**, *47* (11), 3361–3368.

(57) Kumar, C. P.; Gopal, N. O.; Wang, T. C. **2006**, 5223–5229.

(58) Rajh, T.; Nedeljkovic, J. M.; Chen, L. X.; Poluektov, O.; Thurnauer, M. C. *J. Phys. Chem. B* **1999**, *103* (18), 3515–3519.

(59) Bourikas, K.; Kordulis, C.; Lycourghiotis, A. *Chem. Rev.* **2014**, *114* (19), 9754–9823.

Chapter 4

Grafting Organometallic complex on Titania *via* SOMC

PART I: SOMC by covalent grafting

Chapter 4

Grafting Organometallic complex on Titania *via* SOMC

Part I: SOMC by covalent grafting

Chapter 4

Part I: SOMC by covalent grafting

4.1 Introduction

As discussed in Chapter 1, SOMC on titania has been applied previously using organometallic precursors such as $V(NMe_2)_4$, $Sn(CH_3)_4$, nickelocene etc. as metal source.[1–5] Although well characterized, these studies are incomplete due to the ill-defined surface moieties. The quantitative estimation of surface hydroxyls or coordinated water on TiO_2 and the organics released during the grafting process were not performed. These data are important in identifying the availability of surface moieties and the reactivity of the incoming organometallic precursor.

Amongst many known organometallic precursor, $Ta[CH_2C(CH_3)_3]_3[=CHC(CH_3)_3]$ (**1**) is one of the most well studied substrate for SOMC. Ta chemistry on silica has been well defined, clearly understood and well characterized in literature.[6–9] Dufaud *et. al.*[10] succeeded in grafting tantalum on silica (Aerosol-200) by reacting partially dehydroxylated silica bearing silanol functionalities with $Ta[-CH_2C(CH_3)_3]_3[=CHC(CH_3)_3]$ (**1**). This study followed by other studies[7,8] revealed that changes in the nature and concentration of silanols (by dehydroxylation at different temperatures) can affect the nature surface species. As shown in Figure 4.1, two different types of surface species are formed on silica and the concentration of these species is a function of dehydroxylation temperature of silica.[11] Based on IR spectroscopy, 1D and 2D solid state NMR spectroscopies, elemental analyses and quantitative chemical reactivity toward ethanol and H_2, it has been shown that the

surface complex (≡SiO)Ta[-$CH_2C(CH_3)_3$]$_2$[=$CHC(CH_3)_3$] can be the sole surface species (> 95 %) present on the surface of silica partially dehydroxylated at 700°C.

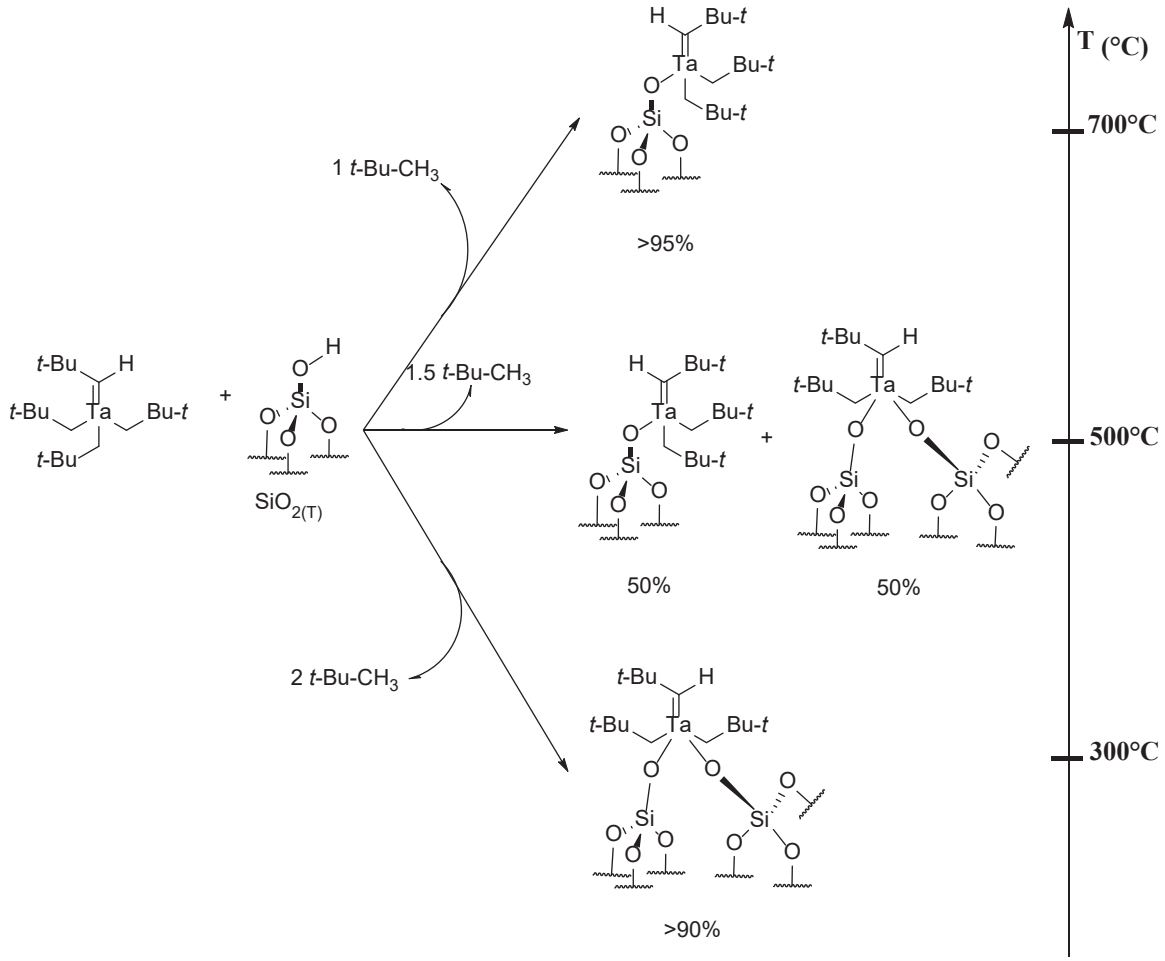

Figure 4.1 Formation of different well-defined Tantala species depending on the dehydroxylation temperature of SiO_2.

Thus, using such a precursor gives us an added advantage to understand its interaction with the active titania surface reactive species. Since we already have a quantitative estimation of surface species on $TiO_{2(700)}$ the next step was to graft complex (**1**) by surface organometallic approach to further understand the environment and chemical accessibility of hydroxyls present on different planes of $TiO_{2(700)}$.

4.2 Results and Discussion

4.2.1 Grafting of Ta complex on $TiO_{2(700)}$

TiO_2 anatase dehydroxylated at 700°C was used as the substrate for grafting complex (**1**). Complex (**1**) was prepared as described in literature.[12] The impregnation technique typically consisted of stirring at 25°C a mixture of $TiO_{2(700)}$ and Ta complex in pentane with the expected reaction as shown in (Eq. 4.1).

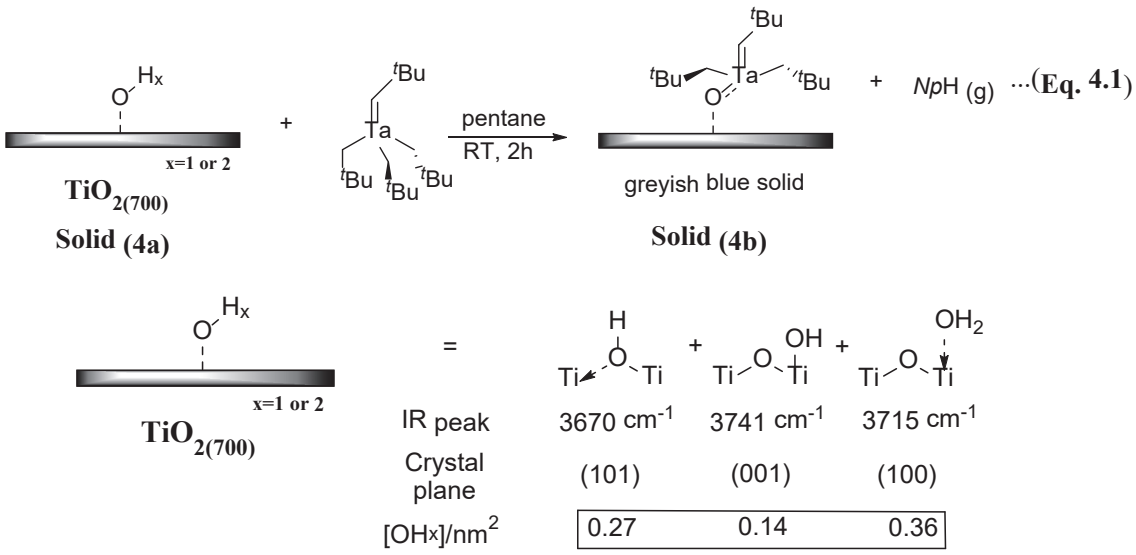

Grafting reaction at low temperature avoids the decomposition of organometallic precursor thus favouring a clean chemistry onto titania. After washing cycles, the volatiles are condensed into a reactor of known volume in order to quantify the neopentane (**NpH**) released during the reaction. The released gas was quantified by gas chromatography. The resultant solid was dried under UHV for an hour to obtain a greyish-blue powder and was characterized by DRIFT, SSNMR and elemental analysis. Furthermore, solid (4b) was taken in a reactor (of known volume) and was exposed to vapours of degassed water (as shown in Eq 4.2). Doing so allowed us to quantify the amount of residual alkanes released due to the reaction between water and

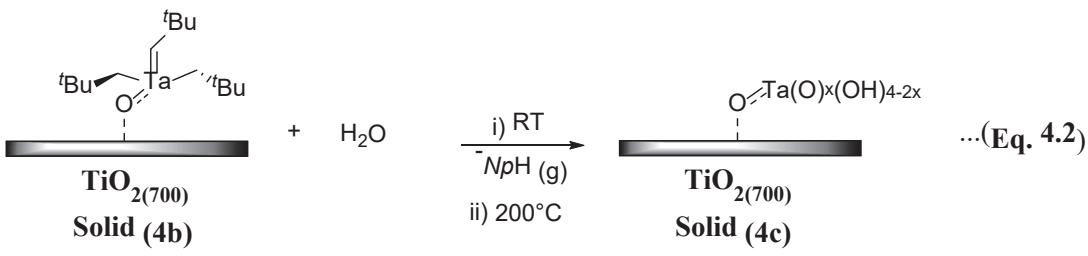

the organic moieties after the grafting procedure. The solid was then dried under UHV for 1h at 200°C (solid (4c)) to remove the physisorbed water and was characterized using DRIFT spectroscopy.

4.2.2 Infrared study and Elemental analysis

Based on chapter 3 results, the reactive surface titanols of $TiO_{2(700)}$ are described as a mixture of three different kind of hydroxyls situated on three different facets of anatase. These three species display three diagnostic sharp peaks in the IR spectra (Figure 4.2a) at 3671 cm^{-1} and 3741 cm^{-1} attributed to a bridging hydroxyl present on

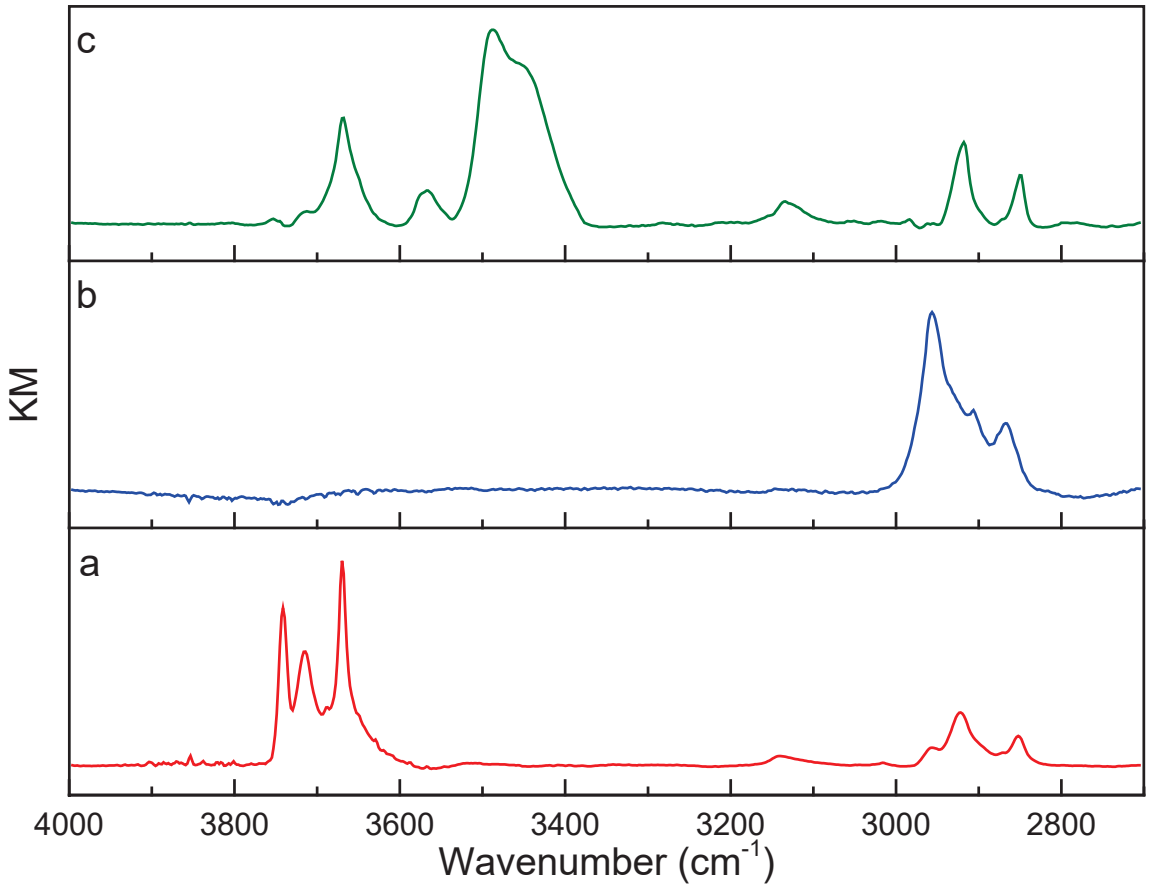

Figure 4.2 DRIFT spectra of TiO_2 anatase a) after dehydroxylating at 700°C under UHV for 12h b) after $Ta[-CH_2C(CH_3)_3]_3[=CHC(CH_3)_3]$ grafting on $TiO_{2(700)}$, solid (**4b**) and c) after exposing solid (**4b**) to water vapours and dehydroxylating at 200°C for 1h, solid (**4c**). For full spectra look **Annex III**.

(101) atomic plane and Ti-OH on a (001) atomic plane respectively. The broad peak at 3715 cm^{-1} corresponds to a coordinated water on a (100) anatase facet. The overall

concentration of all the 3 species combined as estimated by chemical titration is approximately 0.7 OH/nm^2 (Eq. 4.1).

Table 4.1 summarizes all the data for grafting of complex (**1**) on $TiO_{2(700)}$: metal content, neopentane released during the grafting and the equivalent of remaining neopentane per grafted metal determined by quantifying neopentane evolved during total hydrolysis.

Table 4.1 Grafting of complex (**1**) on $TiO_{2(700)}$ by impregnation at 25°C in pentane.

Molecular precursor	*Ta (wt%)[a]*	*C atoms/ Ta*	*NpH/ Ta (grafting)[b]*	*NpH equiv./ Ta (hydrolysis) [c]*
Ta[-CH$_2$C(CH$_3$)$_3$]$_3$[=CHC(CH$_3$)$_3$]	1.5	14	1.0	3.2

a: Percentage of metal (**elemental analysis**)

b: Equivalent of neopentane (NpH) per Ta released during the grafting quantified by GC

c: Equivalent of remaining neopentane per grafted Ta determined by quantifying NpH evolved during total hydrolysis.

It is important to note that about one NpH per Ta is released during the grafting procedure. The metal loading of 1.5 wt% for Ta correspond to 0.12 mmol of metal per gram of solid. The results are in close agreement with concentration of titanols obtained by chemical titration indicating a full reaction of surface hydroxyls with Ta complex. This can also be observed by the DRIFT spectra (Figure 4.2b), where all the peaks corresponding to surface hydroxyls have disappeared indicating their ingestion during the grafting process. Additionally, the instensity of peaks $\nu_{C\text{-}H}$ in the C-H stretching region (2800-3000 cm^{-1}) is enhanced due to the presence of neopentyl and neopentylidene in the solid. A total of 14C/Ta was obtained by elemental analysis suggesting the release of one neopentane molecule/ Ta. The reaction of Ta(V) complex with silica partially dehydroxylated at 700°C mainly provides monosiloxy surface complexes [(≡SiO)Ta(=CH*t*Bu)(CH$_2$*t*Bu)$_2$(≡SiOSi≡)] by eradication of a sigma bonded ligand as NpH.[7,11] Thus, one can expect a similar chemistry on titania; albeit before arriving to any conclusions the Ta grafted titania needs to be well- characterized

like Ta grafted silica to fully understand the nature of covalency between the complex and the surface since anatase in itself consists of different surface species.

Solid (4b) after being well characterized was reacted with vapours of degassed water (Eq. 4.2). This led to release of alkyl chains on Ta as gaseous alkanes which was quantified *via.* GC. The coordination sphere of the resulting species is not well defined, it is probably a mixture of oxo and hydroxo ligands. Indeed, two hydroxo ligands can be easily transformed in one oxo ligand releasing water. A total of 3.2 NpH/Ta atom was obtained during the hydrolysis of solid (4b) making a net mass balance of 4.2 NpH/Ta atom. The resultant powder was then dehydrated at 200°C for 1h to obtain solid (4c).

4.2.3 EPR spectroscopy

The greyish-blue solid was transferred in a quartz tube inside glove box to perform EPR spectroscopy. A signal at approximately g = 1.93 (Figure 4.3) was assigned to "Ti^{3+}" ions.[13,14] Approximately 35 µmol spins/g of $TiO_{2(700)}$ were calculated after the grafting of complex (**1**) onto $TiO_{2(700)}$. It is important to remember that the starting material i.e. $TiO_{2(700)}$ initially consisted low amount of oxygen vacancies and "Ti^{3+}"

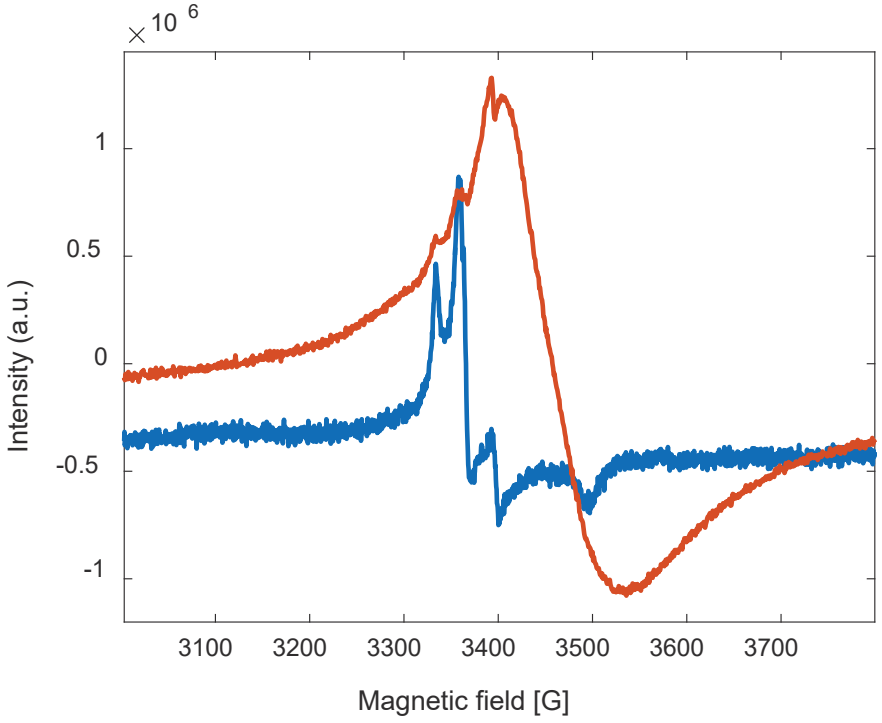

Figure 4.3 EPR spectra of $TiO_{2(700)}$, before (in blue) and after grafting with complex (**1**) i.e. solid (4b) (in orange).

ions (20 µmol spins/g) mainly present in the bulk with a few oxygen vacancies present on the surface. After the grafting process, we see an increase in the paramagnetic activity of the solid from 13.7 µmol"Ti^{3+}"/g to 29 µmol"Ti^{3+}"/g indicating that the organometallic Ta(V) complex plays an important role in inducing surface para magnetic ions since addition of $Ta(OEt)_5$ did not bring any change in the EPR spectra. This suggests the "self-doping" mechanism of TiO_2.[15] It is well known that Tantalum possesses strong oxophilicity.[16,17] Therefore, one can hypothesize an oxygen insertion in the M—C bond of the grafted species leading to the formation of an alkoxide complex and reducing surface Ti^{4+} ions by abstraction of surface oxygen thereby creating "Ti^{3+}" ions. Although, since the increase in the concentration of "Ti^{3+}" ions is so low no experimental evidences of the formation of alkoxides were determined and therefore it is abstract to comment on the technicalities of the observed activity.

4.2.3 Solid State NMR spectroscopy

Roux *et. al.*[7] reported the CPMAS ^{13}C NMR of complex (**1**) grafted on silica that was dehydroxylated at 700°C. 4 different peaks at 31, 47, 95 and 247 ppm corresponding to different carbons of neopentyl and neopentylidene ligands were obtained respectively. No prominent peaks were observed for complex (**1**) grafted on $TiO_{2(700)}$ by CPMAS ^{13}C NMR (**Annex II**). This is due to the presence of defects on the surface and sub-surface of $TiO_{2(700)}$ close to which excess electrons are trapped.[18,19] An unpaired electron has a gyromagnetic ratio that is 658 times larger than that of the proton and has significant interaction with the external magnetic field and the surrounding nuclei.[20]

Thus, it is conclusive that CPMAS ^{13}C NMR does not give any information due to the paramagnetic activity of the solid. On other hand, EPR provided further insight into the paramagnetic centres and their behaviour on the surface of $TiO_{2(700)}$ grafted with complex (**1**).

4.3 Summary

Eq. 4.3, 4.4 and 4.5 depict the reaction of complex (**1**) with individual surface specie present on different crystal planes of $TiO_{2(700)}$. Reaction of complex (**1**) with the

coordinated water (Eq. 4.5) on the (100) crystal plane can be expected to form two different surface species. The DRIFT spectra of solid (4b) (Figure 4.2) shows complete disappearance of all the hydroxyl peaks with no new appearances. This suggests that Ta=O is the major specie formed during the grafting with very minor quantities of Ta-OH species that are indictable or even may not exist. Another important piece of evidence regarding the formation of Ta-O bond on all the crystal planes can be observed by DRIFT spectroscopy. The $\nu_{(Ta\text{-}O)}$ band appears at approximately 930 cm^{-1} which translates to formation of covalent bond/s between the substrate surface and complex (**1**)[21].

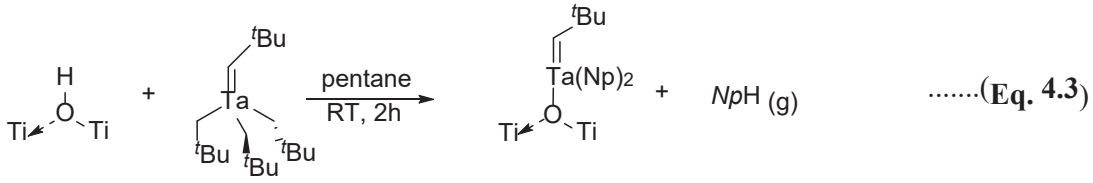

.....(**Eq. 4.3**)

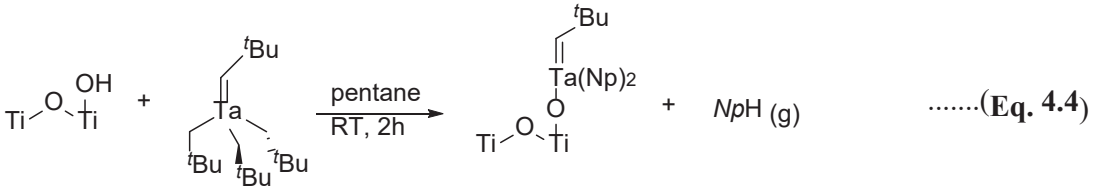

.....(**Eq. 4.4**)

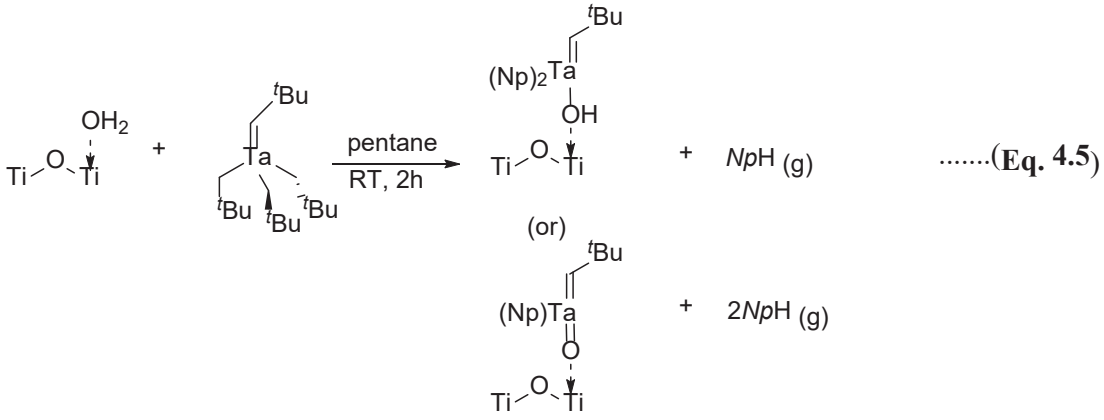

.....(**Eq. 4.5**)

Unfortunately, since a CaF_2 window (λ cut-off 1000 cm^{-1}) was used while performing the DRIFT spectroscopy the aforementioned band was not observed. Since, SSNMR did not produce ^{13}C signals corresponding to alkyl and alkene C's it was not possible to understand the behaviour of the organic species in the solid (4b).

4.4 Conclusions

$Ta[-CH_2C(CH_3)_3]_3[=CHC(CH_3)_3]$ was successfully grafted on $TiO_{2(700)}$ as evident by release of NpH (g) and occurrence of ν_{C-H} bands corresponding to alkyl groups of complex (**1**) in IR spectra. Grafting of 1 Ta/nm^2 and 14C/Ta was obtained after the first step by elemental analysis. This value (1 Ta/nm^2) is close to the net concentration of surface hydroxyls (0.7 OH/nm^2) and 1 NpH evolved / Ta grafted suggesting the formation of a monopodal species; with complete coverage of the surface hydroxyls. EPR spectra suggested the formation of surface "Ti^{3+}" ions that were absent initially recalling the known "self-doping" phenomena for TiO_2. We can propose in our case a mechanism based on the oxophilic nature ot tantala carbon bond: this can be converted into an oxygen trap leading to the formal reduction of Ti(IV) to "Ti(III)", thus explaining the evolution of the observed EPR spectrum.

Furthermore, the study of tantala-titania solid synthesized using SOMC by EXAFS have been previously attempted in our group. In the transmission mode, we were not successful since the TiO_2 support absorbs too much of the incident X-ray beam. Studies using measurements in the fluorescence mode would be possible and interesting but would need much more beam-time for recordings.

SOMC technique which can create well-defined grafting of organometallic complexes on the substrate surface.[22] is tributary of the complexity of the starting surface as well as the oxygen moieties in the sub-surface network of highly dehydroxylated titania.

PART II

SOMC by Werner coordination chemistry

Chapter 4

Grafting Organometallic complex on Titania *via* SOMC

Part II: SOMC by Werner coordination chemistry

Chapter 4

Part II: SOMC by Werner coordination chemistry

4.5 Introduction

The surface of highly dehydroxyated anatase ($TiO_{2(700)}$) is dominated by Lewis acidic sites (Ti_{5c},Ti_{4c}) rather than surface hydroxyls as established in the previous chapter. Several studies have been performed over decades to realize the main characteristics of performing Werner coordination chemistry on titania.[23–32] These studies include a wide range of experiments involving DFT modelling, infrared spectroscopy, TPD studies etc. on different crystal planes of anatase and defines the coordination, stability and activity of the coordinating species. In particular, the aromatic coordinating moieties are interesting as they can trap the electrons generated during the photoemission process thereby delaying the electron-hole recombination.[5,33] This delay can help in increasing the efficiency of photo-redox processes and plays an important role in the rate determining step.

Taking this into consideration, we aimed our work to first study the Werner properties of the surface using a well-known probe molecule; Pyridine. Once the relationship between Lewis acidic sites and the probe molecule was established it was utilized to perform Werner chemistry with the target molecule *i.e.* 2-methyl Imidazole (**2-mIm**). It is important to remember that 2-mIm adsorption/desorption study on TiO_2 anatase has never been reported and we have attempted to make the best possible fit based on coordination of 2-mIm with other metal-organic frameworks.[34,35]

The coordination of imidazole linkers to $TiO_{2(700)}$ was attempted as such sort of aromatic linkers have been known to delay the electron-hole recombination rate in a photocatalytic metal oxide *i.e.* titania thereby enhancing its catalytic property.[33] At the same time, 2-mIm is an ideal molecule as it consists of a Brønsted acidic site (–N-H) that can be used to graft organometallic complex using SOMC.

4.6 Results and Discussion

4.6.1 *In situ* monitoring of pyridine desorption by DRIFT spectroscopy

IR spectroscopic inquiries of pyridine adsorption and desorption has proved to be an efficient method for identifying the nature and concentration of acidic sites on the surface of metal oxides.[36–39] The technique allows us to determine qualitatively the acidic and basic sites, surface hydroxyls etc. present on the surface. The lone pair of electrons on the nitrogen atom provides sufficient basic character to the molecule and thus pyridine is used as a probe for the acid sites on metal oxide surfaces.[37,40] TiO_2 anatase with (101) and (001) facet is known to display Lewis acidic sites (Ti_{5c}) and Brønsted basic sites (O_{2c}).[41] These sites acts as coordination sites for pyridine adsorption.

Pyridine (gas phase) was introduced in a pyrex reactor containing a known amount of $TiO_{2(700)}$ (~40 mg) at room temperature. After exposure to pyridine vapour pressure the solid was evacuated under reduced pressure. Removing the excess pyridine under UHV also eliminates the weakly physisorbed molecules of pyridine on surface of $TiO_{2(700)}$. The resultant solid i.e. pyridine adsorbed $TiO_{2(700)}$ (**Py-$TiO_{2(700)}$**), was monitored by DRIFT spectroscopy while heating the sample from 20°C to 500°C. At 20°C, 6 different absorption peaks were observed in 1200-1700 cm^{-1} range that corresponds to C-C and C-N ring modes. The peak frequency and sharpness of the strong ν_{19b} absorbance which appears at 1445 cm^{-1} corresponds to the C-N-C stretching mode of pyridine and is termed as a pyridine ring-breathing mode. The position of the ν_{19b} absorbance at 1445 cm^{-1} confirms that pyridine molecules are chemisorbed on the Lewis acidic sites of TiO_2 anatase.[37,42] The frequency of this mode is most strongly affected by the interaction between the nitrogen lone pair of pyridine molecule and the substrate surface.[37,42,43] A low intensity peak at 1492 cm^{-1} due to ν_{19a} absorbance further indicates the presence of electron acceptor sites on titania's surface.[44] In the ν(CCN) region, a shoulder on the lower wavenumber side is seen on both the ν_{19a} (peak at 1492 cm^{-1}) and the ν_{19b} (peak at 1445 cm^{-1}) indicating that there is more than one type of Lewis acid site on the TiO_2 surface. Similarly, the peaks at 1576 cm^{-1} and 1603 cm^{-1} are symptomatic of pyridine coordination to Lewis acidic sites.[37] As shown in Figure 4.4, concomitant desorption of pyridine was observed with steady increase in temperature and lead to relatively complete removal of the N-heterocycle at around

350°C. During, the desorption process, no other peaks were observed to be appearing indicating no decomposition of pyridine on surface of anatase. This directs our consideration towards the stability of such N-heterocyclic species on surface of titania. Green *et. al.*[36] reported the DFT calculations of bonding energies of pyridine adsorbed

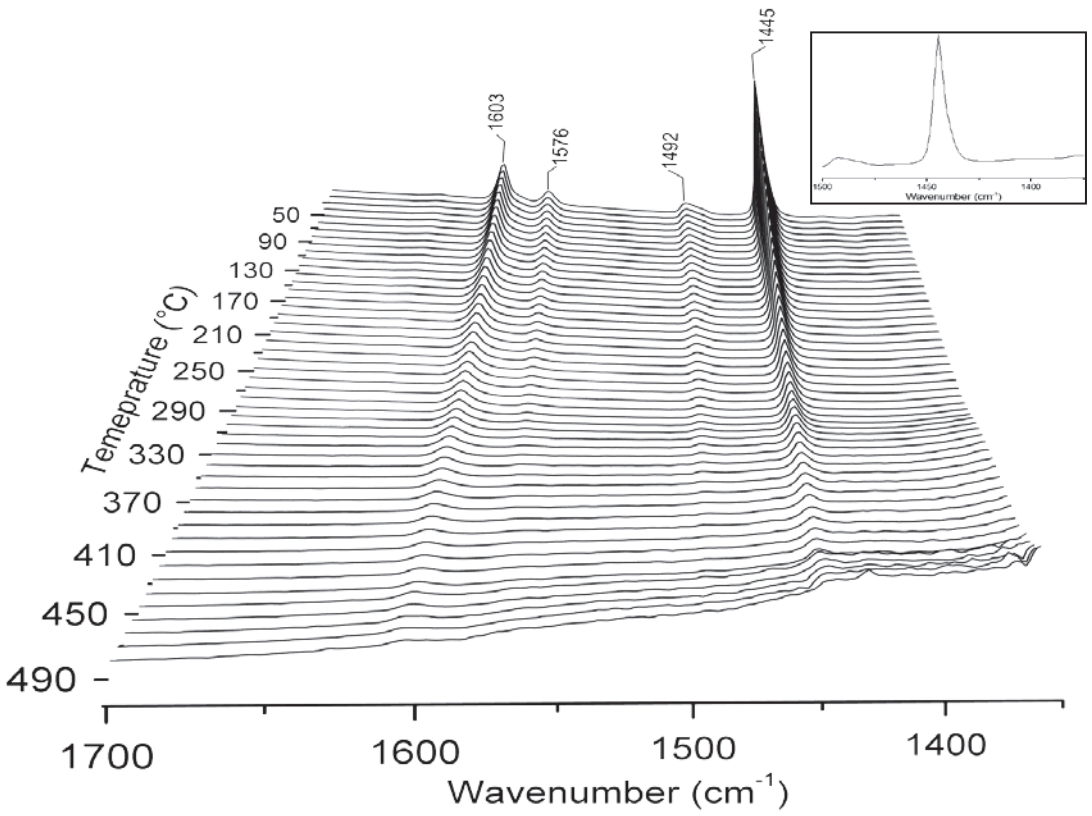

Figure 4.4 *In situ* infrared spectra of pyridine (pre-adsorbed on $TiO_{2(700)}$) desorption recorded every 10 °C between 20 °C and 500 °C (ramp rate 2 °C min^{-1}). Inset shows the shoulder on the lower wavenumber side for 1492 cm^{-1} and 1445 cm^{-1} at 20°C.

on anatase (101) and rutile (110); the dominant crystal planes present in anatase and rutile. The adsorption energy of pyridine adsorbed on rutile (110) was 71 kJ/mol whereas similar phenomena on anatase (101) had 85 kJ/mol which was 14 kJ/mol stronger than on rutile despite a very low difference (~0.04 Å) in the Ti-N bond length. This increase in adsorption energy on anatase (101) was associated with increased hydrogen bonding on the surface (Figure 4.5).

The adsorption of pyridine is stronger when the plane of pyridine is aligned perpendicular to the plane of bridging oxygen atoms and the Ti center such that the H-atoms on pyridine can interact with the bridging O_{2c} compared to when it's normally

aligned. This effect causes the pyridine to adsorb more strongly on anatase (101) which is a predominant species in our sample.

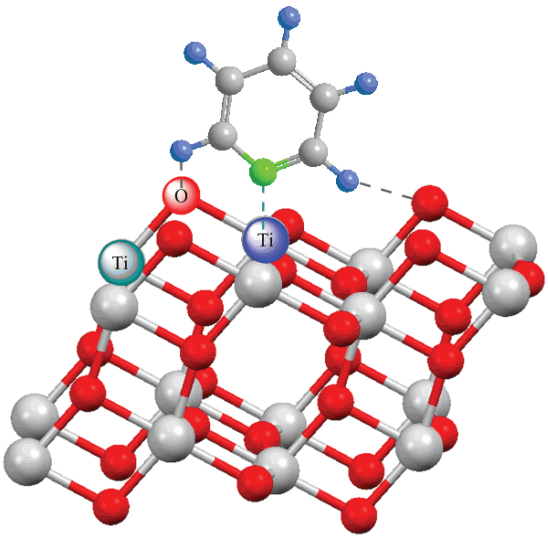

Figure 4.5 Schematic representation of pyridine adsorption on TiO_2 anatase (101) facet. The grey balls in the ring are C, green is N and blue is H.

The *in situ* DRIFT study with pyridine abetted to understand qualitatively the presence and nature of Lewis acidic sites. The study was found to be coherent with the reported literature and confirms the presence of mainly Lewis acidic sites. Since, no dominant peak corresponding to PyH^+ was observed it can be concluded that the Lewis acid chemistry is prominent on the substrate surface. The next step was to perform similar study with the targeted aromatic specie 2-methyl Imidazole (**2-mIm**) to understand its stability on the surface of $TiO_{2(700)}$.

4.6.2 *In situ* monitoring of 2-methyl Imidazole desorption by DRIFT spectroscopy

2-mIm was pre-adsorbed on $TiO_{2(700)}$ using pseudo CVD method. Briefly, both the solids were introduced in a pyrex reactor and the system was evacuated under UHV. The reactor was then sealed and heated at 120°C, cooled down to room temperature under Ar and encapsulated inside the DRIFT cell. Figure 4.6a and 4.6b shows the infrared spectra recorded in the 2-mIm desorption study. At 20°C, absorption peaks at 1293 cm^{-1}, 1358 cm^{-1}, 1426 cm^{-1} and 1565 cm^{-1} were observed between 1200-1900 cm^{-1} while the latter two frequencies having a shoulder at a higher wavenumber

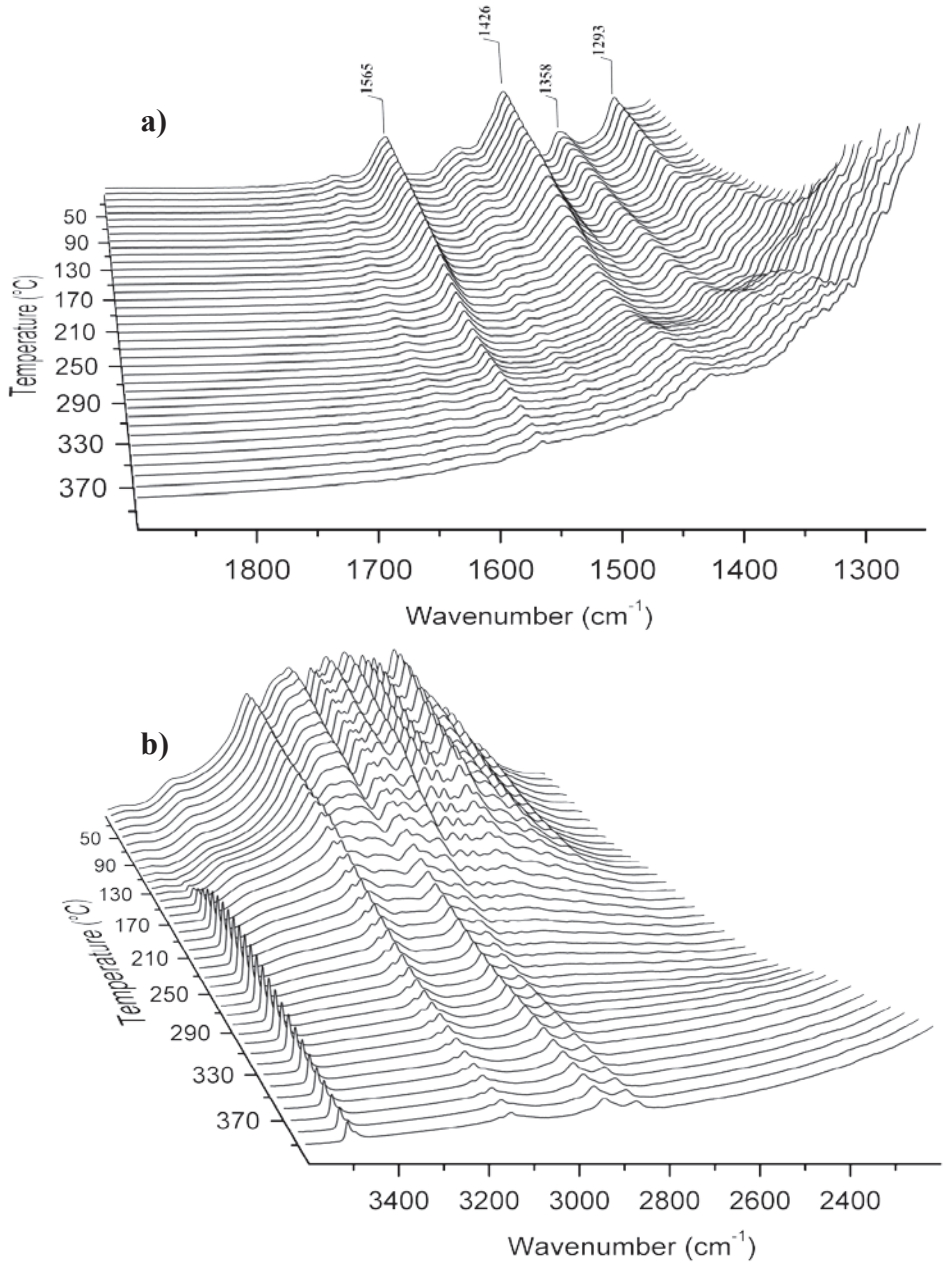

Figure 4.6 *In situ* infrared spectra of 2-mIm (pre-adsorbed on $TiO_{2(700)}$) desorption recorded every 10 °C between 20 °C and 400 °C (2 °C min^{-1}) in **a)** 1200-1900 cm^{-1} region and **b)** 2200-3600 cm^{-1} region. For full spectra at 20°C see **Annex IV**.

respectively. These vibrations reflect the coordination of 2-mIm with the Lewis acidic sites on $TiO_{2(700)}$. The shoulder at higher wavenumbers for absorption peaks at 1426 cm^{-1} and 1565 cm^{-1} can be due to the coordination of 2-mIm on the Lewis acidic sites *via* electron lone pair of N-H and not N as shown in Figure 4.7. It is interesting to note that the resonance between the N—H • • •N "out of plane" bending and N-H stretching vibration[45,46] at ~ 1845 cm^{-1} was absent in 2-mIm adsorbed $TiO_{2(700)}$. This gives us an information about the orientation of the 2-mIm molecule. The absence of this peak

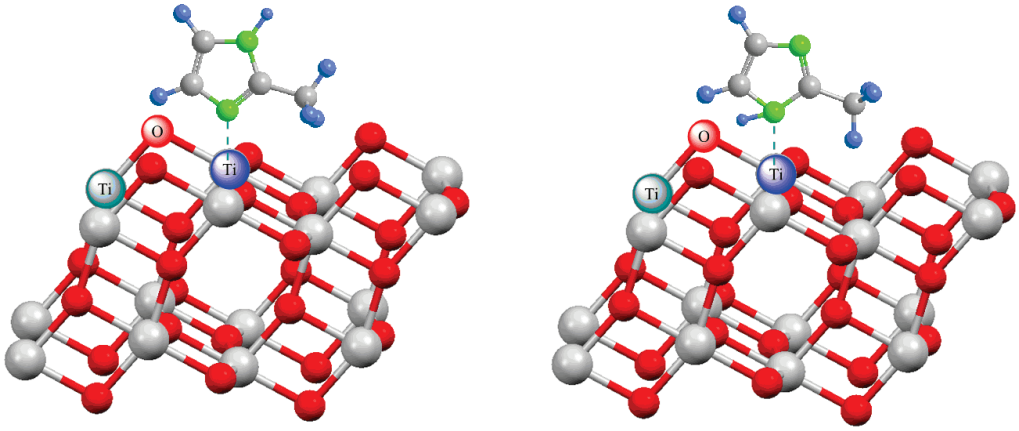

Figure 4.7 Schematic representation of 2-mIm adsorption on TiO_2 anatase (101) facet. The grey balls in the ring are C, green is N and blue is H.

represents the stalling of out of plane bending of N—H • • •N which can be caused due to the horizontal alignment of the 2-mIm molecule with respect to the crystal plane instead of a vertical alignment. Moreover, if the molecule is aligned in a horizontal position w.r.t. the crystal plane we can also expect H-bonding interactions of the –CH, –NH and $–CH_3$ groups of the N-heterocycle with the Brønsted basic O_{2c} present on the surface.

A broad and strong absorption band between 2500-3400 cm^{-1} as shown in Figure 4.6b corresponds to stretching vibrations of hydrogen bonds established between the pyrrole group and the pyridinic nitrogen (N—H • • •N).[47,48,34] A complex multiplet absorption spectrum in this region suggests the interaction of –CH and $–CH_3$ groups with the surface as well as the physisorbed 2-mIm fragments. A broad absorption peak at 3153 cm^{-1} is due to the stretching vibrations of C—H bands in methyl and imidazole ring.[47]

As desorption temperature was increased a decrease in the intensity of the peaks was observed while no new signal appeared in 1200-1900 cm^{-1}. At approximately 350°C, most of the 2-mIm adsorbed on Lewis acidic sites disappeared. On the other hand, in the stretching region a new absorption peak at 3505 cm^{-1} appears upon increasing the temperature to 130°C with a shoulder at lower wave number, attains a maxima at ~200°C and then continuously decreases in intensity up till 400°C. This sharp peak corresponds to $\nu_{N—H}$ stretching vibration and is slightly shifted to a lower wavenumber due to the coordination of 2-mIm on a Lewis acidic surface.[49] The delayed appearance of this peak can be correlated to the interaction of the chemisorbed 2-mIm species with

the physisorbed species thereby broadening the absorption frequency of this stretching vibration making it difficult to identify at room temperature. At elevated temperature, when the physisorbed species slowly starts to eliminate stretching vibrations analogous to isolated N—H bond starts to appear and achieves a maxima at around 200°C indicating that most of the pyrrole group are isolated on the surface.

Another interesting conjuncture was the splitting of the broad absorption peak at 3153 cm^{-1} that corresponds to stretching vibrations of C—H bands in methyl and imidazole ring at 130°C into two peaks that drifted apart from each other as the temperature was increasing. At 200°C, the two peaks were identified at 3136 cm^{-1} and 3154 cm^{-1} whereas when the temperature was increased to 350°C the peaks had an absorption frequency of 3136 cm^{-1} and 3166 cm^{-1} respectively. The peak at 3136 cm^{-1} specifically corresponds to $\nu_{C—H}$ bands in methyl and imidazole ring[47] while the reasons for the movement of the second peak with increasing temperature and its nature still remain unknown. The next phase was the formation and quantification of surface coordinated 2-mIm species.

4.6.3 Elemental Analysis of 2-mIm@$TiO_{2(700)}$

As discussed in previous chapter, a clean anatase surface on an average consists of 5 Lewis acidic sites/ nm^2 irrespective of the crystal plane. These sites can be used as active centres for performing Werner chemistry on the surface of titania.[26,29,32,33,50] 2-mIm was adsorbed using the same method described previously (Chapter 2). Once adsorbed the resultant solid was calcined at 200°C under UHV to remove the excess 2-mIm. The resultant solid (**2-mIm@$TiO_{2(700)}$**) was then moved into glove box. The amount of 2-mIm chemisorbed on $TiO_{2(700)}$ was determined by elemental analysis. A layer of 2-mIm consisting of 3.5 2-mIm/nm^2 or 0.31 mmol 2-mIm/g of $TiO_{2(700)}$ was obtained after the aforementioned treatment. We were able to achieve a 70% surface coverage using this technique. This may be due to the residual surface hydroxyls that are bound to Ti_{5c}. Another reason can be the orientation of the aromatic system. Instead of being vertically aligned they may be horizontally aligned w.r.t. surface as the case of pyridine.

4.6.4 Solid State NMR spectroscopy

^{13}C CPMAS SSNMR was used to identify the structure and grafting of 2-mIm on $TiO_{2(700)}$ (**Annex V**). Signals at 12 ppm and 144 ppm were assigned to the carbon of C6 and C1 respectively.[51] Signal corresponding to C4 and C3 at 121 ppm was not seen

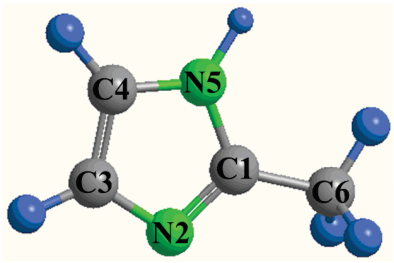

but instead two intense signals at 129 ppm and 110 ppm were observed. This may be because the symmetric C4 and C3 carbon have lost the C_2 symmetry due to the molecule's interaction with the surface. Thus, C4 and C3 carbon becomes non-equivalent and generates two different signals unlike non-grafted 2-mIm molecules.

Thomas *et. al.*[26] reported the adsorption of p-amino benzoic acid on TiO_2 anatase (101) surface by DFT, NEXAFS, UV-Vis. and valence band photoelectron spectroscopy. Their work showed that p-amino benzoic acid was adsorbed on anatase (101) surface in a bidendate fashion most likely bridging neighbouring Ti_{5c}. The proton on the carboxyl was abstracted before adsorption but did not lead to the formation of zwitter ion as supported by experimental and DFT calculations. The amine group on the ring was intact and away from the surface indicating its availability for grafting biomolecules, quantum dots and even organometallic precursors. Most likely similar phenomena must be occurring in our case where the amine is intact and far away from the surface. Although, advanced techniques must be required before remarking on the chemistry with most certainty.

4.7 Conclusion

The inspection of 2-mIm desorption off $TiO_{2(700)}$ unravelled that 2-mIm is coordinated to Lewis acidic sites and is stable at high temperatures. We also learned that desorption at high temperature (**~200°C**) can lead to elimination of physisorbed species and formation of isolated chemisorbed 2-mIm molecules on TiO_2 anatase dehydroxylated at 700°C with a (101) predominant crystal plane. With a loading of 3.5 2-mIm/nm^2, the chemisorbed species probably forms a monolayer on the surface but no conclusive proof was determined. SSNMR suggested the presence of an intact 2-mIm molecule with asymmetric –C=C– indicating the interaction of the moiety with the surface.

The chemisorption of 2-mIm on different crystal planes provides us with a homogeneous surface consisting mainly of Brønsted acidity coming from the aromatic amine. It would be interesting to graft organometallic species on this surface and understand their interaction with the aromatic ring as well as the substrate surface. Another approach, could be formation of metal-organic frameworks (MOF's) like structure (for example, ZIF-8) on the surface of anatase. MOF's are well-known for their gas storage application.[52] Developing such structures may enhance the photo-reduction efficiency of TiO_2 by increasing the concentration of the reactant on the surface.[53] This study will be continued later.

4.8 References

(1) Huang, H.; Lin, J.; Fan, L.; Wang, X.; Fu, X.; Long, J. *J. Phys. Chem. C* **2015**, *119* (19), 10478–10492.

(2) Grasser, S.; Haeßner, C.; Köhler, K.; Lefebvre, F.; Basset, J.-M. *Phys. Chem. Chem. Phys.* **2003**, *5* (9), 2–7.

(3) Gu, Q.; Long, J.; Zhou, Y.; Yuan, R.; Lin, H.; Wang, X. *J. Catal.* **2012**, *289* (September), 88–99.

(4) Fan, L.; Long, J.; Gu, Q.; Huang, H.; Lin, H.; Wang, X. *J. Catal.* **2014**, *320* (1), 147–159.

(5) Huang, H.; Lin, J.; Zhu, G.; Weng, Y.; Wang, X.; Fu, X.; Long, J. *Angew. Chemie - Int. Ed.* **2016**, *55* (29), 8314–8318.

(6) Avenier, P.; Xavier, A.; Ae, S.-M.; Veyre, L.; Filippo, A.; Ae, R.; Basset, J.-M.; Odile, A.; Ae, E.; Taoufik, M.; Elsje, A.; Quadrelli, A. *Top. Catal.* **2009**, *52*, pp 1482-1491.

(7) Le Roux, E.; Chabanas, M.; Baudouin, A.; De Mallmann, A.; Copéret, C.; Quadrelli, E. A.; Thivolle-Cazat, J.; Basset, J. M.; Lukens, W.; Lesage, A.; Emsley, L.; Sunley, G. J. *J. Am. Chem. Soc.* **2004**, *126* (41), 13391–13399.

(8) Chabanas, M.; Quadrelli, E. A.; Fenet, B.; Copéret, C.; Thivolle-Cazat, J.; Basset, J.-M.; Lesage, A.; Emsley, L. *Angew. Chemie Int. Ed.* **2001**, *40* (23), 4493.

(9) Gourez, E.; Avenier, P.; Solans-Monfort, X.; Veyre, L.; Baudouin, A.; Kaya, Y.; Taoufik, M.; Basset, J.-M.; Eisenstein, O.; Quadrelli, E. A. *New J. Chem. New J. Chem* **2011**, *35* (35), 961–1148.

(10) Dufaud, V.; Niccolai, G. P.; Thivolle-Cazat, J.; Basset, J.-M. *J. Am. Chem. SOC* **1995**, *117*, 4288–4294.

(11) Lefort, L.; Chabanas, M.; Maury, O.; Meunier, D.; Copéret, C.; Thivolle-Cazat, J.; Basset, J.-M. *J. Organomet. Chem.* **2000**, *593* (594), 96–100.

(12) Schrock, R. R. *Acc. Chem. Res.* **1979**, *12* (3), 98–104.

(13) Hurum, D. C.; Agrios, A. G.; Gray, K. A.; Rajh, T.; Thurnauer, M. C. *J. Phys. Chem. B* **2003**, *107* (19), pp 4545-4549.

(14) Hurum, D. C.; Agrios, A. G.; Crist, S. E.; Gray, K. A.; Rajh, T.; Thurnauer, M. C. *J. Electron Spectros. Relat. Phenomena* **2006**, *150*, 155–163.

(15) Su, J.; Zou, X.; Chen, J.-S. *RSC Adv.* **2014**, 4, 13979-13988.

(16) Schrock, R. R. *Chem. Commun.* **2005**, (22), 2773.

(17) Schrock, R. R.; Guggenberger, L. J.; English, A. D. *J. Am. Chem. Soc.* **1976**, *98* (4), 903–913.

(18) Setvin, M.; Franchini, C.; Hao, X.; Schmid, M.; Janotti, A.; Kaltak, M.; Van De Walle, C. G.; Kresse, G.; Diebold, U. *Phys. Rev. Lett.* **2014**, *113* (8), pp 086402(5).

(19) Selcuk, S.; Selloni, A. *Nat. Mater.* **2016**.

(20) Otting, G. *Annu. Rev. Biophys.* **2010**, *39* (1), 387–405.

(21) Arbuj, S. S.; Mulik, U. P.; Amalnerkar, D. P. *Nanosci. Nanotechnol. Lett.* **2013**, *5* (9), 968–973.

(22) Copéret, C.; Comas-Vives, A.; Conley, M. P.; Estes, D. P.; Fedorov, A.; Mougel, V.; Nagae, H.; Núnez-Zarur, F.; Zhizhko, P. A. *Chem. Rev.* **2016**, *116* (2), 323–421.

(23) Hadjiivanov, K.; Klissurski, D.; Busca, G.; Lorenzelli, V. *J. CHEM. SOC. FARADAY TRANS* **1991**, *87* (1), 175–178.

(24) Busca, G.; Saussey, H.; Saur, O.; Lavalley, J. C.; Lorenzelli, V. *Appl. Catal.* **1985**, *14* (C), 245–260.

(25) Morterra, C. *J. Chem. SOC. Faraday Trans. I* **1988**, *84* (5), 1617–1637.

(26) Thomas, A. G.; Jackman, M. J.; Wagstaffe, M.; Radtke, H.; Syres, K.; Adell, J.; Lévy, A.; Martsinovich, N. *Langmuir* **2014**, *30* (41), 12306–12314.

(27) Syres, K. L.; Thomas, A. G.; Flavell, W. R.; Spencer, B. F.; Bondino, F.; Malvestuto, M.; Preobrajenski, A.; Grätzel, M. *J. Phys. Chem. C* **2012**, *116* (44), 23515–23525.

(28) Kim, K. S.; Barteau, M. A.; Farneth, W. E. *Langmuir* **1988**, *4* (3), 533–543.

(29) Chen, H.-Y. T.; Tosoni, S.; Pacchioni, G. *Surf. Sci.* **2016**, *652*, 163–171.

(30) Lang, S.; Benz, M.; Obenaus, U.; Himmelmann, R.; Hunger, M. *ChemCatChem* **2016**, *8* (12), 2031–2036.

(31) Martra, G. *Appl. Catal. A Gen.* **2000**, *200* (1–2), 275–285.

(32) Ma, J.-G.; Zhang, C.-R.; Gong, J.-J.; Yang, B.; Zhang, H.-M.; Wang, W.; Wu, Y.-Z.; Chen, Y.-H.; Chen, H.-S. *J. Chem. Phys.* **2014**, *141* (23), 234705.

(33) Martini, L. A.; Moore, G. F.; Milot, R. L.; Cai, L. Z.; Sheehan, S. W. *J.Phys.Chem.C* **2013**, *117* (28), pp 14526−14533.

(34) Xu, F.; Kou, L.; Jia, J.; Hou, X.; Long, Z.; Wang, S. *Anal. Chim. Acta* **2013**, *804*, 240–245.

(35) Stassen, I.; Styles, M.; Grenci, G.; Gorp, H. Van; Vanderlinden, W.; Feyter, S. De; Falcaro, P.; Vos, D. De; Vereecken, P.; Ameloot, R. *Nat. Mater.* **2016**, *15* (3), 304–310.

(36) Green, I. X.; Buda, C.; Zhang, Z.; Neurock, M.; Yates, J. T. *J. Phys. Chem. C* **2010**, *114*, 16649–16659.

(37) Zaki, M. I.; Hasan, M. a.; Al-Sagheer, F. a.; Pasupulety, L. *Colloids Surfaces A Physicochem. Eng. Asp.* **2001**, *190* (3), 261–274.

(38) Tanaka, Katsumi; White, J. M. *J. Phys. Chem.* **1982**, *86* (24).

(39) Nakabayashi, H.; Kakuta, N.; Ueno, A. *Bull. Chem. Soc. Jpn.* **1991**, *64* (8), 2428–2432.

(40) Bludau, H.; Karge, H. G.; Niessen, W. *Microporous Mesoporous Mater.* **1998**, *22* (1–3), 297–308.

(41) Bourikas, K.; Kordulis, C.; Lycourghiotis, A. *Chem. Rev.* **2014**, *114* (19), 9754–9823.

(42) Bezrodna, T.; Puchkovska, G.; Shimanovska, V.; Chashechnikova, I.; Khalyavka, T.; Baran, J. *Appl. Surf. Sci.* **2003**, *214* (1–4), 222–231.

(43) Knöuzinger, H. *Adv. Catal.* **1976**, *25*, 184–271.

(44) Parfitt, G. D.; Ramsbotham, J.; Rochester ’f, C. H. *Trans. Faraday Soc.* **1971**, *67*, pp 1506-1507.

(45) Li, X.; Gao, X.; Ai, L.; Jiang, J. *Chem. Eng. J.* **2015**, *274*, 238–246.

(46) Tran, U. P. N.; Le, K. K. A.; Phan, N. T. S. **2011**, *1*, 120–127.

(47) Hachuła, B.; Nowak, M.; Kusz, J. *J. Chem. Crystallogr.* **2010**, *40* (3), 201–206.

(48) Bustamante, E. L.; Fernández, J. L.; Zamaro, J. M. *J. Colloid Interface Sci.* **2014**, *424*, 37–43.

(49) Kürkçüoğlu, G. S.; Yeşilel, O. Z.; Çaylı, İ.; Büyükgüngör, O. *J. Inorg. Organomet. Polym. Mater.* **2011**, *21* (2), 306–315.

(50) Araña, J.; Alonso, A. P.; Rodríguez, J. M. D.; Colón, G.; Navío, J. A.; Peña, J. P. *Appl. Catal. B Environ.* **2009**, *89* (1–2), 204–213.

(51) Papadopoulos, E. P.; Hollstein, U. *Org. Magn. Reson.* **1982**, *19* (4), 188–191.

(52) Furukawa, H.; Cordova, K. E.; O'Keeffe, M.; Yaghi, O. M. *Science* **2013**, *341* (6149), 1230444.

(53) Marepally, B. C.; Ampelli, C.; Genovese, C.; Saboo, T.; Perathoner, S.; Wisser, F. M.; Veyre, L.; Canivet, J.; Quadrelli, E. A.; Centi, G. *ChemSusChem* **2017**, 10 (22), 4442-4446.

Chapter 5

3D-type meso/macro porous structured photoanodes based on Ti mesh

Chapter 5

3D-type meso/macro porous structured photoanodes based on Ti mesh

Chapter 5

5.1 Introduction

In previous chapters we have successfully identified, quantified and modified the titanols, and to a lesser extent the acidic Ti(IV) and reduced "Ti(III)" centers present on the surface of TiO_2 anatase powder. Nevertheless, powder may not be the ideal conditioning when it comes to the application of this semiconductor oxide. Ampelli *et.al* showed that although P25 Degussa powder showed water splitting activity, a uniform array of TiO_2 nanotubes showed one order of magnitude higher activity with respect to the powder.[1] The influence of cell geometry in a photocatalytic water splitting process was also explored.

TiO_2 nanotubes offer advantage over conventional TiO_2 powder due to the following facts: *i*) higher light harvesting due to the vertical alignment of the nanotubes which permits vertical charge transport; *ii*) easier electron diffusion from anode to cathode as the nanotubes are supported on Ti metal and *iii*) higher surface area in a compact setup.[2–6]

TiO_2 nanotubes can be formed by different methods such as sol-gel techniques, hydro/solvothermal methods with or without templates[7–16], atomic layer deposition (ALD) into the template[17–19] and anodic oxidation[1,6]. Many of these processes involve use of titanium alkoxide precursors to undergo acid catalysed hydrolysis reaction followed by condensation reactions. Therefore, the end results are single tubes or loose agglomerates of tubes dispersed in a solution and often a wide distribution of tube length is observed. On the contrary, Anodic oxidation or electrochemical anodization

approach is self-organizing: meaning an array of well-defined, perpendicularly aligned (to the substrate surface) titania nanotubes of controllable (and well-defined) length can be achieved.[20–23] Since, the tubes originate from the substrate surface (our case) they are electrically connected and easy to handle. This method overrides other methods considering that any shape of titanium can be converted into a template consisting of a dense layer of well-defined TiO_2 nanotubes while operating under mild conditions.

TiO_2 nanotubes have been fabricated by anodic oxidation on different Ti substrates such as Ti foils[24], Ti meshes[25] etc. to harvest energy from the incoming photons and perform photocatalysis. Amongst different Ti substrates, TiO_2 nanotube arrays fabricated on Ti gauze offers higher specific surface area, 3-D hierarchical meso/macro porous structure, flexibility and low dependence on the angle of incident light.[26–28] The design of such catalytic system was inspired from hierarchical porous zeolites that show superior performances with respect to the original zeolites in different catalytic processes involving heterogeneous catalysts, such as in selective oxidative processes[29], or in enhancing the adsorbing properties for CO_2 capture[30]. Such a system might also help understanding the relationship between the hierarchical meso/macro porosity in TiO_2 and the overall electron transport and proton diffusion, with the aim of minimizing the overpotential phenomena inside the cell.

Owing to the aforementioned advantages, we decided to study and improve the route to compact array of TiO_2 nanotubes with 3-D hierarchical meso/macro porosity on Ti gauze through anodic oxidation. The aim is to sufficiently improve the photocatalytic performance of the system with respect to the state of the art (which still needs photosensitizer or external potential) in order to achieve improved self-standing well-structured nanomaterial.

5.2 Results and Discussion

5.2.1 Structural and morphological properties of 3D-type structured Ti photoanodes

Anodic oxidation[31] (as described in Chapter 2) was employed on a Ti mesh (gauze) to obtain 3D type structured Ti photoanodes composed of titania nanotubes (**TNT's**). Figure 5.1 shows SEM images of the Ti mesh prior and after anodization. The surface of the gauze is not perfectly smooth, due to the presence of a thin layer of oxide passivating the metallic surface, as confirmed by EDX analysis.

After the anodization process, highly ordered TiO_2 nanotube arrays were formed on the round surface of the woven Ti wires. The formation of the TNTs did not alter the macro-structure of the original Ti mesh, and 36 % open area was maintained after the anodization (Figure 5.1b). The resultant structure therefore displays two types of porosity like hierarchical porous zeolites[32–34]: i) a mesoporosity due to the TiO_2 nanotubes having an inner diameter in the range 40-120 nm, ii) a macroporosity due to the meshes of the initial Ti gauze (80 mesh). While the mesoporosity plays an important role in electron trapping and charge diffusion[35] the macroporosity equally helps in proton diffusion that are generated during the water photo oxidation process *via* PEM to the cathode for H_2 production. The sample anodized at higher voltage (60 V) showed a partial detachment of the TNT layer from the Ti wires and the resulting TNTs-Ti gauze is reported in Figure 5.1c. A magnification of this SEM image (Figure 5.1e) evidenced the thickness of the photoactive layer, i.e. the length of the nanotubes, which measures 19.0 μm for a sample anodized at 60 V for 5 h. Figures 5.1d and f show two SEM images at different magnification, clearly evidencing the highly ordered arrays of TNTs. It is to note that for all the samples: i) vertically aligned TNTs with a circular shape were formed on the round surface of the woven Ti wires and ii) all the nanotubes on the top side are open. These results were similar to TNT's grown on a Ti disc as reported by Ampelli *et. al.*[36] and are important for light harvesting and charge separation phenomena.[6]

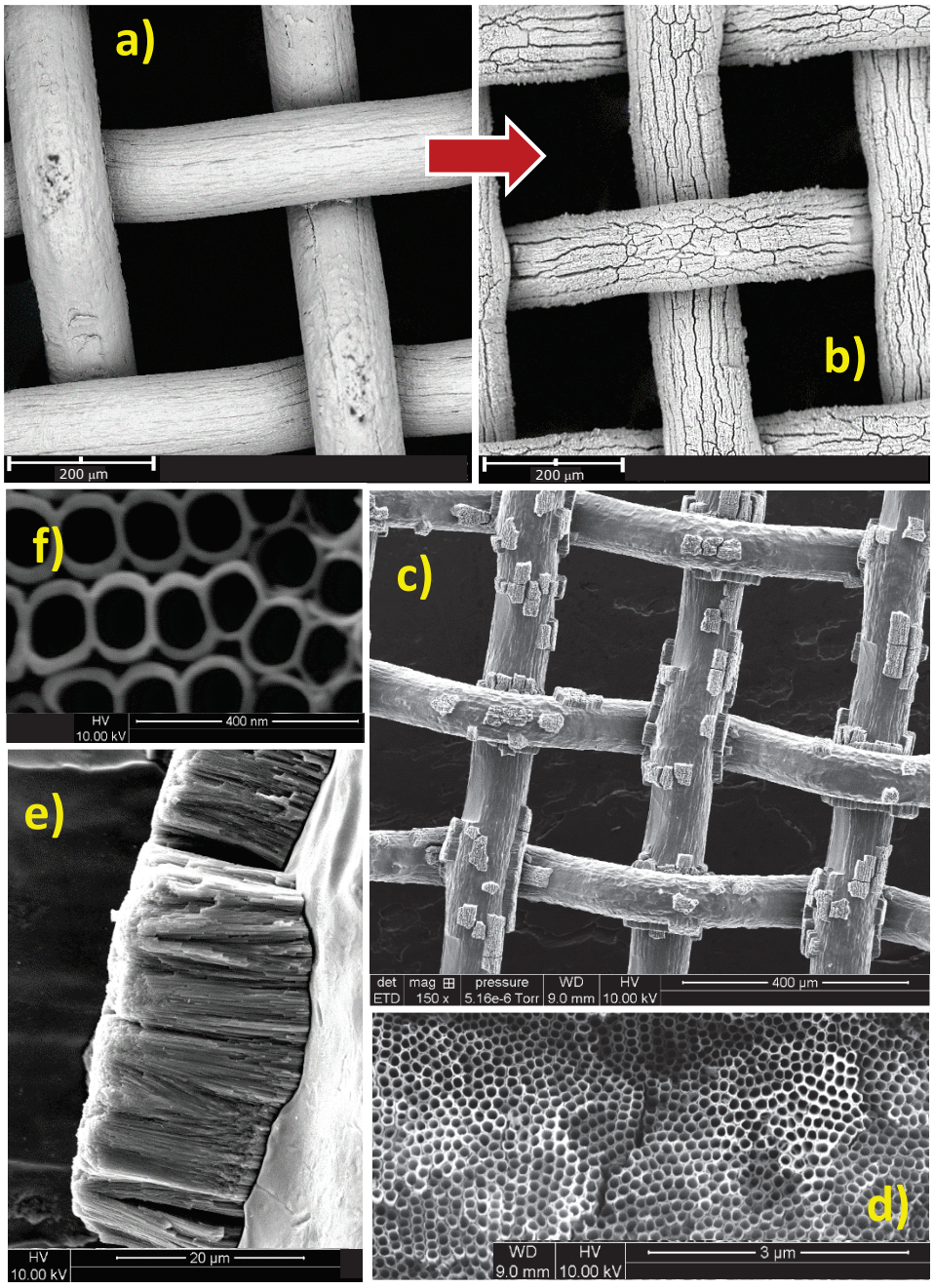

Figure 5.1 SEM images of: a) the Ti mesh before the anodization; b) the TNTs-Ti mesh after the anodization (50 V, 5 h); c) the TNTs-Ti mesh after anodization (60 V, 5 h) showing a partial detachment of TNTs; d) top of the TNTs (60 V, 5 h); e) cross section of TNTs-Ti mesh (60 V, 5 h); f) high magnification of top of TNTs (60 V, 5 h).

We then proceeded to a systematic study on the effect of the applied potential and the time of anodization on the structural parameters of TNTs. Table 5.1 summarizes the characteristics and nanostructure properties of all the TNTs-Ti mesh samples anodized by varying both applied voltage (from 40 to 60 V) and time of anodization (from 20 min to 7 h). The oxide layer sizes (nanotube diameter, wall thickness and length) were

directly obtained from the SEM images. The influence of the applied voltage was evaluated in the range 40-60 V for TNTs-Ti meshes anodized for 5 h. Juang *et. al.*[37] reported the relationship between applied voltage, nanotube length and diameter in an anodic process. They showed that increasing the potential between 20 V – 50 V the length and diameter of the nanotubes increases. Similar results were observed in our case when the voltage was increased from 40 to 50 V, bigger nanotubes both in terms of inner diameter (from 48 to 90 nm) and in terms of length (from 7.0 to 8.0 μm) were obtained.

Table 5.1 Structural properties of the TNTs-Ti meshes anodized at different applied voltage and time of anodization.

Applied potential (V)	***Anodization time (min)***	***TNTs length (μm)***	***TNTs wall thickness (nm)***	***TNTs inner diameter (nm)***
50	20	1.2	12	52
50	45	2.0	11	58
50	60	2.5	10	60
50	180	5.5	10	74
50	240	6.9	11	86
50	300	8.0	11	90
50	420	8.5	18	100
40	300	7.0	17	48
60	300	19	12	66

A further increase of the voltage up to 60 V produced longer nanotubes (19 μm) and reduced inner diameter. The polarization of Ti-O bonds due to strong electromagnetic fields generated *in situ* as a function of applied potential promotes dissolution of Ti^{4+} cations into the electrolytic solution and faster migration of Ti^{4+} and O^{2-} ions towards the metal/oxide interface.[38] Therefore, increasing the potential during the anodic oxidation process increases the nanotube length. However, at 60 V the inner diameter

was limited to 66 nm. Similar behaviour was observed for planar-type TNTs-based photoanodes.[5]

The growth mechanism of TiO_2 nanotubes as suggested by Ng *et. al.*[39] showed that the applied voltage greatly influences the first stage of nanotube formation when small pits originate on the early oxide layer. If the voltage is high, a strong electromagnetic field is generated and the number of pits per unit area (finally evolving in nanotubes) is higher. This means that at 60 V in our conditions there was no space enough for bigger nanotubes (see also the reduced voids among the nanotubes in Figure 5.1f). Moreover, the strong voltage was responsible for the partial detachment of the TNTs layer from the Ti wires, as shown in Figure 5.1c. In this view, the most stable TNTs-Ti meshes were obtained at 50 V and the influence of different anodization times was investigated at this selected voltage.

Figure 5.2 shows the profiles of length, internal diameter and percentage of voids (titania-free geometrical surface area of the electrode surface) of the 50 V anodized samples versus time of anodization.

An increase in length (from 1.2 µm for 20 min to 8.5 µm for 7 h) and inner diameter (from 52 nm for 20 min to 100 nm for 7 h) with the anodization time is observed. These results are in accordance with *Liu et. al.*[40] which reported a similar behaviour for 50-

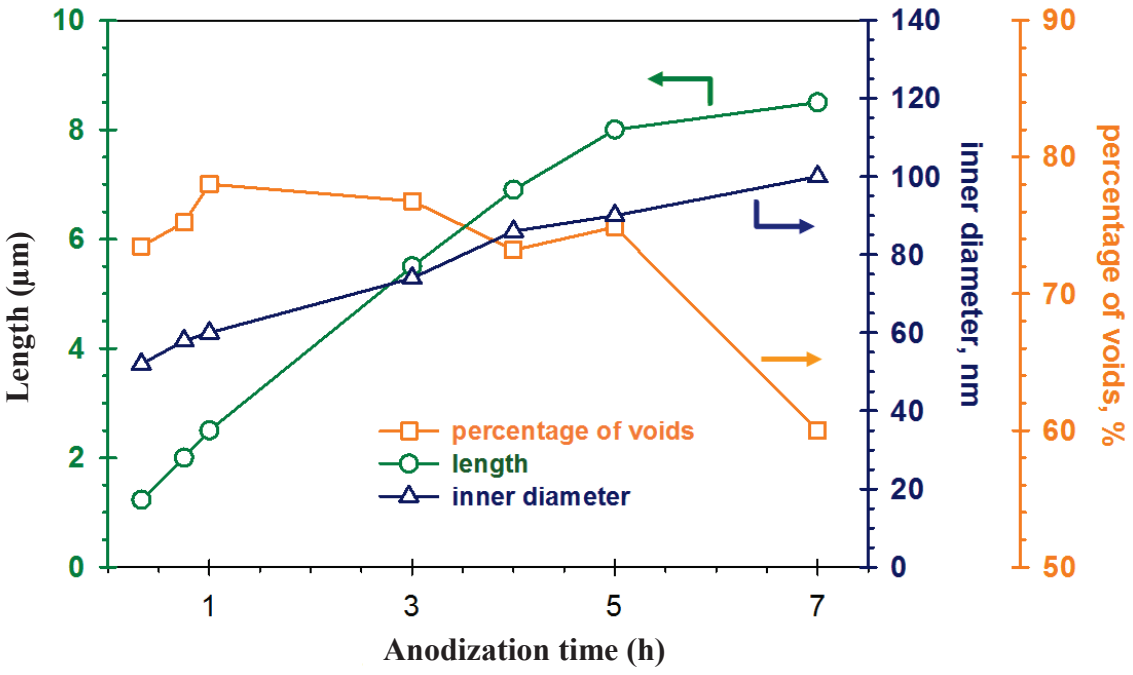

Figure 5.2 Profiles of length, internal diameter and percentage of voids of 50 V-anodized TNTs-Ti mesh versus time of anodization.

mesh Ti gauzes anodized for anodization times ranging from 1 to 16 h. The percentage of voids was quite constant until 5 h and strongly diminished at 7 h. The role of these structural properties on the ability of TiO_2 to perform water photo-oxidation will be discussed later in this chapter.

The crystallinity of TNTs-Ti mesh was investigated by XRD as shown in Figure 5.3. Annealing at 450°C, induced crystallinity to the amorphous nanotubes formed after the anodic oxidation of Ti gauze.[41] For all the samples, only the anatase phase of TiO_2 was present and no rutile phase was detected. The dominant diffraction peak at 25.3° can be assigned to the (101) plane of anatase TiO_2 (JCPDS 21-1272), indicating a highly crystalline anatase phase for the annealed TiO_2 nanotubes on Ti mesh. As in the case

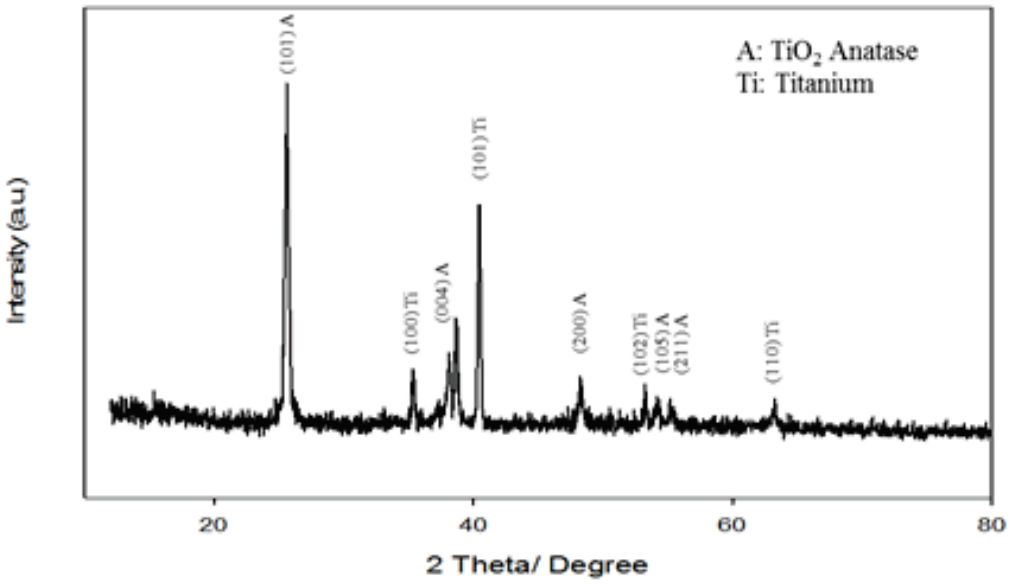

Figure 5.3 XRD pattern of 50 V-anodized TNTs-Ti mesh anodized for 5 h and annealed at 450°C.

of TiO_2 anatase nano powder a predominance of (101) can be expected for TiO_2 nanotubes annealed at 450°C following the Wulff construction.[42] This also suggests that nanotubes with (101) crystal plane are highly photo-stable when compared to (100) and (001) planes, due to its lower surface energy (0.44 J/m^2).[43] The XRD pattern also shows that part of the metallic Ti was not oxidized after the anodization (i.e. the internal part of the wires), which can thus act as a conductive mesh for the collection of the electrons (which are then transported to the cathode side through an external circuit).

5.2.2 Electronic properties of TNTs-Ti mesh

The TNTs-Ti mesh samples were characterized by UV-Vis diffuse reflectance spectroscopy to evaluate their light absorption properties. Figure 5.4 shows the spectrum for the 1 h-anodized mesh sample, the corresponding spectrum of a planar TNTs-Ti foil anodized under the same experimental conditions (50 V, 1 h) and the spectrum obtained from commercial TiO_2 P25 Degussa.

All the spectra exhibit a strong absorption in the UV region related to the intrinsic inter-band transition absorption of TiO_2.[44] However, while TiO_2 P25 Degussa only absorbs light in the ultraviolet region, TNTs-Ti mesh evidences a broad absorption band extending to the whole visible region. A similar behaviour can be seen also for the planar TNTs-Ti photo-anode, but in this case the broad visible peak is centred at about 580-600 nm. It has been known that TNTs-Ti planar systems developed by anodic oxidation and featuring ordered arrays of titania nanotubes show an intense absorption in the visible region, as they behave like 2D-type photonic materials[45,46] with the broad absorption related to light diffraction and scattering phenomena. The

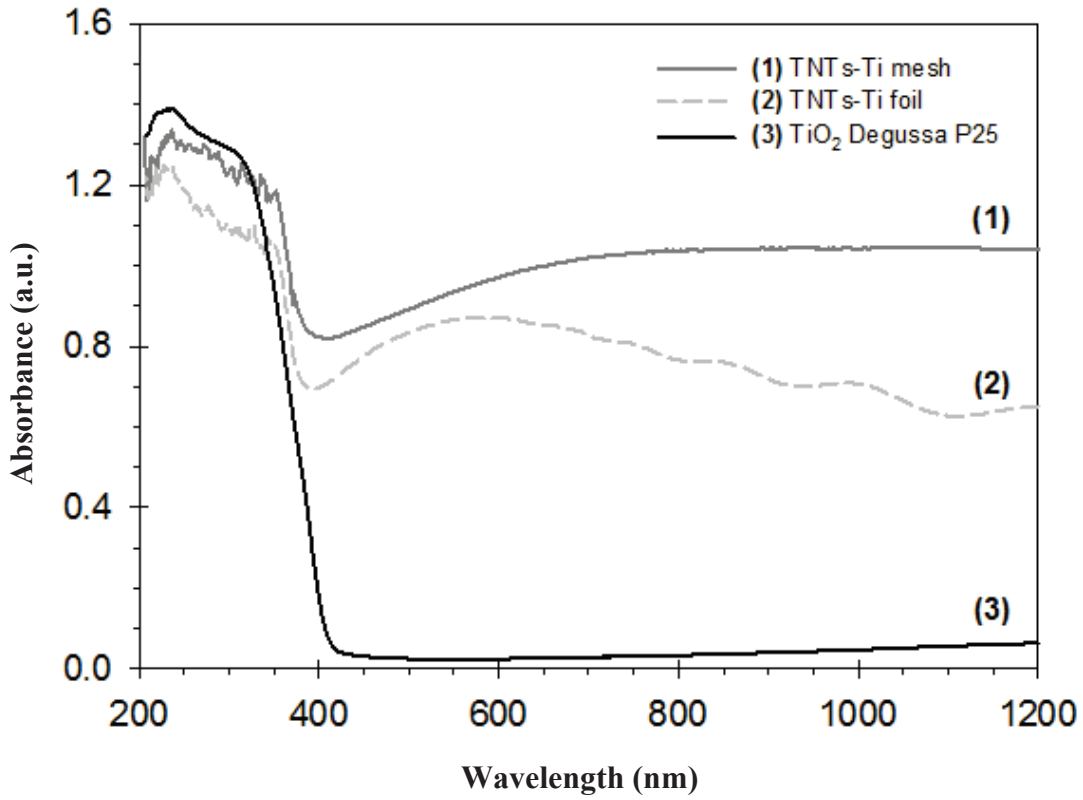

Figure 5.4 UV-visible diffuse reflectance spectra of TNTs-Ti mesh (**1**) in comparison with a planar-type TNTs-Ti photoanode (**2**) (both anodized at 50 V for 1 h) and TiO_2 P25 Degussa (**3**).

UV absorption band cantered at 580-600 nm is broader for the TNTs-Ti mesh than for the Ti foil and the P25 powder. While there is no dedicated literature addressing this phenomena for 3D structures like ours, state of the art on the 2D material suggests that this broader band in the UV is due to structural resonance effects.[2] Variation of the nano-architecture along the third dimension with respect to the planar-type TNTs-Ti could further reinforce such phenomenon (3D vs 2D).

The length of the TNTs (i.e. the thickness of the photoactive layer) can strongly influence light harvesting properties of the photoanodes.[36] In order to evaluate the actual absorbed light irradiance of the TNTs-Ti meshes, a transparent membrane composed of TNTs was necessary. Passalacqua *et. al.*[47] reported a three step anodic oxidation method to prepare self-standing TNTs membranes with no residual Ti foils. We used a similar method to prepare three planar-type TNTs-Ti electrodes (since the procedure was not feasible for TNTs from Ti mesh) by anodic oxidation, using the same synthetic conditions adopted for the gauzes (same electrolyte, same voltage: 50 V) but stopping the anodization at three different times (1h, 3h and 5h). After the anodization, the TNTs layers were detached from the metallic non-oxidized Ti layer in order to obtain TNTs transparent membranes. The SEM images of the three samples indicated the average TNTs lengths of 1.3, 2.9 and 5.8 μm for 1h, 3h and 5h samples respectively (consistently with the expected behaviour correlating anodization time and nanotubes length). A probe of a spectroradiometer (Lot Oriel, model ILT950) was located behind the TNTs membranes to measure the light transmittance. TNTs obtained after anodic oxidation of 1h (1.3 μm TNTs length by SEM) a corresponding transmitted light irradiance value of 0.059 W/cm^2 was observed. The same procedure was repeated for other TNTs-Ti membranes. The resulting transmitted light irradiance values were plotted versus the TNT length in Figure 5.5. The point at 0 μm corresponds to the incident light irradiance from the lamp (0.135 W/cm^2) obtained with no sample. As the procedure of TNTs detachment is not feasible for TNTs-Ti mesh, we evaluated the transmitted light irradiance by interpolation using the plot of Figure 5.5 obtained for the planar-type TNTs membranes. Using the plot of Figure 5.5 we found (for 2.5 μm) a corresponding transmitted light irradiance value of .059 W cm^{-2}. The same procedure was performed for the other TNTs- Ti meshes.The transmitted light irradiance values are reported in Table 5.2. The absorbed light irradiance values were calculated by subtracting the transmitted light irradiance values from 0.135 W/cm^2 (i.e.

the transmitted light irradiance with no sample). The light absorption initially increases with the anodization time and attains a maxima above which the heightening in the length of the nanotubes does not increase the light absorption.

Table 5.2 Transmitted light irradiance obtained by interpolation of plot in Figure 5.5 for Ti meshes anodized for different durations. Absorbed light irradiation was calculated by subtracting the corresponding transmitted light irradiance value from 0.135 W/cm^2 (transmitted light irradiance with no sample).

Sample	*Transmitted light Irradiance (W/cm^2)*	*Absorbed light Irradiance Irr (W/cm^2)*
No sample	0.1350	0
TNTs-Ti 20 min	0.0775	0.0575
TNTs-Ti 45 min	0.0637	0.0713
TNTs-Ti 1 h	0.0590	0.0760
TNTs-Ti 3 h	0.0509	0.0841
TNTs-Ti 4 h	0.0505	0.0845
TNTs-Ti 5 h	0.0504	0.0846
TNTs-Ti 7 h	0.0504	0.0846

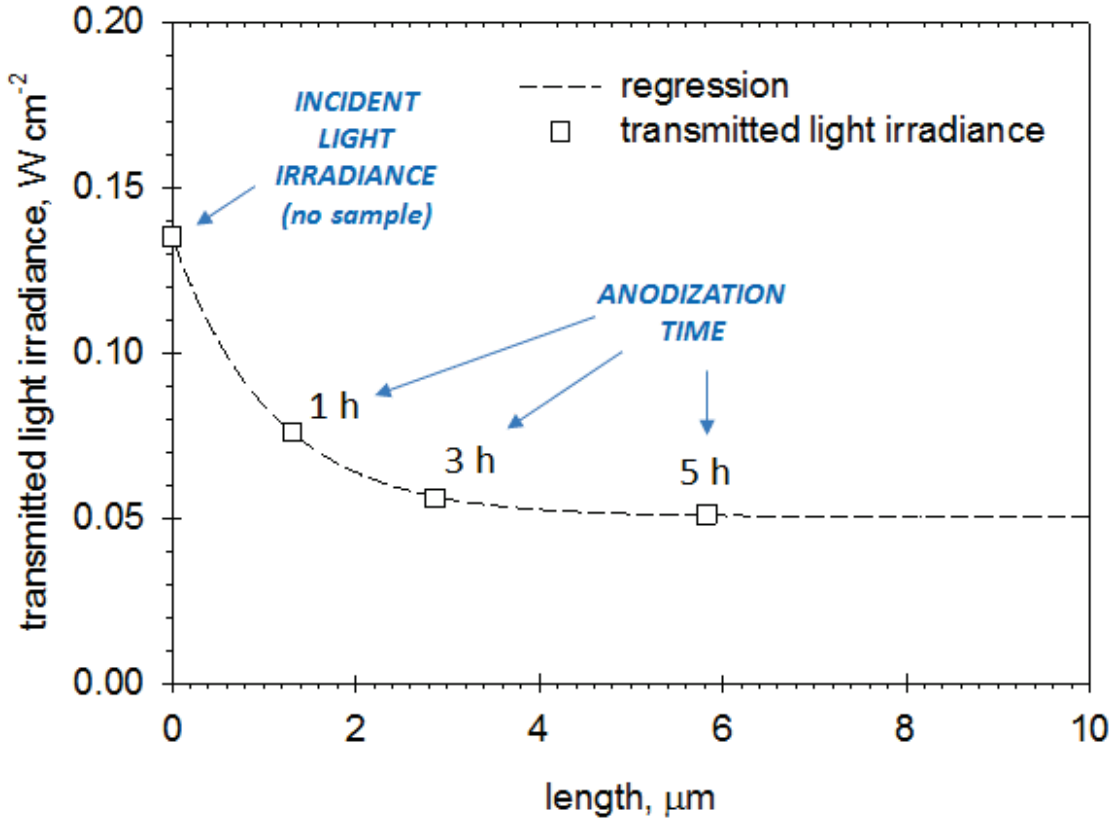

Figure 5.5 Plot of transmitted light irradiance vs. length of TNTs, obtained by irradiating planar-type TNTs membranes (prepared at different anodization times) after detachment from the non-oxidized Ti layer. The point at 0 μm corresponds to the incident light irradiance from the lamp (0.135 W/cm^2) obtained with no sample.

The plot suggests the flattening out of the irradiance for the seven samples (Table 5.2) and correlate the anodization time and the transmitted irradiance to the TNTs length.

5.2.3 Photo-current measurements

The TNTs grown on Ti meshes for different anodization times were exposed to light irradiation for chronoamperometric measurements, using an electrochemical cell with a three-electrode configuration as described in Chapter 2.

Figure 5.6 shows the obtained current density vs. time profiles. The sharp increase and decrease of current with light ON/OFF is due to the optical absorption and formation of electron–hole pairs indicating the photoelectrochemical activity of TNTs.[48] The samples were first subjected to four cycles of ON/OFF illumination without applying any filter showed a quick recovery to the original photocurrent values. The highest

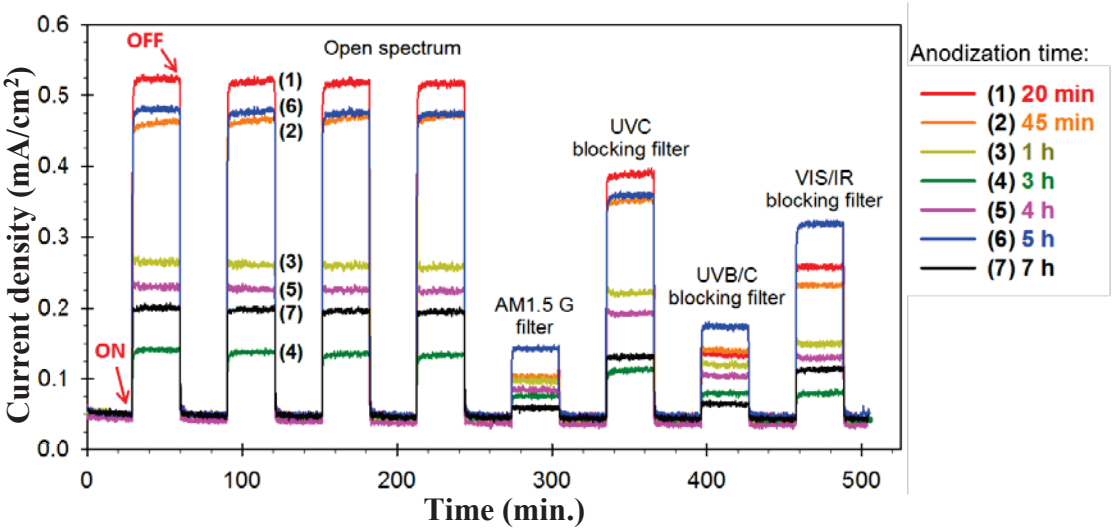

Figure 5.6 Chronoamperometric measurements for TNTs-Ti meshes prepared at different anodization times (0.1 V vs. Ag/AgCl, 1 M KOH).

value of photocurrent was obtained for the 20 min-anodized sample (0.53 mA/cm^2). The order of photocurrent activity in open spectrum was: 20 min > 5 h > 45 min > 1 h > 7 h > 3 h. The TNTs-Ti (open spectrum), evidencing reproducible and instantaneous rises in photocurrent followed meshes were then irradiated selecting different wavelength regions by using the filters. In presence of the UVC filter, the same order was observed. For the AM 1.5 G, UV B/C and VIS/IR filters, however, the orders of photocurrent activity were different. A correlation between structural properties of TNTs-Ti mesh, photocurrent and its photo-oxidation efficiency can be established. This has been discussed in the next section.

5.2.4 Photocatalytic efficiency

TiO_2 nanotubes has been known mainly for its two properties i) Photo-reduction[49,50] (CO_2, N_2) and ii) Photo-oxidation[22,51] (H_2O). Amongst these, the photo-oxidation feature of TiO_2 is heavily explored *via* photoelectrocatalysis.[52] Photoelectrocatalysis involves oxidation of water to produce H_2 & O_2 in presence of light. We used the same

method to determine the photocatalytic efficiency of TNTs-Ti mesh anodized for different time intervals at similar potential (50 V). The TNTs-Ti gauzes were assembled with Nafion® and GDL and tested in the PEC device in the process of water photo-electrolysis. When the light source is turned on, O_2 is produced in the anodic chamber while the cathodic chamber produces H_2. As the half reactions occur on the surface of the electrodes, which are in direct contact with the proton conductive membrane, this configuration may strongly improve the mass transport and minimize the overpotential due to long-distance pathways for the charges in the electrolyte, as it usually occurs in conventional electrochemical cells.[53,54]

After an induction period of about 15 min, as an equilibrium needs to be created inside the cell[1], the production rates of hydrogen from the cathode side remained constant over the time range investigated (five hours of irradiation). The hydrogen evolution values are plotted in Figure 5.7a versus the anodization times, while Figure 5.7b shows the proportionality between H_2 evolution and photocurrent density values.

The structural properties of TNTs-Ti meshes strongly influences their performances in the PEC cell. Particularly, two opposing aspects greatly affect the behaviour of the photoanodes. Shankar *et. al.*[55] reported for planar-type TNTs-Ti electrodes that if the nanotubes are too long, the photo catalytic efficiency will suffer due to the recombination of charge carriers. This can explain the decrease of performances of TNTs-Ti meshes comparing the anodization times from 20 min to 3 h. However, it is also well-known that the inner diameter of TNTs plays a crucial role in determining the effective surface area for absorbing photons and performing water splitting. TNTs with higher inner diameter usually give best performances in PEC cells.[2,56]

In our case, the inner diameter was higher by increasing the anodization time, as already shown in Figure 5.2. This contributed to enhancement in the PEC cell performance for samples anodized for a duration of 5h when compared to the 3h sample. Therefore, the process is a competition between two physical parameters i) Length of TNTs and ii) Inner surface area of TNTs. These physical parameters can thus explain the minimum photocatalytic efficiency for Ti mesh anodized in 3h. However, the H_2 productivity diminished again for TNTs-Ti mesh anodized for 7 h, despite of the higher inner diameter. This result can be ascribed to the strong difference of the void percentage of the 7 h-anodized sample (Figure 5.2). Nguyen *et. al.*[4] recently reported the importance of voids in H_2 production. He showed that, increasing the

voids between nanotubes leads to an increase in surface area (as the outer walls of nanotubes are now accessible) and faster electron transport due to decrease in number

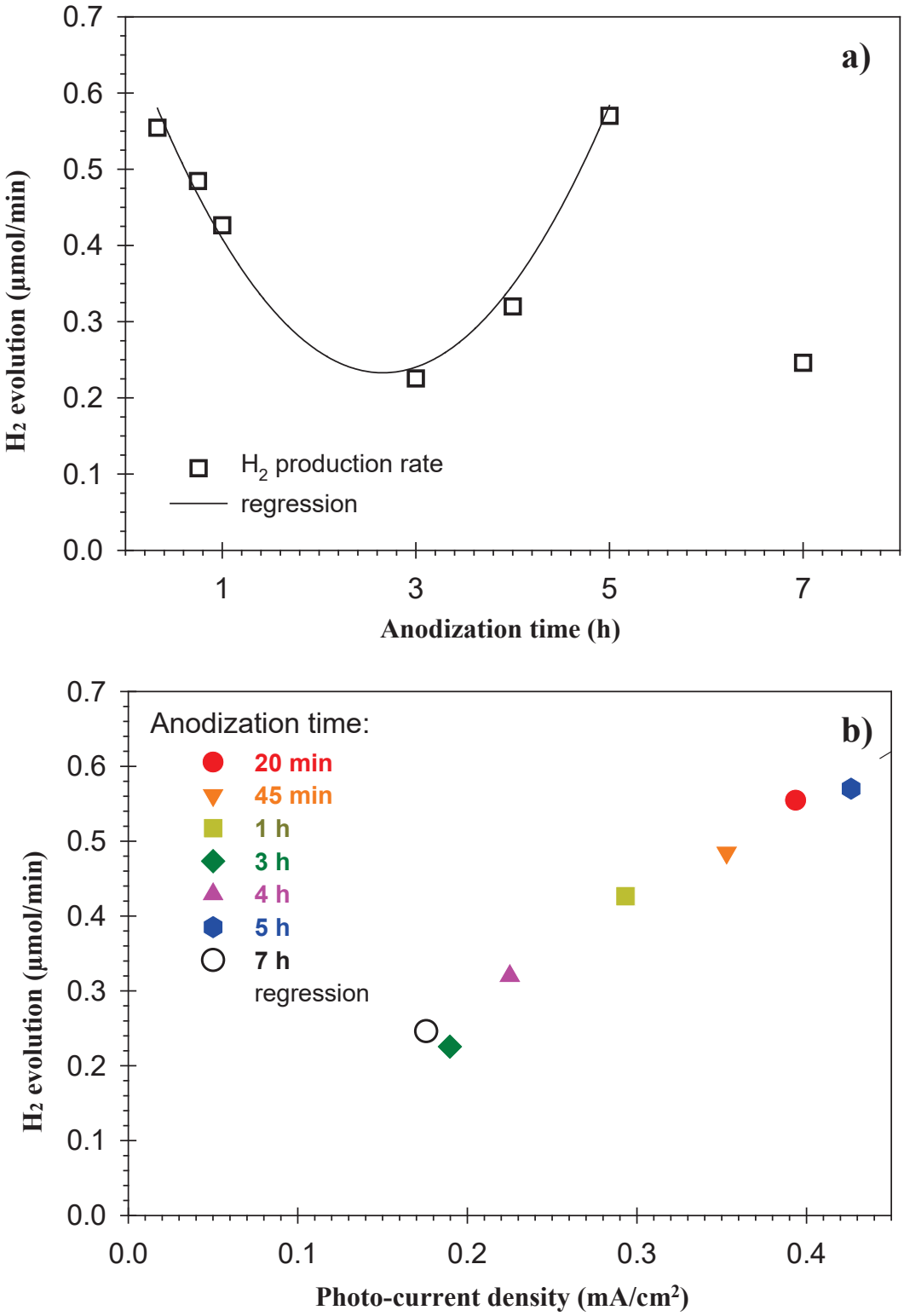

Figure 5.7 Hydrogen production (µmol/min) rate versus: a) anodization time (hours) with proposed regression curve and b) photo-current density (mA/cm^2) for TNTs-Ti meshes anodized at 50 V.

of contacts amongst TNTs thereby increasing the efficiency. In fact, especially in our case in bottom part of the nanotubes, the reduction of the surface angle of the Ti wires with the penetration during the anodization lead s to a decrease in the voids among the nanotubes. This leads to the formation of a number of contacts among the TNTs, which may act as sites for charge recombination. As a result, the H_2 productivity strongly diminished for higher anodization time *i.e.* 7h.

We also calculated the photoconversion efficiency (**PCE**) of different TNTs-Ti mesh's by using the following equation[57]:

$$PCE\ \% = \frac{R_{H2}\ *\ \Delta G^0}{Irr\ *A} * 100 \qquad \text{……. (Eq. 5.1)}$$

where, R_{H2} is the rate of hydrogen production (mol s^{-1}), ΔG^0 is the standard Gibbs energy at standard conditions (2.372 x 10^5 J/mol), *Irr* is the light irradiance (W/cm^2) and *A* is the irradiated area of the photocatalyst (cm^2). While we observed a maximum of H_2 production rate for the 5-h-anodized TNTs-Ti mesh, giving about 177 µmol in 5 h of light irradiation, the PCE was higher for the 20-min anodized sample. This is due to the lower absorbed light irradiance value for the 20-min anodized sample. All the H_2 production rate and PCE values are reported in Table 5.3.

Table 5.3 Hydrogen production rate and photoconversion efficiency (PCE) for TNTs-Ti meshes anodized at 50 V for different times.

Anodization time	***H_2 production rate (µmol/min)***	***PCE %***
20 min	0.55	0.67
45 min	0.48	0.47
1 h	0.43	0.39
3 h	0.23	0.19
4 h	0.32	0.26
5 h	0.57	0.47
7 h	0.25	0.20

Our system compares well with respect to the state of the art on Ti mesh based systems. Liu *et. al.*[58] reported 3-D vertically arrays of TiO_2 nanotubes on Ti meshes as efficient photoanodes for water photoelectrolysis, showing high photo-current density especially in presence of hole scavengers such as ethylene glycol. In our case, all the catalytic tests were carried out without applying any bias between the two electrodes (the energy needed for water splitting was supplied only from the lamp) and no sacrificial donors were added into the system to facilitate water oxidation. Zhou *et. al.*[59] studied the H_2 generation properties of TiO_2 nanotube arrays fabricated on Ti meshes. They reported a maximum rate of H_2 evolution of 4.6 L m^{-2} h^{-1} during the first hour of irradiation. However, the rate decreased to 1.2 L m^{-2} h^{-1} after five hour. In addition, they used Pt doped TiO_2 nanotubes in presence of tri-ethanolamine as sacrificial donor and the rate of H_2 evolution strongly diminished for the non-doped TiO_2 nanotube arrays (0.14 L m^{-2} h^{-1}). In our case, considering a constant H_2 generation of about 0.6 μmol/min for the best active TiO_2 nanotube gauze (Figure 5.7), by proper calculation we were able to obtain 1.4 L m^{-2} h^{-1} H_2 evolution rate (after 5 h of light irradiation) using bare (non-doped) TiO_2 nanotubes and without adding any sacrificial donors. This is a positive contribution to state of the art on continuous water photo-electrolysis processes for H_2 evolution. Simultaneously, we have proven that the catalytic activity of the catalyst is stable which means the surface states in TNTs regenerates in a continuous cycle.

Our attempts to characterize surface species of this TNTs-Ti mesh support were quenched by the fragility of the nanotubes. The compact design of the system also prevented us from obtaining the surface area of this system.

5.3 Conclusion

Hierarchical porous TiO_2 nanotube arrays (TNTs) were synthesized by controlled anodic oxidation of regularly woven Ti wires. The resulting 3D-type meso/macro structured Ti meshes were used as efficient photoanodes in a highly compact photo-electrocatalytic (PEC) device for the production of hydrogen. The water splitting was performed to recognise catalytic performance of such flexible TNTs-Ti mesh. The presence of a mesoporous structure (due to the ordered arrays of TiO_2 nanotubes) together with the macro pores of the gauze (36 % open area) assured good properties of both light absorption and charge transport, minimizing the overpotential phenomena that occurs due to proton diffusion from the anode to the cathode, which is one of the main drawbacks of PEC cells for the production of solar fuels.

Structural characterization data of TNTs-Ti meshes evidenced that: i) the TNTs layer was found to be in anatase phase for all the TNTs-Ti gauzes; ii) the increase of the applied voltage allowed to obtain nanotubes with higher length; iii) the parameters of inner diameter are related to space present on the surface of Ti during the growth of the tubes and is probably influenced by the acting electromagnetic field; iv) the samples anodized for longer times showed larger inner diameter but with higher tube length, that increased the probability of charge recombination and v) the presence of a nano-architecture in titania leads to an absorption peak in the visible region, due to light diffraction and scattering phenomena, not present in commonly prepared TiO_2 powder.

The essence of photo catalysis with TNTs-Ti meshes greatly depend on their structural properties. We found two main opposing aspects influencing the photo-activity: i) the inner diameter and ii) the length of TNTs. While the increase of the inner diameter with the anodization time improves H_2 productivity, longer nanotubes negatively influence the catalytic activity due to the increasing charge recombination phenomena. The result is an initial decreasing profile of H_2 evolution vs. anodization time, reaching a minimum at 3 h and then increasing again for the 5 h-anodized sample. However, a further increase of the anodization time to 7 h did not allow an improvement in H_2 productivity, due to the low percentage of voids (and the high number of contacts among the tubes) for longer nanotubes.

The TNTs-Ti mesh, in combination with a carbon-based GDL, can be a good candidate to be used as the photoactive substrate in a gas-phase system, due to its high porous

structure, as these specific “electrolyte-less” conditions were reported as advantageous for these kinds of process.[60] This suggests the versatility of such a system and is an added advantage. It would be interesting to explore, determine and take advantage of surface chemistry of TNTs by applying SOMC technique with or without linkers but on the contrary the dehydroxylation temperature (700°C) is not agreeable with the TNTs-Ti mesh system developed by anodization.

5.4 References

(1) Ampelli, C; Centi, G; Passalacqua, R; Perathoner, S. *Energy Environ. Sci.* **2010**, *3* (3), 253.

(2) Roy, P.; Berger, S.; Schmuki, P. *Angew. Chemie - Int. Ed.* **2011**, *50* (13), 2904–2939.

(3) Kontos, A. I.; Likodimos, V.; Stergiopoulos, T.; Tsoukleris, D. S.; Falaras, P.; Rabias, I.; Papavassiliou, G.; Kim, D.; Kunze, J.; Schmuki, P. *Chem. Mater.* **2009**, *21* (4), 662–672.

(4) Nguyen, N. T.; Ozkan, S.; Hwang, I.; Mazare, A.; Schmuki, P. *Nanoscale* **2016**, *8*.

(5) Passalacqua, R.; Ampelli, C.; Perathoner, S.; Centi, G. *Nanosci. Nanotechnol. Lett.* **2012**, *4* (2), 142–148.

(6) Mor, G. K.; Varghese, O. K.; Paulose, M.; Shankar, K.; Grimes, C. A. *Sol. Energy Mater. Sol. Cells* **2006**, *90* (14), 2011–2075.

(7) Tomoko Kasuga; Masayoshi Hiramatsu; Akihiko Hoson; Toru Sekino, and; Niihara, K. *Langmuir* **1998**, *14* (12), pp 3160–3163.

(8) Sander, M. S.; Côté, M. J.; Gu, W.; Kile, B. M.; Tripp, C. P. *Adv. Mater.* **2004**, *16* (22), 2052–2057.

(9) Kasuga, T.; Hiramatsu, M.; Hoson, A.; Sekino, T.; Niihara, K. *Adv. Mater.* **1999**, *11* (15), 1307–1311.

(10) Du, G. H.; Chen, Q.; Che, R. C.; Yuan, Z. Y.; Peng, L.-M. *Appl. Phys. Lett.* **2001**, *79* (22), 3702–3704.

(11) Adachi, M.; Murata, Y.; Harada, M.; Yoshikawa, S. *Chem. Lett.* **2000**, *29* (8), 942–943.

(12) Adachi, M.; Murata, Y.; Okada, I.; Yoshikawa, S. *J. Electrochem. Soc.* **2003**, *150* (8), 488.

(13) Lakshmi, B.B; Dorhout, P.K.; Martin, C. R. *Chem. Mater.* **1997**, *9* (3), pp 857–862.

(14) Nakato, Y.; Akanuma, H.; Shimizu, J.-I.; Magari, Y. *J. Electroanal. Chem* **1995**, *396*, 35–39.

(15) Sugiura, T.; Yoshida, T.; Minoura, H. *Electrochem. Solid-State Lett.* **1999**, *1* (4), 175.

(16) Zhang, M.; Bando, Y.; Wada, K. *J. Mater. Sci. Lett.* **2001**, *20* (2), 167–170.

(17) Shin, H.; Jeong, D.-K.; Lee, J.; Sung, M. M.; Kim, J. *Adv. Mater.* **2004**, *16* (14), 1197–1200.

(18) Knez, M.; Nielsch, K.; Niinistö, L. *Adv. Mater.* **2007**, *19* (21), 3425–3438.

(19) Leskelä, M.; Ritala, M. *Angew. Chemie* **2003**, *115* (45), 5706–5713.

(20) Zlamal, M.; Macak, J. M.; Schmuki, P.; Krýsa, J. *Electrochem. commun.* **2007**, *9* (12), 2822–2826.

(21) Macak, J. M.; Tsuchiya, H.; Berger, S.; Bauer, S.; Fujimoto, S.; Schmuki, P. *Chem. Phys. Lett.* **2006**, *428* (4–6), 421–425.

(22) Passalacqua, R.; Perathoner, S.; Centi, G. *Catal. Today* **2015**, *251*, 121–131.

(23) Ampelli, C.; Genovese, C.; Centi, G.; Passalacqua, R.; Perathoner, S. *Top. Catal.* **2016**, *59* (8–9), 757–771.

(24) Pozio, A.; Carewska, M.; Mura, F.; D'Amato, R.; Falconieri, M.; De Francesco, M.; Appetecchi, G. B. *J. Power Sources* **2014**, *247*, 883–889.

(25) Bao, Z.; Xie, H.; Rao, J.; Chen, L.; Wei, Y.; Li, H.; Zhou, X. *Mater. Lett.* **2014**, *124*, 158–160.

(26) He, W.; Qiu, J.; Zhuge, F.; Li, X.; Lee, J.-H.; Kim, Y.-D.; Kim, H.-K.; Hwang, Y.-H. *Nanotechnology* **2012**, *23* (22), 225602.

(27) Li, Y.; Yu, H.; Song, W.; Li, G.; Yi, B.; Shao, Z. *Int. J. Hydrogen Energy* **2011**, *36* (22), 14374–14380.

(28) Liao, J.; Lin, S.; Zhang, L.; Pan, N.; Cao, X.; Li, J. *ACS Appl. Mater. Interfaces* **2012**, *4* (1), 171–177.

(29) Ojeda, M.; Grau-Atienza, A.; Campos, R.; Romero, A. A.; Serrano, E.; Maria Marinas, J.; García Martínez, J.; Luque, R. *ChemSusChem* **2015**, *8* (8), 1328–1333.

(30) Besser, B.; Tajiri, H. A.; Mikolajczyk, G.; Möllmer, J.; Schumacher, T. C.; Odenbach, S.; Gläser, R.; Kroll, S.; Rezwan, K. *ACS Appl. Mater. Interfaces* **2016**, *8* (5), 3277–3286.

(31) Ampelli, C.; Genovese, C.; Passalacqua, R.; Perathoner, S.; Centi, G. *Appl. Therm. Eng.* **2014**, *70* (2), 1270–1275.

(32) Tao, H.; Yang, H.; Liu, X.; Ren, J.; Wang, Y.; Lu, G. *Chem. Eng. J.* **2013**, *225*, 686–694.

(33) Na, K.; Somorjai, G. A. *Catal. Letters* **2015**, *145* (1), 193–213.

(34) Serrano, D. P.; Escola, J. M.; Pizarro, P. *Chem. Soc. Rev.* **2013**, *42* (9), 4004–4035.

(35) Lynch, R. P.; Ghicov, A.; Schmuki, P. *J. Electrochem. Soc.* **2010**, *157* (3), G76.

(36) Ampelli, C.; Tavella, F.; Perathoner, S.; Centi, G. *Chem. Eng. J.* **2017**, *320*, 352–362.

(37) Juang, Y.; Liu, Y.; Nurhayati, E.; Thuy, N. T.; Huang, C.; Hu, C. C. *Chemosphere* **2016**, *144*, 2462–2468.

(38) Alivov, Y.; Pandikunta, M.; Nikishin, S.; Fan, Z. Y. *Nanotechnology* **2009**, *20* (22), 225602.

(39) Ng, S. W.; Yam, F. K.; Beh, K. P.; Tneh, S. S.; Hassan, Z. *Optoelectron. Adv. Mater. Rapid Commun.* **2011**, *5* (3), 258–262.

(40) Liu, Z.; Subramania, V. R.; Misra, M. *J. Phys. Chem. C* **2009**, *113* (31), 14028–14033.

(41) Li, Y.; Yu, H.; Zhang, C.; Song, W.; Li, G.; Shao, Z.; Yi, B. *Electrochim. Acta* **2013**, *107*, 313–319.

(42) Arrouvel, C.; Digne, M.; Breysse, M.; Toulhoat, H.; Raybaud, P. *J. Catal.* **2004**, *222* (1), 152–166.

(43) Lazzeri, M.; Vittadini, A.; Selloni, A. *Phys. Rev. B* **2002**, *65* (11), 119901.

(44) Mollavali, M.; Falamaki, C.; Rohani, S. *Int. J. Hydrogen Energy* **2015**, *40* (36), 12239–12252.

(45) Li, P.; Chen, S.-L.; Wang, A.-J.; Wang, Y. *Chem. Eng. J.* **2016**, *284*, 305–314.

(46) Centi, G.; Passalacqua, R.; Perathoner, S.; Su, D. S.; Weinberg, G.; Schlögl, R. *Phys. Chem. Chem. Phys.* **2007**, *9* (35), 4930.

(47) Passalacqua, R.; Ampelli, C.; Perathoner, S.; Centi, G. *Chem. Eng. Trans.* **2014**, *41*, 319–324.

(48) Wang, J.; Xu, G.; Zhang, X.; Lv, J.; Wang, D.; Zheng, Z.; Wang, J.; Wu, Y. *New J. Chem. New J. Chem* **2015**, *39* (39), 9019–9027.

(49) Hoshino, K.; Kuchii, R.; Ogawa, T. *Appl. Catal. B Environ.* **2008**, *79* (1), 81–88.

(50) Anpo, M.; Chiba, K. *J. Mol. Catal.* **1992**, *74* (1–3), 207–212.

(51) Leung, D. Y. C.; Fu, X.; Wang, C.; Ni, M.; Leung, M. K. H.; Wang, X.; Fu, X. *ChemSusChem* **2010**, *3* (6), 681–694.

(52) Ni, M.; Leung, M. K. H.; Leung, D. Y. C.; Sumathy, K. *Renew. Sustain. Energy Rev.* **2007**, *11* (3), 401–425.

(53) Sun, Y.; Wang, G.; Yan, K. *Int. J. Hydrogen Energy* **2011**, *36* (24), 15502–15508.

(54) Bosserez, T.; Rongé, J.; van Humbeeck, J.; Haussener, S.; Martens, J. *Oil Gas Sci. Technol. – Rev. d'IFP Energies Nouv.* **2015**, *70* (5), 877–889.

(55) Karthik, S.; Gopal, K. M.; Haripriya, E. P.; Sorachon, Y.; Maggie, P.; Oomman, K. V.; Craig, A. G. *Nanotechnology* **2007**, *18* (6), 65707.

(56) Mohamed, A. M.; Aljaber, A. S.; AlQaradawi, S. Y.; Allam, N. K. *Chem. Commun. (Camb).* **2015**, *51* (63), 12617–12620.

(57) Varghese, O. K.; Grimes, C. A. *Sol. Energy Mater. Sol. Cells* **2008**, *92*, 374–384.

(58) Liu, Z.; Zhang, Q.; Zhao, T.; Zhai, J.; Jiang, L. *J. Mater. Chem.* **2011**, *21* (28), 10354.

(59) Zhou, R.; Kang, S.-Z.; Li, X.; Wang, L.; Qin, L.; Mu, J. *RSC Adv.* **2015**, *5* (9), 6954–6961.

(60) Ampelli, C.; Genovese, C.; Marepally, B. C.; Papanikolaou, G.; Perathoner, S.; Centi, G. *Faraday Discuss.* **2015**, *183* (0), 125–145.

Conclusions and Perspectives

General Summary

Surface organometallic chemistry (SOMC) demonstrates an ability to bridge the gap between homogeneous and heterogeneous catalysts by designing well-defined single site heterogeneous surface complexes. These well-defined catalysts able to catalyze various reactions for instance alkane metathesis, olefin metathesis, alkene polymerization etc. are on the stable or thermo-reductable supports (SiO_2, Al_2O_3, CeO_2). Although remarkable, most of these applications are driven by fossil to fossil conversion. The ongoing energy transition demands alteration of current industrial chemical production, which is heavily reliant on fossil fuels as its primary feedstock to move to an industrial chemical production scenario contingent on "Solar driven chemistry"; a renewable energy driven chemistry.

As one of the most well-established photocatalyst, we have identified TiO_2 as an unique support for solar driven SOMC. Although few literature precedents have been reported in the field of TiO_2 SOMC, little (if any) data on the characterization of the support from a SOMC perspective is available.

Therefore, the challenge of this thesis was to determine qualitatively and quantitatively the surface species present on the surface of TiO_2 anatase and investigate the usefullness of SOMC to develop well-defined catalysts.

In **Chapter 3**, TiO_2 anatase from different commercial sources were calcined at 450°C under air followed by dehydroxylation at 700°C under UHV to obtain partially dehydroxylated titania support, $TiO_{2(700)}$. Techniques such as XRD, HRTEM, DRIFT, EPR, chemical titration with n-*Bu*Li and FTIR identified qualitatively and quantitatively the presence of 0.7 OH/nm^2 or 0.064 mmol OH/g of surface hydroxyls and coordinated water present on the predominant facet (101) along with (001) and (100) crystal planes of $TiO_{2(700)}$. Paramagnetic activity was caused due to the presence of oxygen vacancies and "Ti^{3+}" ions in very low concentration in the bulk of the solid thus having an activated surface with no surface electron mobility. Apart from surface hydroxyls and coordinated water, the surface of $TiO_{2(700)}$ also consisted of strong lewis acidic sites (Ti_{5c}) and weak bronsted basic sites (O_{2c}).

Once the surface was fully characterized $Ta[-CH_2C(CH_3)_3]_3[=CHC(CH_3)_3]$ (**1**) was used as a grafting organometallic precursor due to its well-defined chemistry and identified entities on silica. Complex (**1**) was grafted on surface of $TiO_{2(700)}$ as

monitored by gas release, elemental analysis, EPR and DRIFT spectroscopy suggesting the formation of a monopodal species. An increase in the paramagnetic activity of the resultant solid was attributed to the presence of surface Ti^{3+} ions generated by grafting of the organometallic precursor. Such unexpected results suggests that SOMC grafting on TiO_2 induces a "self-doping" mechanism on the surface of anatase probably due to oxygen insertion in Ta—C bond, thus creating mobile anionic vacancies. The presence of paramagnetism altered the outcome of other characterization techniques thus making it difficult to identify the grafted species.

In order to simplify the surface chemistry (**Chapter 4**), 2-methyl imidazole or 2-mIm was investigated as a coordinating ligand to take advantage of surface lewis acidity and create a homogeneous surface consisting of bronsted acidity from 2-mIm. A loading of 3.5 2-mIm/nm^2 was determined by elemental analysis which was stable at high temperatures suggesting a chemisorbed behaviour of the linker. ^{13}C CP MAS NMR clearly indicated the presence of 2-mIm on $TiO_{2(700)}$ after removing the excess at 200°C under UHV. Further studies are required to have an in-depth understanding of this interaction before to explore this support for SOMC of organometallics.

In **Chapter 5**, a TiO_2 nanotubes (TNTs) based solid film was developed as an advantageous alternative to the powder supports. Using anodic oxidation TiO_2 nanotubes were grown on Ti mesh with a 36% open area. The resultant system displayed both meso and macro porosity due to the porous nanotubes and 80 mesh size of the gauze respectively. The meso-macro porosity of the system helped in faster proton diffusion to the cathode through the PEM thereby decreasing the loss of activity. Different duration and potential were examined to understand the nanotubes growth pattern and find the preeminent photocatalytic performing conditions. Ti mesh anodized for 5h at 50V showed the highest H_2 productivity during a 5h run with a constant water splitting. TNTs-Ti mesh based solid support developed resulted an improvement in H_2 production with respect to state of the art TNT gauze.

Perspectives

The first perspective of this work is to aim at successfully combine single atom heterogeneous catalysis (SAC) and photocatalysis. The tantalum-titania chemistry performed through SOMC route can provide some intriguing insights into MMCT mechanisms as well as propagation of surface reduction sites. As such simply, SOMC

has the ability to produce isolated sites such that the surface grafted metal sites acts as single atom catalysts (SAC).[1] One such example is the dinitrogen reductive clevage using supported (isolated) tantalum atoms prepared by SOMC.[2,3]

A second perspective is to actually circumvent the hurdles (but also opportunities) of transition metal SOMC on TiO_2 mentioned above. Therefore, grafting 2-mIm as surface bound linker could ease which is tantamount to developing an adequate interlayer between TiO_2 and organometallic grafting by SOMC. This system can also be a stepping stone to take advantage of an auto-assembled microporous structure that are known to yield ZIF (metal-organic frameworks).[4,5]

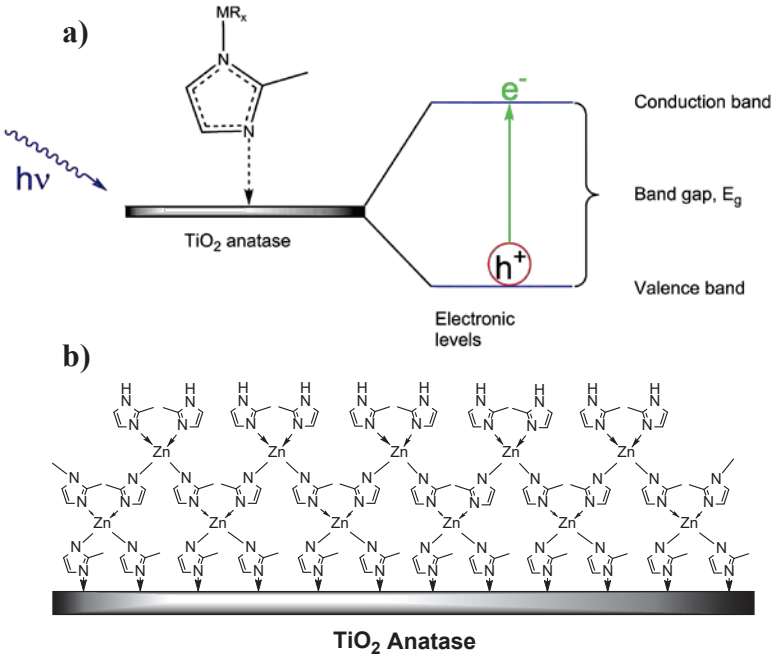

Figure 6.1 Schematic representation of a) Organometallic precursor grafted on 2-mIm coordinated TiO_2 and b) Formation of an auto-assembled metal-organic framework (ZIF-8) on TiO_2 anatase.

From Chapter 5, we learned that nano-engineered structures such as TiO_2 nanotubes on a Ti mesh are easy to prepare, have higher efficiency compared to titania nanopowder and are easy to integrate into the current state of the art PEC devices. Therefore, although TiO_2 anatase nanopowder provides an easy access to all characterization tools once studied, it would be interesting to develop SOMC techniques on TNT's-Ti mesh systems to eventually create a new line of well-defined photocatalysts that can be integrated easily into PEC devices.

References

(1) Yang, X. F.; Wang, A.; Qiao, B.; Li, J.; Liu, J.; Zhang, T. *Acc. Chem. Res.* **2013**, *46* (8), 1740–1748.

(2) Avenier, P.; Taoufik, M.; Lesage, A.; Solans-Monfort, X.; Baudouin, A.; de Mallmann, A.; Veyre, L.; Basset, J.-M.; Eisenstein, O.; Emsley, L.; Quadrelli, E. A. *Science.* **2007**, *317* (5841), 1056-1060.

(3) Basset, J.-M., Psaro, R., Roberto, D., Ugo, R., Eds.; *Modern Surface Organometallic Chemistry*; Wiley-VCH Verlag GmbH & Co. KGaA: Weinheim, Germany, 2009.

(4) Xu, F.; Kou, L.; Jia, J.; Hou, X.; Long, Z.; Wang, S. *Anal. Chim. Acta.* **2013**, *804*, 240–245.

(5) Stassen, I.; Styles, M.; Grenci, G.; Gorp, H. Van; Vanderlinden, W.; Feyter, S. De; Falcaro, P.; Vos, D. De; Vereecken, P.; Ameloot, R. *Nat. Mater.* **2016**, *15* (3), 304–310.

Annex

Annex I

Density Function Theory (DFT) method

The DFT calculations were performed by Dr Frédéric Lefebvre at C2P2, CPE Lyon. A surface model was built starting from the X-ray structure of anatase. This model contains the Ti-OH group and the first and second coordination spheres around titanium (oxygen atoms and second Ti neighbours). The coordination of the Ti atoms of the second coordination sphere are completed by Fluorine atoms located along the Ti-O bonds and at a distance of 1.9 Å (mean value deduced from an optimization of the Ti-F distance in smaller clusters). The method used is B3LYP with the LanL2DZ pseudopotential on Ti and the 6-31+G* basis for O, F and H. In a first step optimization of the positions of the O and H atoms of the hydroxyl group, all other atoms being kept frozen. Calculation of IR frequencies by use of the same method. The calculations were carried out on 3 different TiO_2 planes i.e. (101), (100) and (001) respectively using B3LYP method with the LanL2DZ pseudopotential on Ti and the 6-31+G* basis for O, F and H. The IR frequencies were also calculated by same method.

Hydroxyl group on TiO_2 (001)

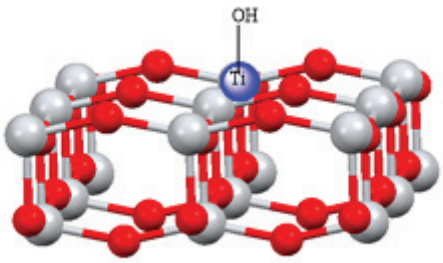

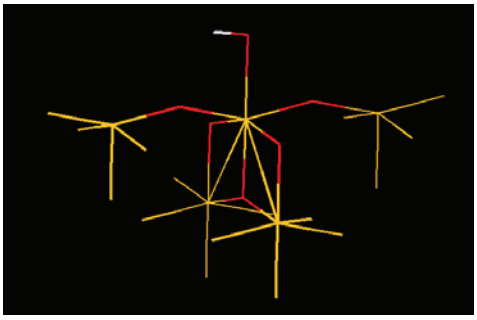

Geometrical parameters after optimization:

Ti-O:	2.13976 Å
O-H:	0.97123 Å
Ti-O-H:	96.448°
IR frequency:	3738.4 cm^{-1}
Intensity:	1.04

Water molecule on TiO_2 (100)

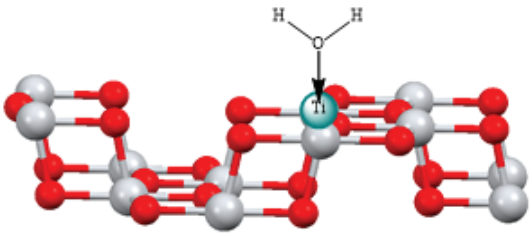

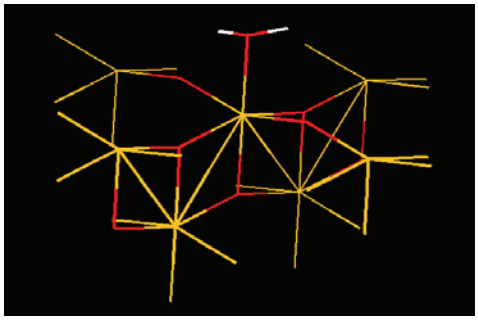

The optimization leads to a different structure where water is not coordinated to titanium but to two adjacent oxygen atoms via hydrogen bonds:

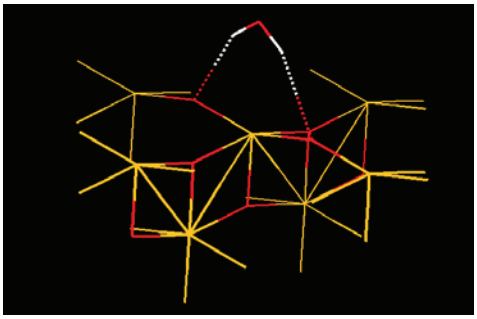

This is probably related to the strained structure chosen for TiO_2 (100).

Hydroxyl group on TiO_2 (100)

We then looked into the possibility of one hydroxyl group instead of the coordinated water molecule on hexacoordinated Ti(IV). In this case the structure was optimized.

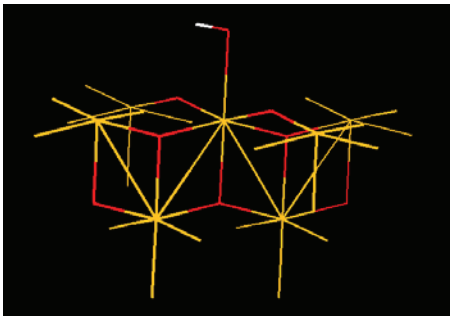

Geometrical parameters after optimization:

Ti-O:	2.18082 Å
O-H:	0.97422 Å

Ti-O-H: 97.632°

IR frequency: 3715 cm^{-1}

Intensity: 0.67

Hydroxyl group on TiO_2 (101)

The structure cannot be optimized probably due to the number of Ti atoms and the charge.

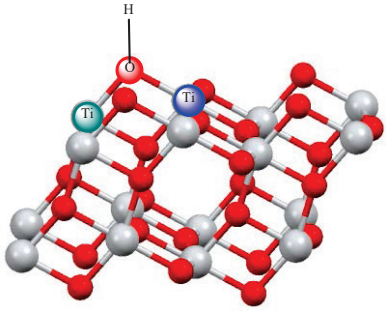

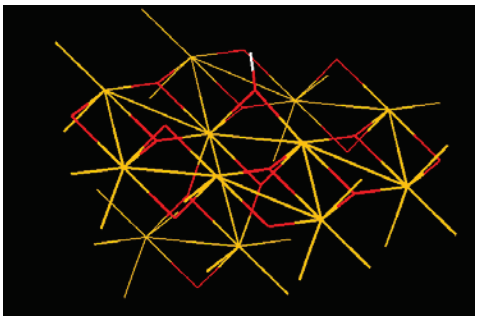

Calculations with the STO-3G basis set for all atoms

For the hydroxyl group on the 001 and 101 faces the optimization leads to the expected structure. For the water molecule on the 100 face the optimization leads to the formation of two hydroxyl groups, one on the starting Ti and one on an adjacent bridging oxygen:

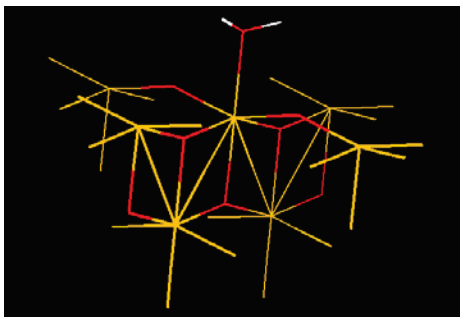

Starting Geometry

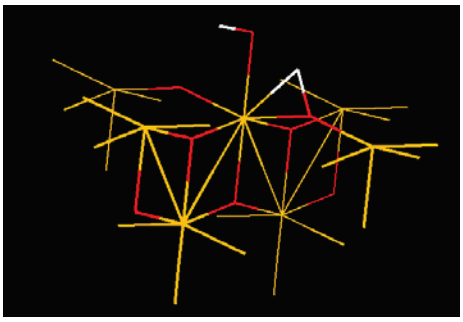

Final Geometry

Note that the position of the bridging oxygen atom where is located the proton has not been optimized. As a consequence the values for the corresponding hydroxyl group should be taken with care.

Group	*d(O-H) (Å)*	*d(Ti-O) (Å)*	*Ti-O-H (°)*	*δ(OH) (cm^{-1})*	*Intensity*	*Intensity normalized*
Hydroxyl group on TiO_2 (001)	1.0422	2.0815	99.95	3425	227	1.00
Hydroxyl group on TiO_2 (101)	1.0141	1.9310 2.0822	135.77 125.79	3694	143	0.63
terminal OH on TiO_2 (100)	1.027	2.0339	97.82	3636	102	0.45
Bridging OH on TiO_2 (100)	1.1243	1.9301 1.9301	77.57 125.06	2268	797	

Annex II

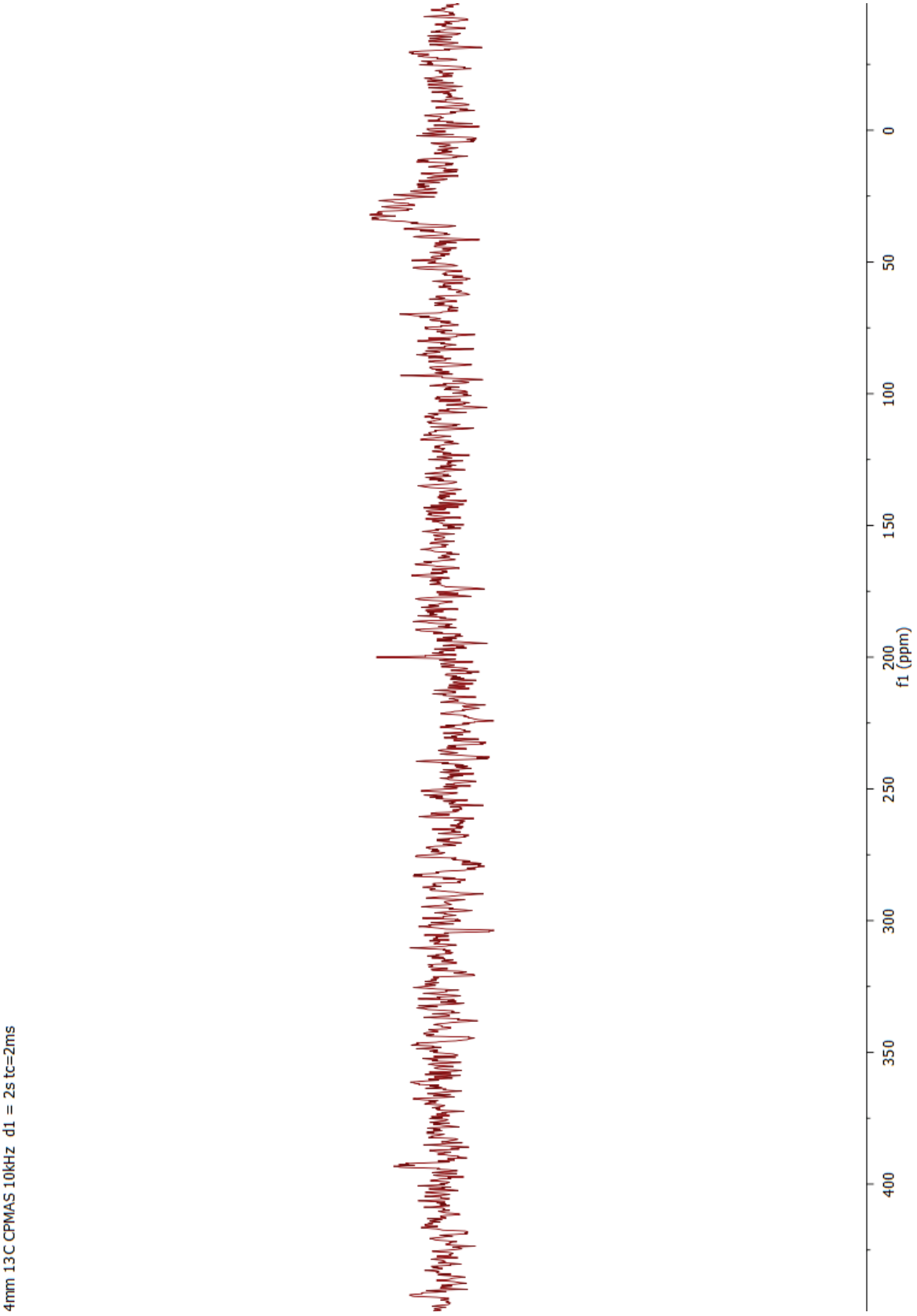
4mm 13C CPMAS 10kHz d1 = 2s tc=2ms
0
50
100
150
200
250
300
350
400
f1 (ppm)

Annex III

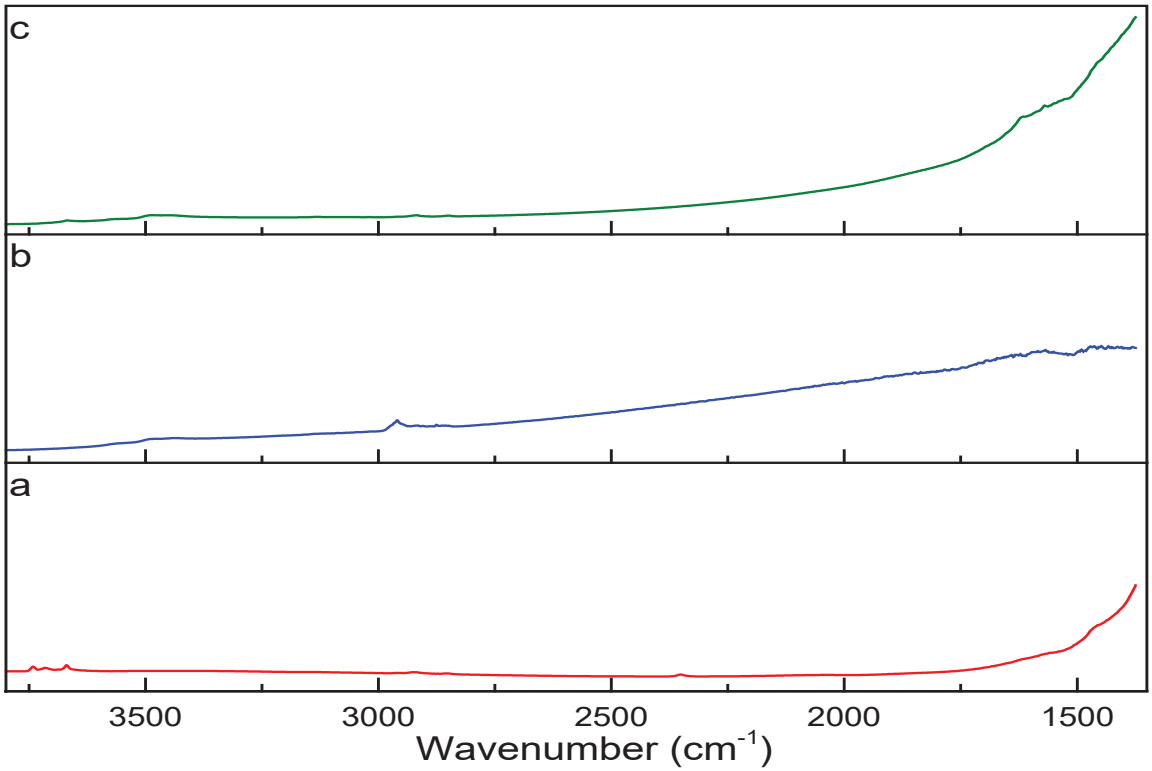

DRIFT spectra of TiO_2 anatase a) after dehydroxylating at 700°C under UHV for 12h b) after Ta[-$CH_2C(CH_3)_3$]$_3$[=$CHC(CH_3)_3$] grafting on $TiO_{2(700)}$ solid (**4b**) and c) after exposing solid (**4b**) to water vapours and dehydroxylating at 200°C for 1h solid (**4c**).

Annex IV

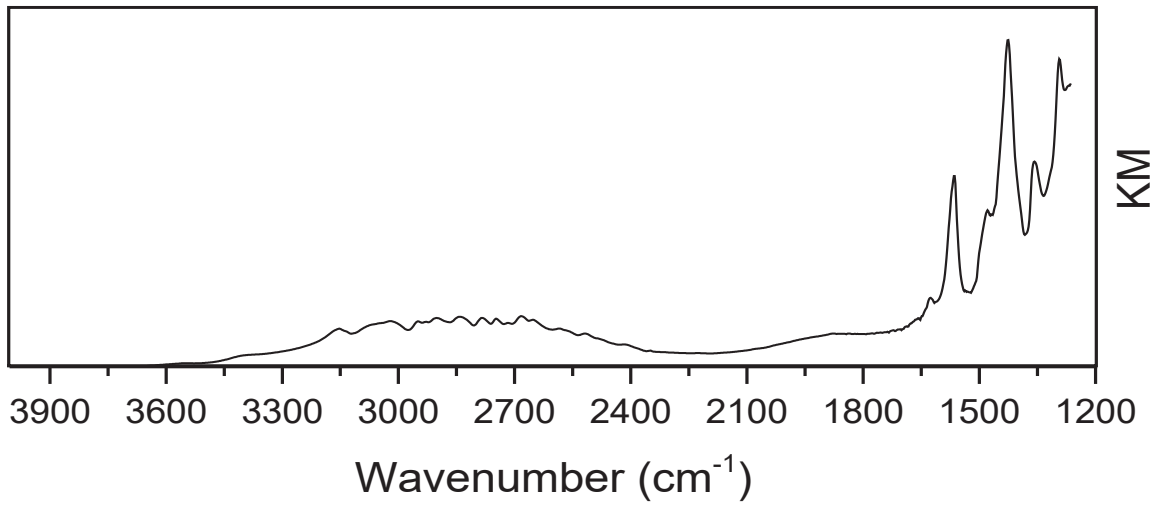

DRIFT spectra of 2-mIm@$TiO_{2(700)}$ at room temperature (20°C).

Annex V

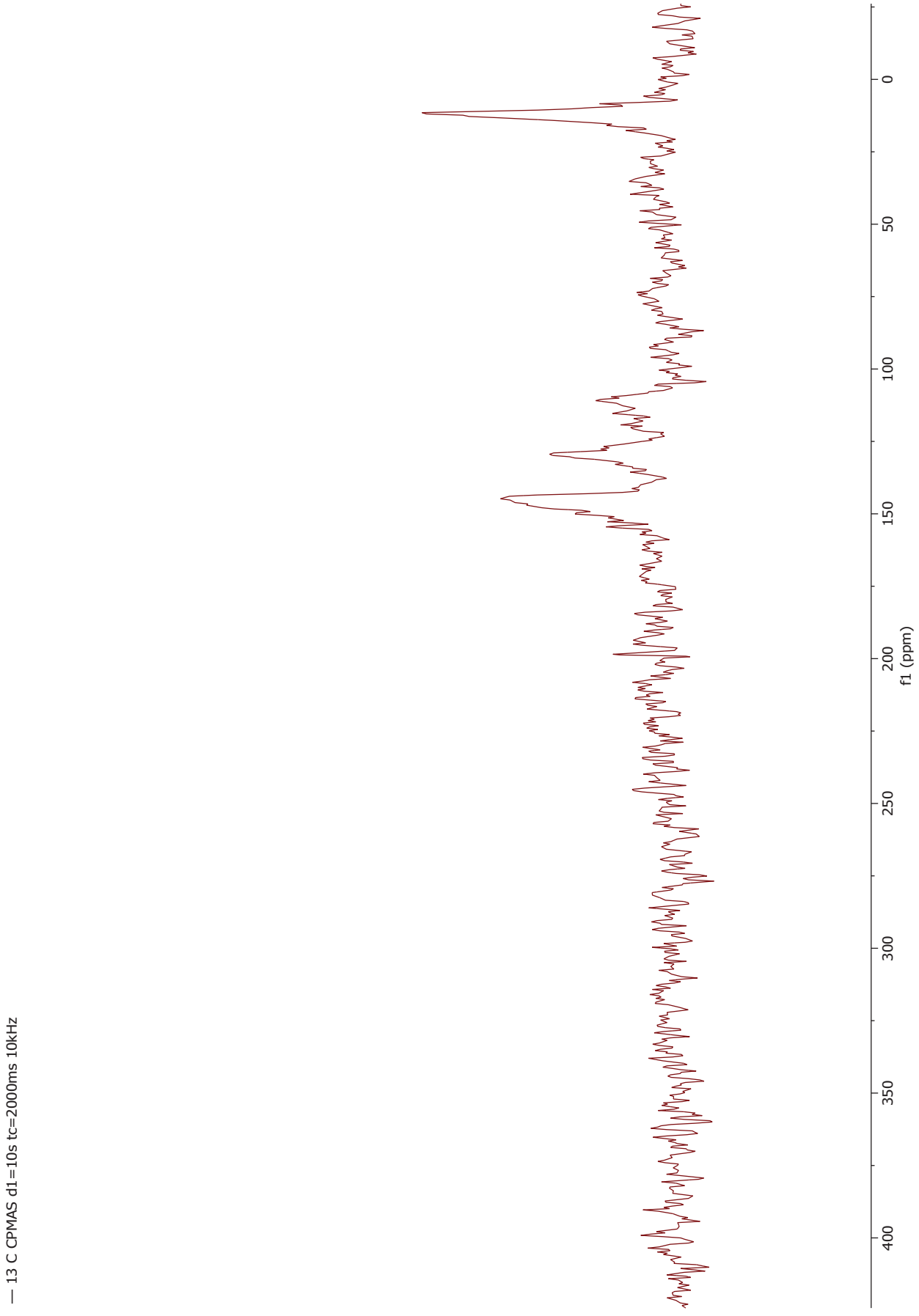
— 13 C CPMAS d1=10s tc=2000ms 10kHz
0
50
100
150
200
250
300
350
400
f1 (ppm)

Abstract

Surface organometallic chemistry (SOMC) is used to design well-defined catalysts. It has been employed here to lay the foundation of SOMC on photocatalytic support, a previously little if any explored area. TiO_2 anatase was used as the photocatalytic support due to its high stability, photoactivity and nontoxicity. The chemical nature and the surface density of the reactive moieties found on anatase support has been determined. A Ta complex, well-known in literature, was used to conduct the first principal studies regarding the interaction between the surface and the organometallic complex. The results provide solid insights into organometallic grafting and metal to metal charge transfer mechanisms for developing well-defined photocatalysts by SOMC.

Résumé

La chimie organométallique de surface (COMS) est une technique utilisée pour concevoir des catalyseurs structurellement bien définis. Elle a été employée ici pour établir les fondements de la COMS sur des supports photoactifs. L'oxyde de titane, TiO_2 à savoir l'anatase a été utilisé comme support photo-catalytique en raison de sa haute stabilité, photo-activité and non toxicité. La nature chimique et la densité des sites réactifs de surface ont été établies. Un complexe de Ta bien connu de la littérature a été utilisé pour mener les premières études d'interaction entre la surface et le complexe organométallique. Les résultats ont permis d'observer le greffage organométallique couplé à des mécanismes transfert de charge métal sur métal, en route vers des photo-catalyseurs bien définis.

Riassunto

La chimica organometallica di superficie (COMS) è una tecnica utillizzata per sintetizzare catalizzatori strutturalmente ben definiti. È stata utilizzata in questa tesi per stendere le fondamenta per l'utilizzo di tecniche COMS su un supporto fotocatalitico, un'area precedentemente poco se non mai esplorata. La TiO_2 anatase è stata utilizzata come supporto fotocatalitico per la sua elevata stabilità, fotoattività e non tossicità. È stata determinata la natura chimica e la densità della superficie dei frammenti reattivi riscontrati sul supporto di anatase. Un complesso di Ta, noto in letteratura, è stato utilizzato per condurre i primi, principali studi riguardanti l'interazione tra la superficie e il complesso organometallico. I risultati hanno fornito dei dettagli accattivanti sul grafting di specie organometalliche e sui meccanismi di trasferimeto di carica metallo-metallo per lo sviluppo di fotocatalizzatori strutturalmente ben definiti.